Aus der Klinik für Frauenheilkunde,
Geburtshilfe und Reproduktionsmedizin
Universitätsklinikum des Saarlandes, Homburg/Saar
Direktor: Prof. Dr. med. E.-F. Solomayer

Micro/Nano Modification of PEEK Surface for Possible Medical Use

Dissertation

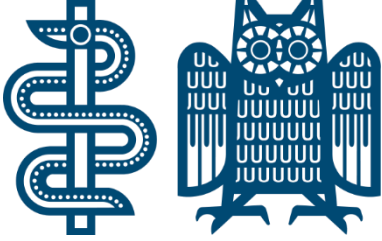**zur Erlangung des Grades eines Doktors der Naturwissenschaften**

der Medizinischen Fakultät

der UNIVERSITÄT DES SAARLANDES

2013

Vorgelegt von: Cagri Kaan AKKAN

geb. am: 31.01.1985 in Istanbul, Türkei

This thesis was performed in close collaboration with CVD/Biosurfaces Division at INM-Leibniz Institute for New Materials and biology laboratory of Pediatric Cardiology Department at Medical Faculty of Saarland University located at the same institute.

Kendiniz için değil millet için elbirliğiyle çalışınız. Çalışmaların en yükseği budur.

Work not for yourself, but collectively for the people. This is the noblest work ever…

M. Kemal ATATÜRK

Abstract

Cell adhesion and proliferation has high importance in the case of human implantation where the surface properties of the materials define the cell response. In this context, surface modifications of these implants were carried out by several groups where the nano and micro surface topographies are introduced to implant surfaces. However, surface chemistry may change depending on the chosen method during the modification process. Therefore, it may be helpful by keeping the surface chemistry identical in order to understand the cellular response to the implant materials in terms of the surface topographic features. In this context, surface modification of Polyetheretherketone (PEEK) was performed by laser and plasma treatment methods in terms of the micro and nano scale surface structuring in order to understand the endothelial cell response to the structured surfaces. Laser system was used to realize periodical structures while oxygen plasma system was used to create one dimensional nano structures over the surfaces. A microlens array was used to realize the periodical structures over planar PEEK and plasma treated PEEK substrates where it can create around four thousand identical structures over the substrate surface. However, due to the non-identical surface chemistries of PEEK surface types after treatments, thin alpha alumina layer was deposited over the substrates surface by pulsed laser deposition technique in order to perform identical surface chemistries. Generated surfaces were analyzed for their surface properties and their cellular behaviors to the endothelial cells were tested in-vitro. Additionally, generated PEEK surfaces were compared for their cellular responses with commercially available alumina plates, with one dimensional Al/Al_2O_3 core/shell nanowires which were deposited on glass substrates by chemical vapor deposition and with their periodically structured surface types by laser system. It was observed by the entire experiments, combination of micro and nano surface structures for alumina and alumina coated PEEK substrates have high influence on the endothelial cell proliferation in comparison to other generated surface structures. Besides, it was observed that the tendency of the cell proliferation rates for each comparable surface (for example: Al/Al_2O_3 core/shell nanowires to nano structured and alumina coated PEEK surface) are indicating high similarity. This result can bring up a new point of view for the medical applications where the implant materials with low melting temperature can be processes by the investigated experimental methods in comparison to the high melting temperature materials with the same surface topography and the chemistry.

Zusammenfassung

Adhäsion und Proliferation von Zellen haben eine große Bedeutung bei Implantaten, da hier die Oberflächeneigenschaften die Zellantwort definieren. In diesem Zusammenhang wurden die Oberflächen der Implantate in verschiedenen Gruppen mit Mikro- und Nanostrukturen versehen. Die Oberflächenchemie kann sich jedoch in Abhängigkeit der jeweiligen Strukturierungsmethode ändern. Um die Effekte der Oberflächentopografie auf die Zellantwort zu verstehen ist jedoch es notwendig die Oberflächenchemie aller Strukturen identisch zu halten. Die Oberflächenmodifikation von Polyetheretherketon (PEEK) wurde durch Plasma- und Laserbehandlung durchgeführt. So wurden Mikro- und Nanostrukturen hergestellt um das Verhalten von Endothelzellen auf strukturierten Oberflächen zu untersuchen. Die Herstellung periodischer Mikrostrukturen wurde mittels Laserablation durchgeführt, während die eindimensionalen Nanostrukturen in einem Sauerstoffplasma erzeugt wurden. Ein Mikrolinsenarray, welches etwa viertausend identische Strukturen auf der Substratoberfläche kreieren kann wurde verwendet um die periodischen Strukturen auf ebenen und auf plasmabehandelten PEEK-Substraten herzustellen. Wegen den nicht identischen chemischen Eigenschaften der Oberflächen nach den verschiedenen Behandlungen wurde mittels Pulsed Laser Deposition eine dünne Schicht alpha-Aluminiumoxid abgeschieden. Bei den so hergestellten Proben wurden die Oberflächeneigenschaften analysiert und ihre Wechselwirkung mit Endothelzellen in vitro getestet. Die PEEK Oberflächen wurden bezüglich ihrer Zellantworten mit anderen Proben verglichen. Die Vergleichsproben bestehen aus kommerziell erhältlichen Aluminiumoxidplatten und eindimensionalen Al/Al_2O_3 Kern/Hülle-Nanodrähten, die mittels Chemischer Gasphasenabscheidung auf Glas hergestellt wurden sowie durch Laserablation periodisch strukturierte Oberflächen dieser Materialien. Über die gesamten Experimente wurde beobachtet, dass die Kombination von Mikro- und Nanostrukturen auf Aluminiumoxid und mit Aluminiumoxid beschichteten PEEK Substraten, im Vergleich mit anderen hergestellten Strukturen einen großen Einfluss auf die Proliferation von Endothelzellen hat. Außerdem wurde beobachtet, dass die Tendenz der Zellproliferationsrate für jeweils vergleichbare Oberflächen (z.B. Al/Al_2O_3 Kern-Hülle Nanostrukturen und nanostrukturierte PEEK Substrate mit Al_2O_3 – Beschichtung) hohe Ähnlichkeiten aufweisen. Dieses Ergebnis kann eine neue Perspektive für medizinische Anwendungen eröffnen, bei der Implantatmaterialien mit niedrigen Schmelzpunkten mit den untersuchten Methoden prozessiert werden statt Materialien zu verwenden, welche die gleiche Oberflächentopographie und –Chemie haben aber sehr hohe Schmelzpunkte besitzen.

1   INTRODUCTION

Since years, researchers from different disciplines such as physics, engineering, chemistry, biology and medical sciences, are working together in order to develop new materials for medical implantations. In this context, they developed various implants using metals, ceramics and polymers where they can be used in different parts of the human body. Spinal, hip, knee, femoral implants, stents, heart valves, pace makers, artificial veins, artificial heart pumps and dental implants can be sort as examples (Ratner et al. 1996; Liang et al. 2005) While researcher are choosing and/or developing materials as medical implants, they mostly pay attention to their mechanical and chemical properties where they have to be inert in the human body and strong enough to resist to the applied forces. Therefore, of course depending on the usage area of the implant, chosen material have to be rigid or flexible. Titanium (Ti) and its alloys can be a good example for rigid and flexible implants where the implant must be rigid for femoral applications while it must be flexible for the stent applications. However, it does not matter where they are used, all implants have to be biocompatible which means that the material that will be implanted into the body will induces any inflammation and causes any tissue differentiation around material itself while providing optimum conditions for the cell growth and proliferation (Ratner et al. 1996; Liang et al. 2005). Thus, cell interaction with the material surface is the critical issue for implant. Therefore, modification of an implant surface in terms of surface chemistry and surface topography may be needed in order to control the cell-surface interaction.

Additionally, it is known that the micro and nano features including with the roughness values and the chemistry of the surface have high influence on the cell-surface interaction (Dalby et al. 2004; Guilak et al. 2009; Bettinger et al. 2009; Moe et al. 2012). Cells sense the micro and nano structures with a natural mechanism which is called "Contact Guidance". Contact guidance regulates the cell migration on the surface depending on the extra cellular matrix (ECM) proteins. ECM contains native nano structures inside itself, such as collagen molecules which are in the range of sizes around 300 nm long and 1.5 nm wide. These collagens may create longer fibrils which can be in micrometer scale (Bettinger et al. 2009; Biela et al. 2009). Therefore, behavior of the cell to the structures with different scale and geometry can be different. Today, improvements in the micro and nano surface structuring techniques enable the researchers to produce surface structures similar to the ECM molecules in terms of the size. Grooves in micro and nano range, fibers with diameters in nano scale, micro spots and many

other surface structures can be produced with high precision in order to use on implant surfaces to improve their biocompatibilities. On the other hand, chemical properties of the produced surfaces define the protein adsorption when material surface meets with the blood. Therefore, surface chemistry has to be defined while the topographic features are presenting on the surface (Guilak et al. 2009; Bettinger et al. 2009; Biela et al. 2009; Hayes et al. 2012; Aktas et al. 2012; Veith et al. 2012).

In this context, laser and plasma surface modification techniques were performed on polyetheretherketone (PEEK) substrates in order to understand the endothelial cell reaction to these substrate surfaces. For this purpose, micro and nano surface structures were performed over PEEK surfaces with plasma and laser surface modification techniques which includes also the Pulsed Laser Deposition technique (PLD) for the deposition of ultra-thin alumina layer on PEEK surfaces. Additionally, generated PEEK surfaces were compared for their cellular responses with commercially available native alumina plates, with 1D Al/Al_2O_3 core/shell nanowires (NWs) which were deposited on glass substrates by chemical vapor deposition (CVD) and with their periodically structured surface types by laser system. Entire experiments were carried out in order to find out the optimum modification parameters for alumina and PEEK to use for cell culturing experiments afterwards. Schematic illustration of the surface types that planned are given in Figure 1.1 with expected cell-surface interactions
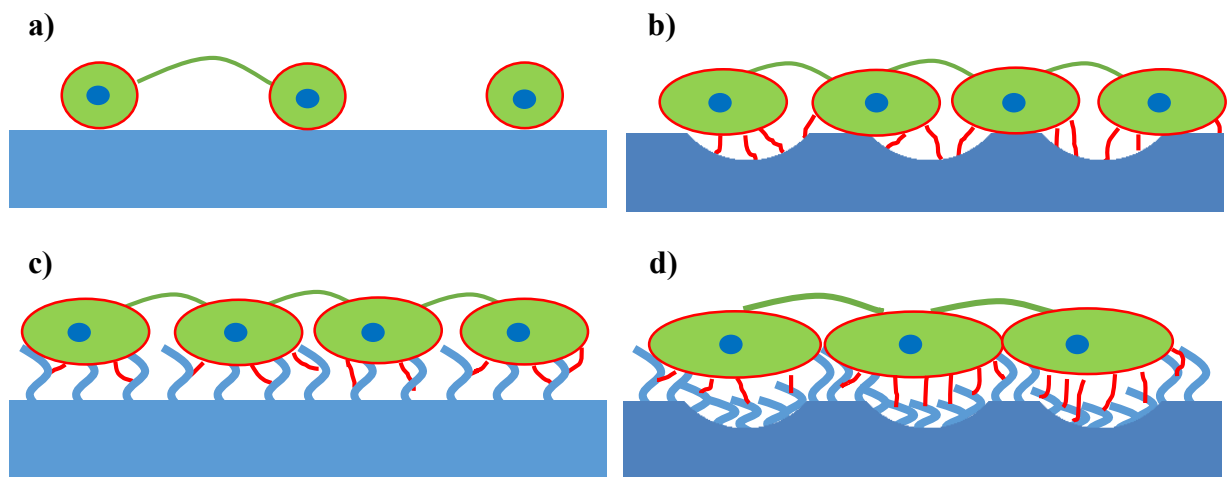

Figure 1.1: Schematic illustration of the planned surface types with the expected cell-surface interactions a) planar surface, b) micro surface structures, c) modified with sub-cellular surface structures and d) combination of micro and sub-cellular structures.

1.1   Laser Material Processing

Since lasers are discovered they became invaluable tools in human life. Today lasers are in use of different fields such as medical devices for eye surgeries in medical applications, as fast and precise cutters, drillers and welders for automotive industry, at the optical parts of weapons for military applications, in the entertainment industry as light shows, in communication and of course for different kinds of research fields in science from material processing to biological applications (Silfvast WT 1996). Usage areas of lasers can be seen in Figure 1.2 (Majumdar et al. 2003).

Communication
- Fiber Optic Com.
- Wireless Com.

Research & Development
- Holography
- Interferometry
- Microscopy
- Spectroscopy
- **Deposition**
- **Surface Mod. (Research)**

Military
- Weapon Guiding
- Atomic Fusion

Medical
- Plastic Surg.
- Cancer Therapy
- Dermatology
- Dental
- Eye Surgery
- Stent Cutting

Entertainment & Daily Life
- Printer/Scanner
- Light Shows
- Pointers
- CD/DVD

Industry
- Cutting
- Drilling
- Welding
- **Surface Mod.**
- Deposition
- 3D Printing

Usage Areas of Lasers

Figure 1.2: Table of usage areas of lasers (Majumdar et al. 2003).

Laser structuring is one of the effective and fast surface modification techniques which are popular in research and industry. Variable operation parameters; such as pulse duration/length and wavelength, provide new approaches especially for scientists in order to understand laser material interaction. Laser can be used either to alter the chemistry in addition to the surface topography modification. It is known that such modifications can cause additional changings on the material surface. Wettability, which has also critical importance for the cell adhesion and proliferation, can be count in these circumstances (Ratner et al 1996; Liang et al.

2005; Aktas OC 2009; Riveiroa et al. 2012). Laser surface treatment can be carried out also by modifying the laser output beam. A useful technique for this can be the laser interference lithography where it is possible to create grooves or spots over the material surface. Axonal alignment of a neuron cell was shown on 1D Al/Al_2O_3 core/shell nanowires treated by direct laser interference method (Lee et al. 2013).

1.1.1 Physical Background of Lasers

Laser is a device which produces intensive, directional and coherent light from far infrared to deep ultraviolet region of the electromagnetic spectrum. It is originally a shortened term of "Light Amplification by Stimulated Emission of Radiation" (Silfvast WT 1996). Basics of lasers were started in 1917 with an idea by Albert Einstein which was a theory to get stimulated emission from an atom. Unfortunately, it took around forty years for its discovery. The first working laser was invented by Theodore Maiman in 1960 from a ruby crystal. It was a simple cavity solid state laser system which has a high reflecting mirror at the back side of the ruby crystal and equipped with a flash lamp in order to pump the crystal itself. One year after this invention the first gas laser which is using He and Ne gases in its active medium was produced by A. Javan, W. Bennett and D. Harriott in 1961. Within the following years the first semi-conductor laser, CO_2 laser, Ar^+ and Excimer lasers were discovered. These lasers are still the most wanted lasers in the market (Träger F 2007).

The usage areas of lasers are dependent on the application field. Related to this reason, it is possible to produce different types of laser with different working principles and of course with different output wavelengths. The wavelength of a laser is depending on the lasers active medium (gain medium) which is standing in the center of the laser cavity. Simply lasers are composed of 3 main components. They are:

1) An active medium which gives the characteristic properties of the output beam.
2) A pump source which starts the population inversion inside the active medium by stimulated emissions.
3) Two mirror system as an optical cavity which helps to increase the number of the photons exponentially by several reflections in a short distance.

Table 1.1: Some types of lasers and their wavelength (Akkan ÇK 2009)

Active Medium	Laser Type	Wavelength
Nd:YAG	Solid State	1064 nm
InGaAs	Semi-conductor	980 nm
Ti: Sapphire	Solid State	700-1000 nm
InGaAlP	Semi-conductor	635-660 nm
HeNe	Gas	633 nm
Ruby	Solid State	628 nm
Cu	Metal Vapor	578 nm
Krypton	Gas-Ion	530.9 nm
Cu	Metal Vapor	511 nm
Argon	Gas-Ion	488 nm
XeF	Gas (Excimer)	351 nm (UV-A)
KrF	Gas (Excimer)	248 nm (UV-C)
KrCl	Gas (Excimer)	222 nm (UV-C)
ArF	Gas (Excimer)	193 nm (UV-C)

Some laser types with their active mediums and output wavelengths can be seen in Table 1.1. On the other hand we can classify lasers as continuous wave (CW) or pulsed lasers due to their operation regime. CW lasers give a constant output power with a little or even no fluctuation within the time while the output power of a pulsed laser is related on the optical pulse itself. Pulse length can be chance from ms to fs. For the pulsed lasers, we can talk about two different energies:

1) Average Power: The power of the laser output which can be calculated by multiplying the output energy with laser operation frequency.
2) Peak Power: The power of the laser output which can be calculated by dividing the output energy of the laser to its optical pulse length (Power of single laser pulse).

Therefore pulsed lasers are tended to produce high peak powers at the work place in comparison to the CW laser. Thus, such lasers are preferable for drilling and fine structuring material processes (Träger F. 2007; Akkan ÇK 2009).

1.1.2   Laser Surface Structuring

In industry lasers are in use since years for drilling, cutting and welding processes due to their non-contact, fast, and precise machining features (Herzog et al. 2008; Kannatey-Asibu E 2009; Romoli et al. 2012). Related to the same potential, lasers can be used for surface structuring of materials in many different industrial fields as surface heat treatment method in order to change the chemical and physical characteristics of materials, as cladding of powder materials over different surfaces or direct laser modification for hardening (Yue et al. 2001; Riveiroa et al. 2012). In addition, surface micro machining/structuring of materials is another important field for the chemical and physical modification of the surfaces. Such changes after surface modification are highly in use for some application fields to improve the adhesion properties of materials and giving hydrophobic/hydrophilic behavior to the surfaces. On the other hand, laser surface modification processes are highly in use in biology and medicine as improved cell-surface interaction of implant materials (Laurens et al. 2000; Riveiroa et al. 2012). Due to these circumstances, choosing the right laser parameters takes high importance for the material processing. These parameters can be listed as:

- Absorption and wavelength
- Polarization
- Operation mode
- Pulse length and pulse power
- Beam mode and beam quality

1.1.2.1   Absorption and Wavelength

Wavelength selection is one of the most important parameters for all over the material processing fields. Absorption ratio of the material at the selected wavelength plays a critical role in all kinds of laser processes. Absorption is related to reflectivity of the material at the certain wavelength. Reflectivity "*R*" of a material can be calculated as shown in equation 1.

$$R = \frac{(1-n)^2 + k^2}{(1+n)^2 + k^2}$$
(1)

Here n is the real part and k is the imaginary part of the refraction index "η ($\eta=n-ik$)". Real and imaginary parts of refractive index for each material are wavelength dependent. Therefore, they vary with the wavelength. If the transmission of the light is negligible for the material, then the absorption "A" of the surface is simply (Steen et al. 2010):

$$A = 1 - R \tag{2}$$

These parameters may show some differences depending on the material surface. For example, roughness value and the temperature of the surface and also the polarization of the incoming light affect the absorption of the material (Steen et al. 2010). Laser wavelength affect is investigated by Tunna et al. for the drilling of cupper with 1064 nm, 532 nm and 355 nm Nd:YAG laser with different laser pulse energies for depth and crater diameter of the drilled hole (Tunna et al 2001). Another wavelength-structure results were reported by Riveiro et al. for the PEEK which is treated with Nd:YAG laser operated at fundamental, second and third harmonic wavelengths and they showed that the third harmonic treatment resulted with smooth structures unlike the fundamental and second harmonic studies (Riveiroa et al. 2012). SEM images of PEEK treated by ns pulsed Nd:YAG laser at 532 nm and 355 nm wavelengths had been given in Figure 1.3 which were performed previously in our laboratories.
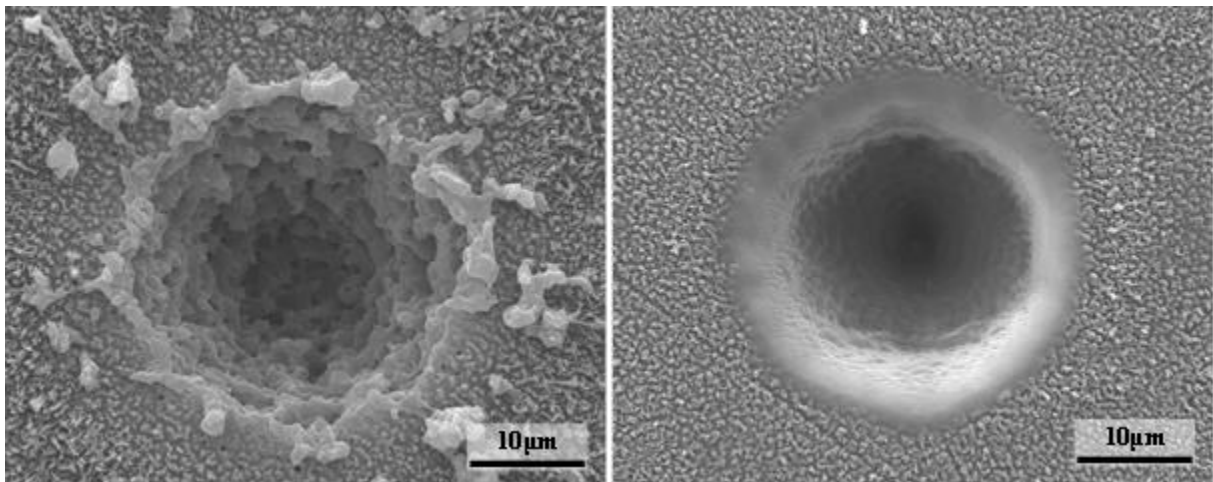

Figure 1.3: SEM images of PEEK treated by ns pulsed Nd:YAG laser at different wavelengths 532 nm (left) and 355 nm (right)

1.1.2.2   Polarization

Polarization of light is defined mainly in three different forms. If the wave vectors are propagating in one direction this is called "*linearly polarized*", if they are propagating in two

directions while perpendicular to each other with equal intensities this is "*circularly polarized*" and if the intensity of one of the perpendicular vector is less than the other, it is called "*elliptically polarized*" (Figure 1.4-a). Polarization has important influence on the reflectivity of the light from the surface and the reflectivity equations for two different linear polarization states "*p*" (parallel to the normal of the material surface) and "*s*" (perpendicular to the normal of the material surface) can be derived from reflection coefficients "*r*" (Hecht E 2002; Träger F 2007; Steen et al. 2010):

$$r_p = \frac{n_t \cos \theta_i - n_i \cos \theta_t}{n_i \cos \theta_t + n_t \cos \theta_i}$$

$$r_s = \frac{n_i \cos \theta_i - n_t \cos \theta_t}{n \cos \theta_i + n_t \cos \theta_t} \tag{3}$$

Here θ_i is the angle of the incoming light with surface normal and θ_t is the angle of refracted light inside the material. n_i and n_t are the refractive indexes of the air and the material respectively. n_i can be noted as 1 and θ_t can be noted as 0 because of the non-transmitting medium.
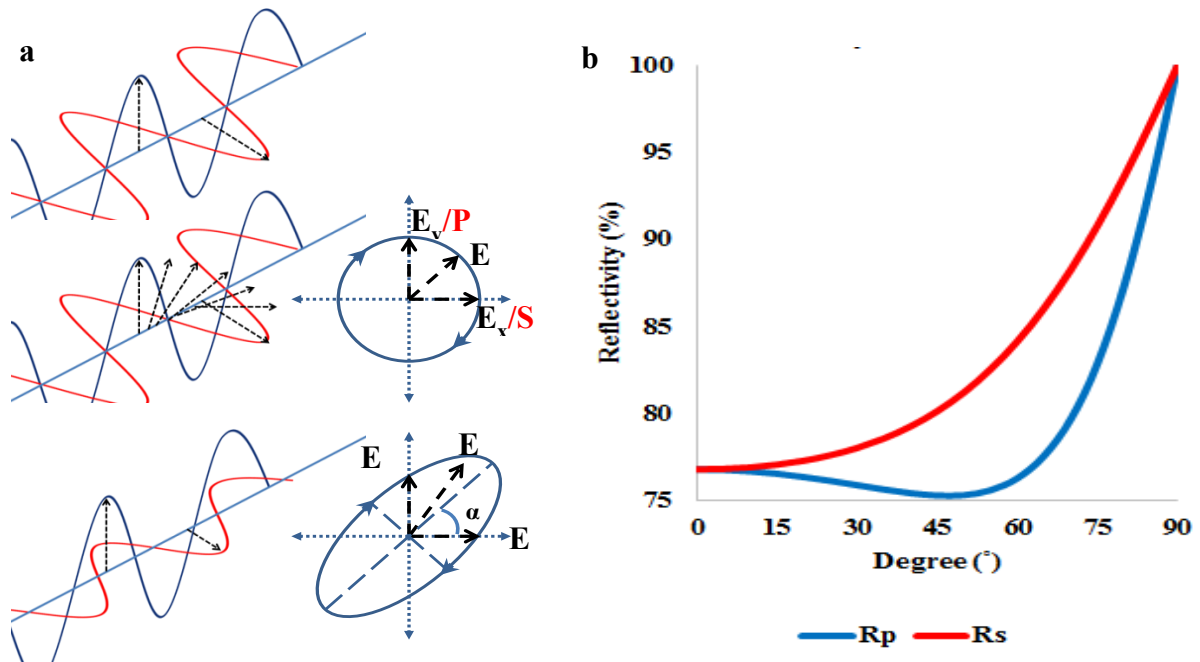
Figure 1.4: a) Different polarization states of light (Up to down: linear, circular and elliptical), b) Reflectivity of silver at "p" and "s" linear polarization states (Hecht E 2002; Refractive Index Database 2012)

When the real and imaginary parts of the refraction indexes used for the r_p and r_s (as mentioned above), reflectivity of the material for certain wavelength for the *p* and *s* polarization states can be derived.

$$R_p = |r_p|^2 = \frac{(n_t - 1/\cos\theta_i)^2 + k_t^2}{(n_t + 1/\cos\theta_i)^2 + k_t^2}$$

$$R_s = |r_s|^2 = \frac{(n_t - \cos\theta_i)^2 + k_t^2}{(n_t + \cos\theta_i)^2 + k_t^2} \tag{4}$$

This effect can be seen for silver at Figure 1.4-b (Refractive Index Database 2012). If the angle of the incoming light is perpendicular to the material surface, reflectivity of the substrate at the selected wavelength can be calculated with equation 1 independently from the linear polarization state.

1.1.2.3   Operation Mode

Laser operation mode is an important point for material processing especially for laser assisted cutting processes in the industry. CW lasers may cause burning effect (Heat affected zone) around the cut due to their CW light emission regime. Such problems can be reduced in case of pulsed lasers usage. Furthermore, the penetration depth of the laser beam for high reflecting and high conducting materials can be increased by pulsed lasers due to their high peak powers. Three kinds of pulse modes are mostly in use for these applications. These are:

1) Modulated Pulsed Lasers (Gated Pulsing): which are working with a principle of switching the laser on and off by electronic controllers. Thus the laser output power is almost the same like CW operation mode but operates in pulse mode. (Figure 1.5-b)

2) Super Pulsing: It is possible to get 2 or 3 times more output power by this technique in comparison to CW lasers. This effect can be reached by electronic configuration for short time of periods. (Figure 1.5-c)

3) Hyper Pulsing: Q-Switch Pulsed Lasers are a good example for such kind of pulsing method. In this method, laser beam switched for shorter times with in the laser cavity like nanosecond or picosecond. Due to this property, such laser can produce powers within the ranges of gigawatts per pulse. (Figure 1.5-d) (Abdel Ghany et al. 2005; Kannatey-Asibu E 2009; Steen et al. 2010; Gabzdyl et al. 2013)
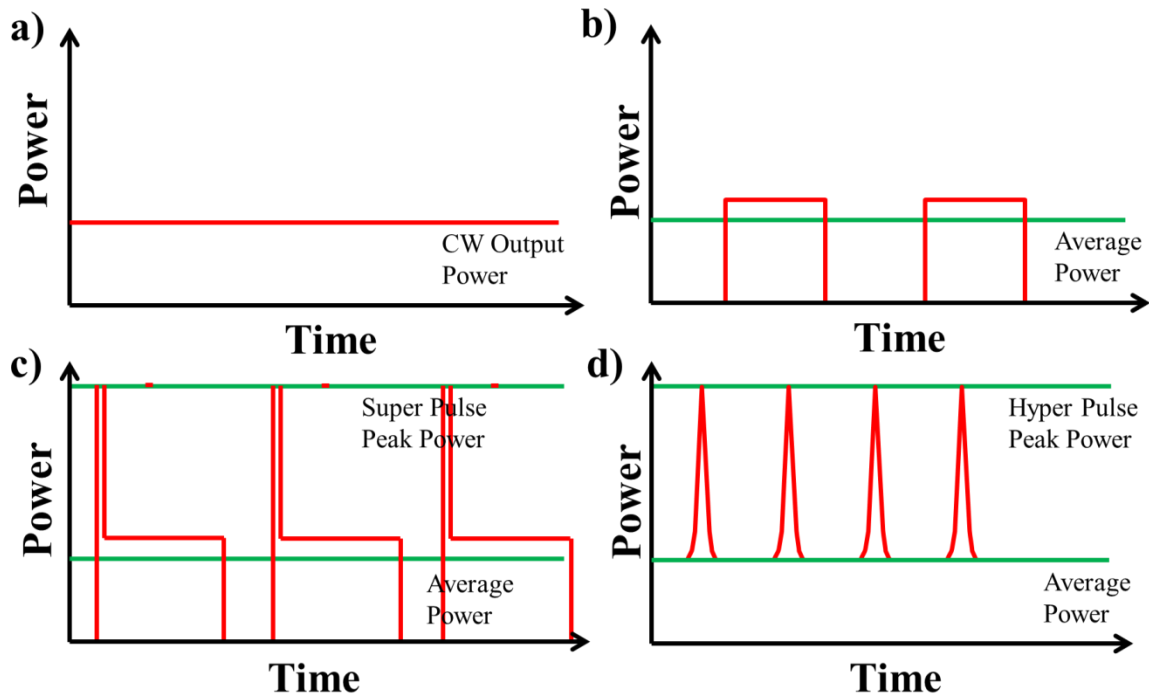
Figure 1.5: Operation mode differences a) CW output, b) Gated pulsing, c) Super pulsing, d) Hyper pulsing (Kannatey-Asibu E 2009)

1.1.2.4 Pulse Length and Pulse Power

Manufacturing fine structures from machining process is necessary for many applications. Therefore pulsed lasers are preferable devices due to their high peak powers in a short time which is related to its pulse length. Peak power was explained in chapter 1.1.1. As explain by Knowles et al. ultra-short pulses have certain advantages on processing of materials, especially for dielectrics due to their thermal penetration depths and material removal rates (Knowles et al. 2007).

When the photon is absorbed by the electron, the lattice starts to heat up by vibrations and this takes around few picoseconds which is called "lattice heating time". Absorption maybe happens via capturing the photon by phonon structure or affecting the electron with the electromagnetic wave of the photon itself (Knowles et al. 2007; Steen et al. 2010). Therefore, for the lasers operating at CW or long pulse (in ms region) regime, material will melt primarily and then evaporates after the exposure. Such lasers can be useful also because of this property due to breaking the weaker bonds of the material with lattice vibration. This effect may leads to the evaporation of the material at lower temperatures than the original material (Steen et al. 2010).

For short pulse duration lasers (in μs and ns region) the thermal effect is less in comparison to CW or long pulse lasers. These lasers are useful for the fine drillings and surface structuring of the metals with less molten effect. However, depending on the pulse length of the laser, the pulse energy must be controlled in order to prevent plasma formation at the focal point while working with such lasers. Plasma formation happens at the focal area if the pulse energy is too high to evaporate the material. Formed plasma enhances the melting process of the material and also helps for the removing of the molten part with the high pressure directed into the forming crater. This pressure can be around 1kbar under vacuum conditions (Schou J 2006; Knowles et al. 2007). Plasma formation at the treatment area can cause blocking of the incoming laser intensity completely if the laser frequency is smaller than the plasma oscillation frequency or it fully transmit if the laser frequency is greater than plasma oscillation frequency. This effect is called "plasma shielding". In most of the cases, laser beam can pass through from the plasma because the selected laser frequency for the material processing is usually larger than the oscillation frequency of the generated plasma (Kannatey-Asibu E 2009; Mutlu et al. 2009).

For ultra-short laser pulses (ps and shorter) pulse duration is shorter than the lattice heating time of the material. This time is usually between 0.5 to 50 ps. Due to this reason, thermal damage will be less in comparison to the CW, long and short pulse duration lasers. Therefore, processing of the material will be more precise. Due to this reason, picosecond lasers give better results for the machining of metals while femtosecond lasers are preferable for the machining of the dielectrics (Knowles et al. 2007; Steen et al. 2010).

However, today, ns second lasers are the lasers where they are mostly in use for the industrial works due to their well-established know-how in material processing (Knowles et al. 2007).

1.1.2.5   Beam Mode and Beam Quality

Usually two kinds of beam modes are under discussion in laser processing. They are TEM_{00} Gaussian Mode and TEM_{mn} Multi Mode laser outputs where the TEM means "Transverse Electromagnetic Modes". "m" and "n" numbers indicate the number of the dark patterns at the intensity distribution of the laser beam profile horizontally and vertically (Kannatey-Asibu E 2009; RP Photonics Consulting GmbH 2012). TEM_{mn} modes and

illustrations of Gaussian mode and multimode beam profiles can be seen in Figure 1.6. If laser beam has a Gaussian intensity distribution it can be focused to a small spot size and at the focal spot high intensities can be reached over the material. This is an important property for laser cutting process. However, multimode laser beams are preferable for laser welding due to their more homogeneous intensity distribution and high energies. Most of the Nd:YAG lasers are operate in multimode (Kannatey-Asibu E 2009). Additionally, M^2 factor is in use to indicate the laser beam quality compare to Gaussian beam. For a perfect Gaussian beam, theoretical M^2 factor is equal to 1. Focusing ability of the laser beam into a small spot size decreases when M^2 factor increases. High power Nd:YAG lasers have mostly an M^2 factor which stays between 50 and 100.
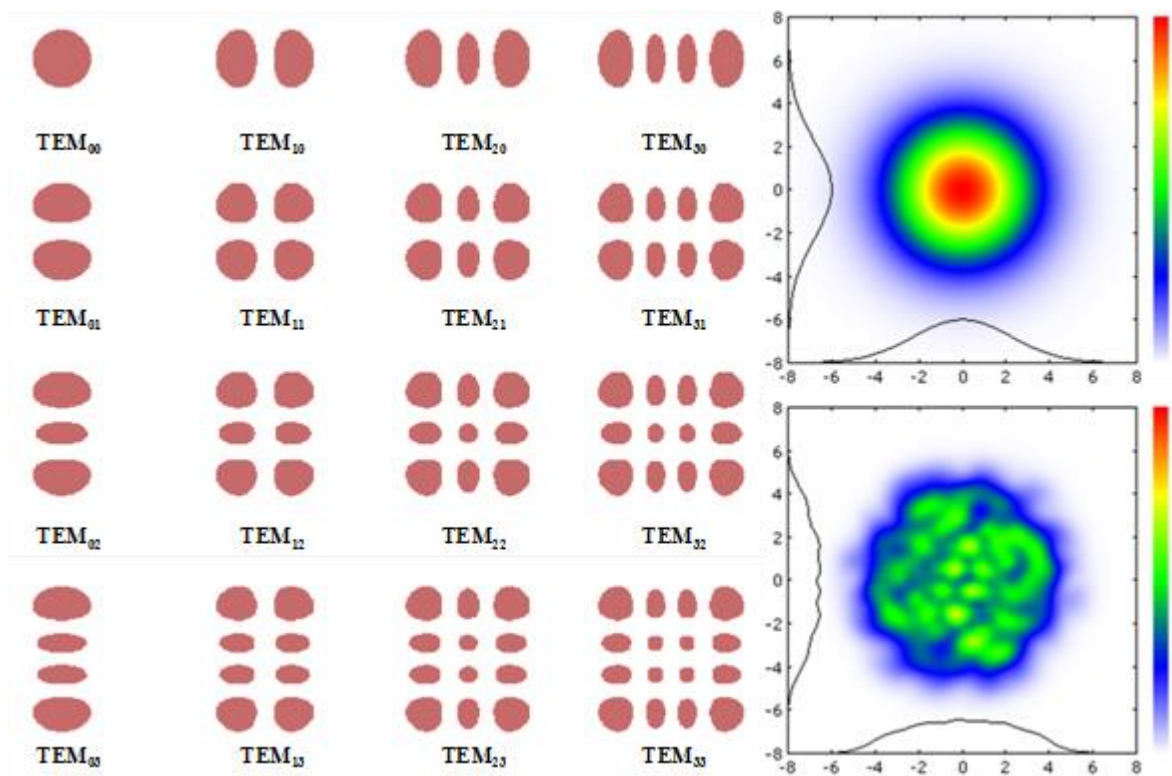

Figure 1.6: Transverse Electromagnetic Modes (TEM$_{mn}$) modes. On the right Gaussian mode (top) and Multimode (down) laser beam profiles. (RP Photonics Consulting GmbH 2012)

1.1.3 Material Ablation by Laser

As it is explained above, wavelength, polarization, operation mode and beam quality of the laser source have high importance in laser material processing. For the material removal, pulsed lasers are preferable devices due to their pulsed output with a certain frequency. However, in the case of long laser pulses (ms) laser light causes mostly melting and in the case of short pulses (ns, ps) material removal happens via ablation (Romoli et al. 2012). On the other hand, laser must work in a certain energy region which is enough to ablate the material from focal area on the surface which is called "Threshold Fluence" and is defined by the material properties (Bäuerle D 1996).

Material ablation occurs by pulse to pulse ablation which ablates same amount of material for each pulse. Ablation mechanism happens by photothermal or photochemical processes. Photothermal ablation occurs when the laser pulse duration is longer than the thermal relaxation time of the material lattice. Such a result mostly occurs when the IR or VIS lasers are used. In many cases, similar results can be seen while UV lasers are in use. Ablation depth *"d"* within a photothermal process can be explained simply with Arrhenius Equation:

$$d_{thermal} = Ae^{-E/RT} \tag{5}$$

where A, *R, T* and *E* are the effective frequency factor (μm/pulse), ideal gas constant, temperature at the laser focal area and activation energy respectively. As it is reported by Tsunekawa et al, temperature rise at the focal area is roughly linear. Thus, equation 5 can be expressed with the terms of laser fluence as equation 6.

$$d_{thermal} = Ae^{-B/\phi} \tag{6}$$

where *B* and *Φ* are the constant and laser fluence respectively (Babu et al. 1992; Tsunekawa et al. 1994; Bäuerle D 1996).

Photochemical ablation occurs at organic polymers and inorganic insulators without thermal effect where the UV lasers directly breaks the bonds and the ablation depth is explained by Beer's law:

$$d_{photo} = \alpha^{-1}\ln(\frac{\phi}{\phi_{th}}) \tag{7}$$

where *Φ*$_{th}$ is the threshold fluence of laser in order to ablate material and *α* is the absorption coefficient. However, some UV lasers do not have enough photon energy in order to break the

bonds with single photon. In such cases, thermal affect may occur as mentioned before. On the other hand, multi photon ablation can be seen for photochemical process which also does not cause any thermal effect (Hancock G 1988; Babu et al. 1992; Bäuerle D 1996; Yu F 2006).

Although these regimes can be seen alone during the ablation processes, in most of the cases, combination of the two mechanisms gives the result depth and this can be estimated with their sum:

$$d_{total} = \alpha^{-1} \ln\left(\frac{\phi}{\phi_{th}}\right) + Ae^{-B/\phi} \tag{8}$$

1.2 Plasma Material Processing

Plasma, which is known as the fourth state of the matter, can be defined simply as an electrically neutral cloud which composes of freely moving particles which are radicals, electrons and positive ions mainly (Lieberman et al. 2005; Bellan PM 2006). There are three main parameters to characterize plasma:

1) Particle Density (#/cm^{-3})
2) Particle Temperatures (in eV unit (1eV=11,605K))
3) Steady state magnetic field (Tesla)

There are three kinds of plasma available which are Non-Fusion, Fusion and Space Plasmas.

- Non-Fusion Plasmas are the kinds that can be seen in our daily life such as: fluorescent lamps, lightning between clouds and arc welding devices that highly use in industry. Furthermore, processing plasmas are also in this classification which is used in this thesis for material processing. Such plasmas have low electron temperatures and even colder ion temperatures at room temperature. They are weakly ionized and cannot produce significant magnetic fields. Particle densities for such kind of plasmas are between 10^{14} and 10^{22} in a cubic meter.

- Fusion Plasmas have high temperatures compared to the Non-Fusion Plasmas. They have a range in tens of eV to 10.000s of eV and have to be controlled carefully. "Tokamak" which uses to confine plasma with high magnetic fields (1-10 T) is an example for fusion plasmas and such devices have plasma particle densities between 10^{19} and 10^{21} in a cubic meter.

- Space Plasmas are usually fully ionized plasmas with particle densities in the range of 10^6 to 10^{20} in a cubic meter. Such plasmas have plasma temperature between 1 and 100 eV (Bellan PM 2006).

As mentioned in Non-Fusion plasma, two kinds of plasma processing methods can be used in material processing field. One of them is the "High Pressure Arc Discharge" plasmas which are in use of welding processes. Furthermore this plasma type can be used for increasing the surface reaction rates, sintering or evaporating and for cutting of the materials by applying heat to the work place. Application pressures of these plasmas are close to atmospheric pressure and particles in these plasmas are almost in thermal equilibrium with $T_i \leq T_e$. Here T_i and T_e are the temperatures of ions and electrons respectively (Lieberman et al. 2005).

The other mostly used method for material processing with plasma, which is also the investigated part of the Plasma Material Processing in this thesis, is the "Low Pressure Discharge" plasmas which are applicable under vacuum conditions with DC or mostly RF power supplies. RF driven plasma devices have advantages over DC driven plasma devices which makes possible to sputter or treat insulating substrates and materials. The vacuum levels for these plasmas are usually between 0.133 and 133 Pa and the particle densities are between 10^{14} and 10^{19} in cubic meter. In these kinds of plasma material processing, gas sources are used to react with the material surface via ionizing the gas between two electrodes by means of positive and negative electrodes where they create an electric field between. By this method, it is possible to change the chemical and physical properties of the material surface without changing its bulk properties. Some processes with this technique are given in Figure 1.7 (Chapman B 1980; Lieberman et al. 2005).

Low Pressure Discharge Plasma Processing

→ **Plasma Enhanced Chemical Vapor Deposition**

→ **Sputtering Deposition**

→ **Plasma Immersion Ion Implantation**

→ **Cleaning**

→ **Activation**

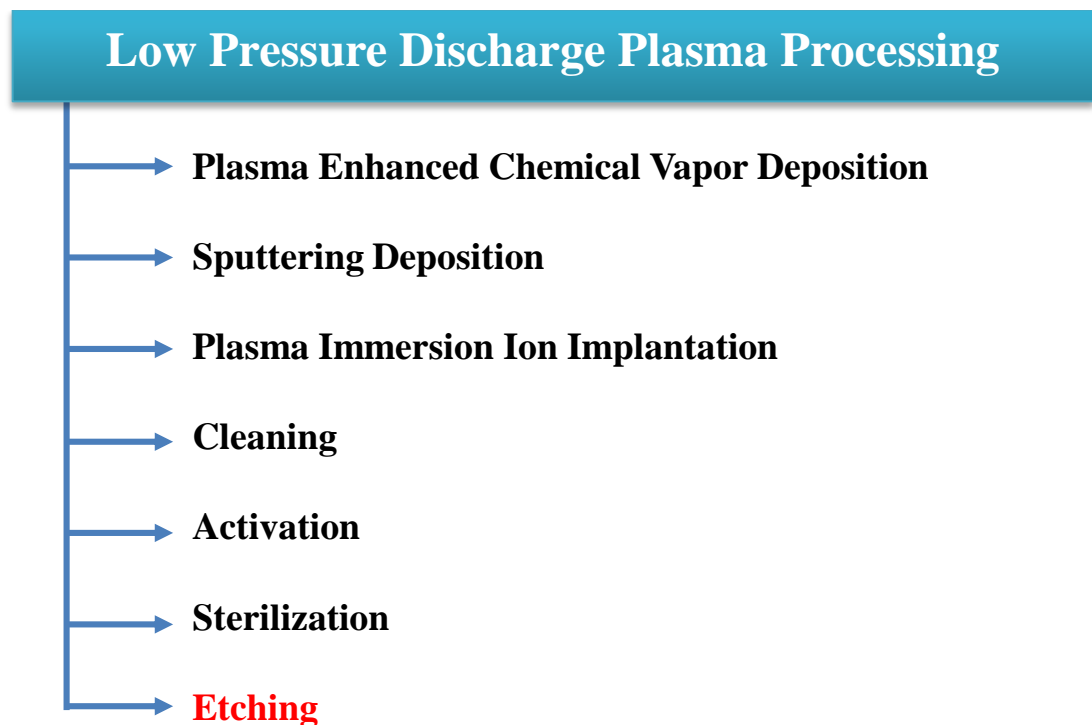→ **Sterilization**

→ **Etching**

Figure 1.7: Process options with Low Pressure Discharge Plasma Processing that can be used under vacuum condition with ionized gas (Lieberman et al. 2005; Diener electronic GmbH + Co. KG 2012).

1.2.1 Processing Types with Low Pressure Discharge Plasma

1.2.1.1 Plasma Enhanced Chemical Vapor Deposition (PECVD)

In comparison to traditional CVD process, PECVD is a way to deposit thin films over surfaces at lower temperatures by decomposing the introduced gas phase precursor with or without a gas supply. The vacuum level for PECVD is generally between 13 and 1330 Pa. Film properties that deposited by this technique, such as morphology and chemical composition, are related to the substrate temperature. On the other hand, homogeneity of the deposited films is one of the most critical point for PECVD. Therefor radio frequency (RF) power source equipped chambers are preferable. Glass like coating with hexamethydisiloxane (HMDSO) is one of the most common thin film applications by PECVD. Same precursor can be used to provide hydrophobic layers, too. (Hegemanna et al. 1999; Cao G 2004; Lieberman et al. 2005; Choudhury et al. 2011; Diener electronic GmbH + Co. KG 2012)

1.2.1.2 Sputtering Deposition

In sputtering deposition, ions, directed to the target material under the applied electric field, eject the atoms from the target via bombarding the target surface. Ejected atoms from the target get deposited on to the substrate surface. Argon gas is mostly in use as processing gas for this process. With this technique, it is possible to deposit metals, alloys and insulators. However it is not easy to deposit stoichiometric layers from multicomponent targets in most of the cases. If the adhesion coefficients of the components to the substrate are the same, then it can be possible to get stoichiometric layers. Furthermore, via adding some extra processing gases into the chamber different than Argon (such as: O_2 or N_2), layers which have different chemistries than the target can be sputtered by this method. This process is called "reactive sputtering". SiO_2 layer production from Si target under O_2 environment is an example of this technique. With this method of deposition it is possible to get homogenous coatings with good adhesion properties and low roughness values. Schematic illustration of RF sputtering can be seen in Figure 1.8. With this technique, polymeric implant materials can be coated in order to improve their biocompatibility. Hydroxyapatite deposition to the artificial bone implants can be an example for this deposition method. RF power sources are the key of sputtering insulating

materials by this technique. In the range of 5 MHz to 30 MHz RF sources are suitable for sputtering however 13.56 MHz sources are the most preferable ones and this frequency sources are reserved for all plasma material processing methods by Federal Communication Commission (FCC). (Cao G 2004; Lieberman et al. 2005; Bazaka et al. 2011).
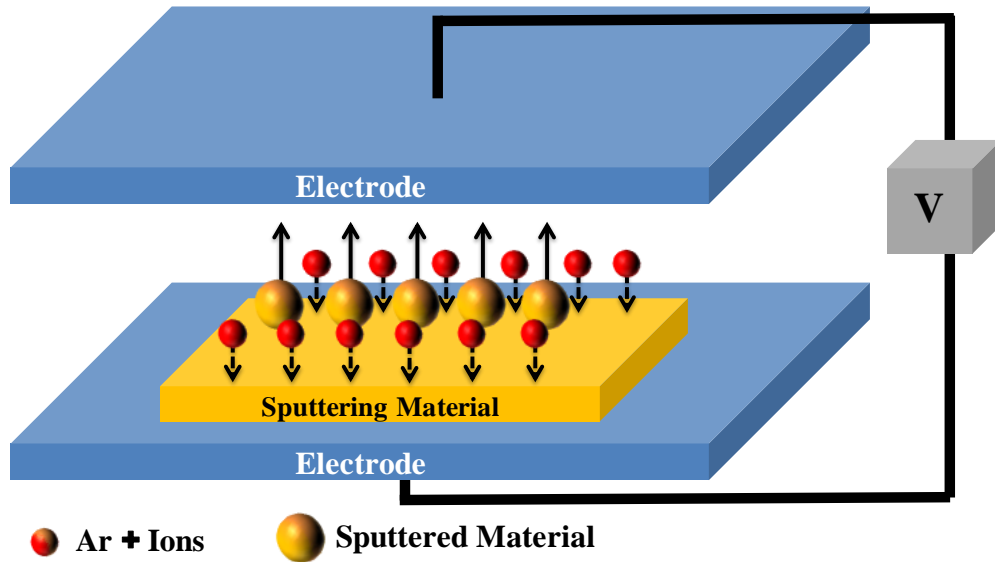

Figure 1.8: Schematic of the RF sputtering. Positive ions (red) bombard the target surface under the applied electric field and sputtered target atoms are deposited on the substrate.

1.2.1.3 Plasma Immersion Ion Implantation

Plasma immersion ion implantation is a technique which can alter the chemistry and structure of the material surface by injecting energetic ions to the surface. This method is mostly used in semiconductor technology. Furthermore, thin films of alloys can be produced by using this technique (Lieberman et al. 2005).

1.2.1.4 Cleaning

This is a sample preparation step where removing of organic contaminations from substrates surfaces by using plasma method before the main processing. Gas sources for this process are mostly oxygen, argon and air (Diener electronic GmbH + Co. KG 2012; Plasma Electronic GmbH 2012)

1.2.1.5   Surface Activation

This is a process which makes the substrates surfaces hydrophilic. Surface becomes hydrophilic via bombarding the substrate surface with oxygen ions and radicals. The reaction happens only at molecular level, thus, the bulk material is not affected from this process. This process is mostly applicable for polymeric materials and helpful for painting applications. Additionally, this process is useable for permanent sticking of two materials to each other. PDMS and glass; which are commonly in use for microfluidic fabrication can be stick to each other by this method. On the other hand, this process also finds places in medical fields because of the increased surface wettability where the cell adhesion influences by hydrophilic surfaces (Wu et al. 2006; Lee et al. 2010; Diener electronic GmbH + Co. KG 2012; Plasma Electronic GmbH 2012; Ratner et al. 1996; Liang et al. 2005).

1.2.1.6   Sterilization

By using air, oxygen or argon plasmas or their combinations, it is possible to isolate biomolecules, proteins, peptides and also bacterial spores from materials surfaces. This process is mostly in use with medical equipment producers, researchers and packing industries (Rossi et al. 2009; Diener electronic GmbH + Co. KG 2012).

1.2.1.7   Etching

Plasma etching is a method to remove materials from the surface of a bulk material by physical or chemical reactions. This process can be realized only for the selected material on the surface or by removing the material which part is unmasked during the process. Second method is highly in use for integrated circuit fabrication. On the other hand etching of polymeric materials is also another promising method for creating hydrophobic and hydrophilic surfaces (Lieberman et al. 2005; Tsougeni et al 2009). Four different etching types are in use with Plasma Etching Processes.

1.2.1.7.1   Sputtering Etching

Sputtering etching is the way of removing the surface atoms by energetic ion bombardment. This is a non-selective method to remove materials from the surface. This process is relatively slow due to removing the top layer of the surface atom by atom with single ions and dependent on the angle of incoming ions to the surface. Mostly ions with energies higher than 20-30 eV can be used for this method however the etching rate is not dependent on the ion energy, mostly dependent on the surface binding energies. Sputtering yields of some materials with Ar^+ are given in Table 1.2. If there is a secondary material as a substrate inside the chamber, the distance between the etched material and this substrate must be long enough in order not to make a deposition over the substrate surface (Lieberman et al. 2005; Fridman A 2008).

Table 1.2: Sputtering yield of several materials with Ar^+ at 600 eV energy (Fridman A 2008)

Material		Al	Si	Fe	Co	Ni	Cu	Ge
		0,83	0,54	0,97	0,99	1,34	2,00	0,82
		W	Au	Al_2O_3	SiO_2	GaAs	SiC	SnO_2
	S. Yield	0,32	1,18	0,18	1,34	0,9	1,8	0,96

2.2.1.7.2   Chemical Etching

This is a process that the plasma discharge gas neutral atoms cause chemical reaction at the surface of the bulk material and due to this reaction, gas-phase products (etchant/volatile products) are being formed from the bulk material. This process is a material selective process and relatively faster than sputtering etching process. Some of the materials and their etchant gases are given in Table 1.3 (Lieberman et al. 2005; Fridman A 2008).

Table 1.3: Materials in Plasma Chemical Etching method and their etchant atoms

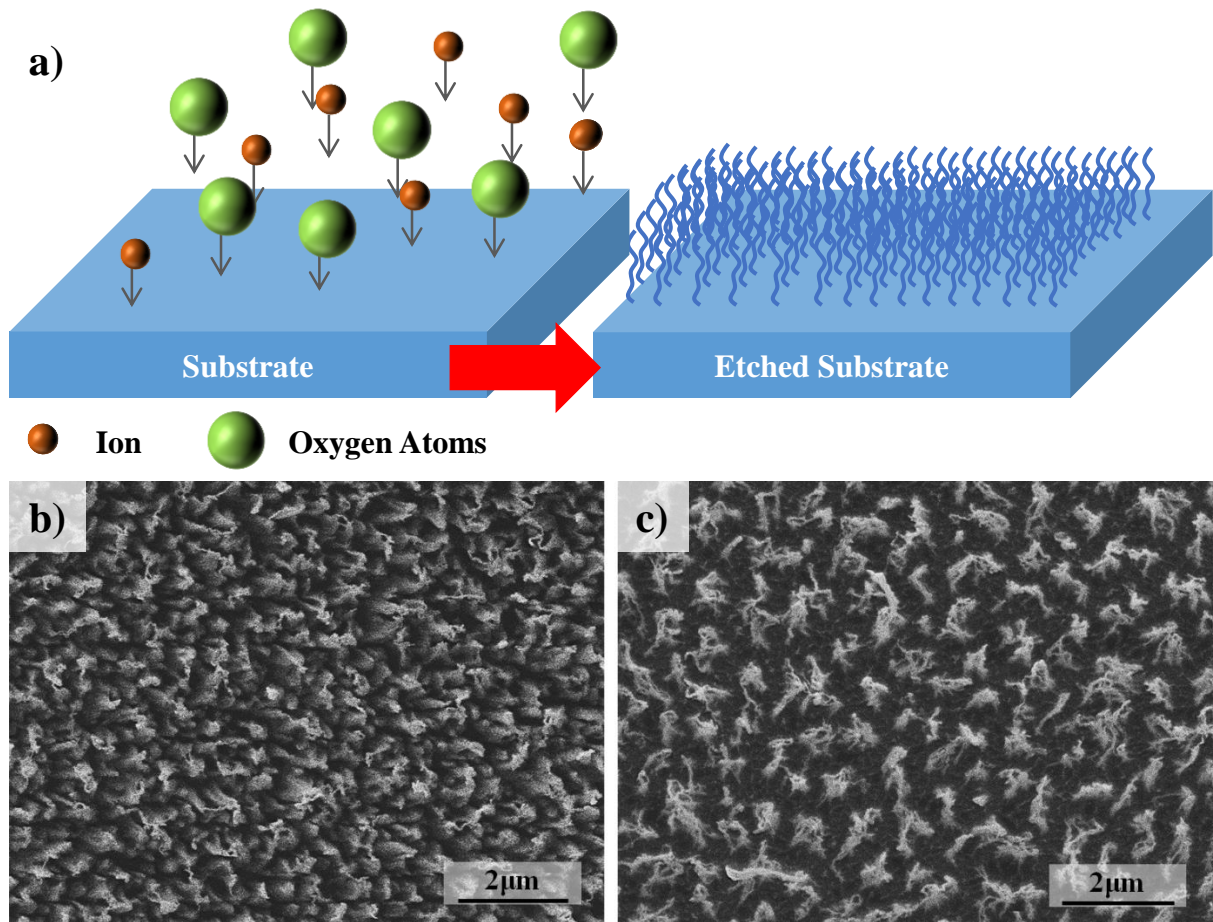| Material	Etchant Atoms
Si, Ge	F, Cl, Br
SiO_2	F, F & C
Si_3N_4, Silicides	F
C, Organics	O
W, Ta, Ti, Mo, Nb	F, Cl

Figure 1.9: a) Schematic illustration of Ion Enhanced Energy Driven Etching process with O_2 etchant gas. Nano/micro size fibers form after the etching of the materials such as PTFE and PEEK. b-c) O_2 plasma etched PTFE and PEEK substrates respectively.

2.2.1.7.3   Ion Enhanced Energy Driven Etching

It is possible to consider this process as a combination of Sputtering and Chemical Etching because of the process itself. In this process the surface is under bombardment of neutral atoms and ions simultaneously. Thus, etching rates with this process is higher and the etchant products are larger in comparison to the sputtering and chemical etching methods. Etching rate for this process is depending on the energy of the bombarding ions. When the applied energy varies, the result will fallow the variation. Illustration of ion enhanced energy driven etching process can be seen in Figure 1.9-a. If O_2 gas is in use for the process as etchant gas, fibers with nano/micro sizes can be produced on several polymer substrates such as Polytetrafluoroethylene (PTFE) and PEEK which is the investigated material in this thesis.

SEM images of PTFE and PEEK substrates etched by O_2 gas plasma can be seen in Figure 1.9-b and -c respectively (Lieberman et al. 2005; Fridman A 2008; Tsougeni et al. 2009).

1.2.1.7.4   Ion Enhanced Inhibitor Etching

In this type of process, addition to the energetic ions and neutral atoms, inhibitor precursor radicals are formed too. These radical are produced by the etchant gases like CF_4, CCL_2 and CCL_3. Etchant radical from these kinds of precursors like CF_2 and CF_3 are deposited over the surface and protect the surface from chemical etching. This kind of deposition occurs only if there is no ion flux inside the plasma. The ion flux prevents the production (decomposition) of such kinds of radicals on the surface or removes these layers if they are already formed (Lieberman et al. 2005; Fridman A 2008).

1.3   Pulsed Laser Deposition

Pulsed Laser Deposition (PLD) is a physical deposition technique for the thin film deposition of various materials varying from polymers to ceramics. One of the main advantages of PLD is to deposit layers with preserved stoichiometry because of high laser pulse energies at short interaction times. Therefore, PLD provides direct deposition of alloys and compounds with identical stoichiometry (Eason R 2007).

PLD was first applied in 1965 by Smith and Turner in order to prepare semi-conductor and dielectric thin films (Eason R 2007). However, rediscovery of the PLD was in 1980s. Since that time, PLD started to increase its popularity with deposition of superconductive oxide films. Today, PLD is one of the most promising and popular deposition techniques in research because of its valuable properties (Gottmann et al. 1999; Krebs et al. 2003; Eason R 2007). These properties can be given as:

- Stoichiometric deposition of material from the target to the substrate
- Environmental flexibility such as vacuum or inert/reactive gas atmosphere
- Enhanced adhesion to the substrate surface and film formation in comparison to the other deposition techniques
- Suitable for multilayer depositions with different deposition materials
- Controllable deposition thickness by controlling the number of laser pulses (10^{-3} Å to 1 Å per pulse) (Svendsen et al. 1996; Willmott et al. 2000; Schou J 2006; Eason R 2007).

1.3.1   Basic Setup of PLD System

Typical setup for PLD applications can be seen in Figure 1.10. Simply, pulsed laser beam gets focused to the target material with a focusing lens which is located at the outside of the chamber with around 45˚ incidence angle. Rotation stage for the target holder can be useful in order to prevent striking several laser pulses to the same location on the target. Otherwise, such a sputtering process can cause inhomogeneous ablation on the target, thus, plasma plume can change its direction and efficiency (Doughty et al. 1995; Bäuerle D 1996). In order to transmit the laser beam into the chamber a glass viewport with high transmission (especially

for UV range of the electromagnetic spectrum) is in used. UV-fused silica glass provides the optimum efficiency due to its high transmission from Deep-UV (DUV) to IR region of electromagnetic spectrum. Transmission curve of such a UV-fused silica glass can be seen in Figure 1.11. When the high influence laser beam hits to the target material, plasma plume occurs and expands towards to the substrate surface in three dimensions. Substrate temperature is also an important parameter for defining the morphology of the grown film. Distance between the target and the sample is kept usually between 3 to 8 cm during the process (Bäuerle D 1996).
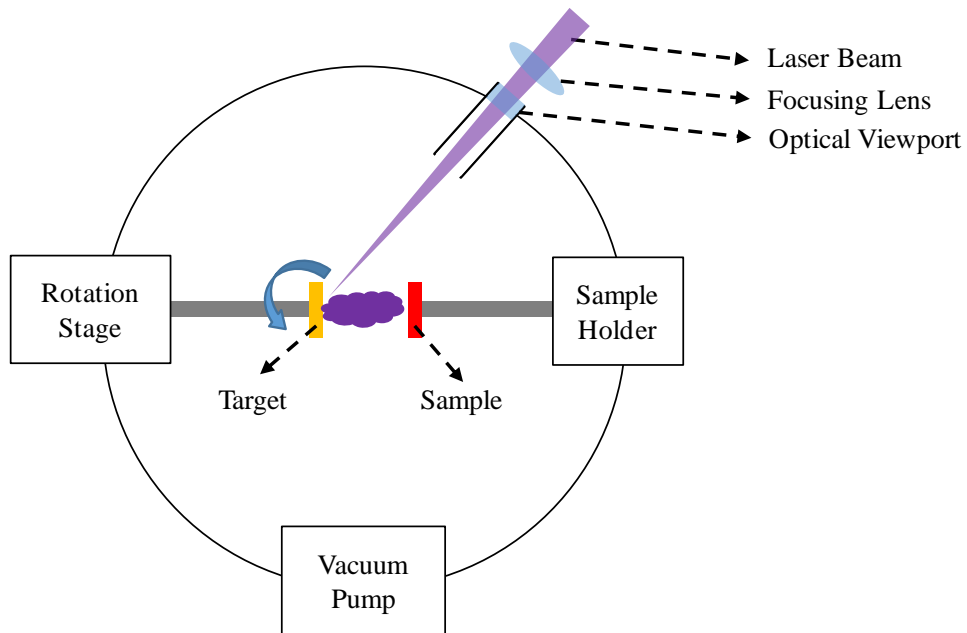
Figure 1.10: Basic schematic of PLD setup. Focused laser beam creates high energy to increase the temperature at the focal area more than the vaporization temperature of the material, thus, the plasma plume occurs and expand to the substrate surface in three dimensions.

For PLD applications, choosing right parameters is extremely important to achieve high quality thin films. One of the most important parameters is the laser wavelength which will interact with the target. Usually, lasers operating in UV range, such: as Excimer Lasers (193 nm, 248 nm) and third or fourth harmonic of Nd:YAG lasers (266 nm, 355 nm), are suitable for most of the target materials because of their low reflectivity from the target surfaces. In some cases IR lasers (10.6 µm-CO_2 laser and 1.06 µm-Nd:YAG laser) can be useful too for deposition (Schou J 2006; Eason R 2007). PLD can be applied at different environments. This can be a reactive gas or inert gas environments as well as the vacuum condition. Such gas atmosphere conditions have also a critical effect on the deposition rate due to the mean free path of the sputtered particles. Effects of the ambient gas pressure on the hardness and on the elastic

module of the deposited alumina films were shown by Gottmann et al. previously (Gottmann et al. 1999; Eason R 2007; Carradò et al. 2011).
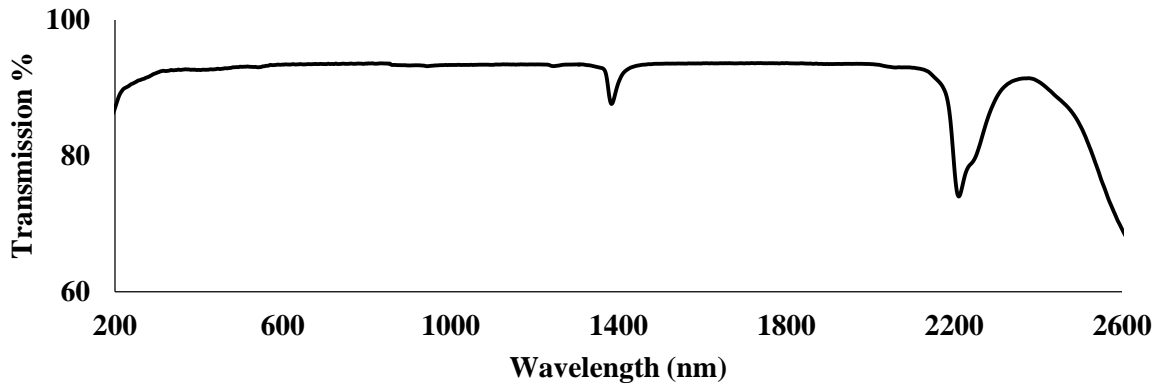
Figure 1.11: Transmission of UV-fused silica glass (Thorlabs Inc 2012).

1.3.2 Plume Formation and Expansion

As it mentioned above, laser pulse creates a plasma plume which is expanding in three dimensions when it hits to the target material's surface. The mechanism behind of the plume generation begins with the absorption of the laser light by the target. This has a critical importance due to the target heating at the focal point. In that case, the wavelength, pulse length and the fluence of the laser beam have critical importance as mentioned in Part 1.1.2 previously. Most of the materials absorb UV light, therefore, UV lasers are the most preferable ones for PLD applications (Schou J 2006; Eason R 2007).

When a laser pulse hits on material surface, some part of its intensity will be absorbed depending on the materials absorption coefficient as one can predict from Beer-Lambert Law (Equation 9) and electromagnetic energy of light will be transformed to heat energy by electronic excitations. This transformation happens for conducting materials by plasmon and unbounded electrons and for insulator by excitons.

$$I(z) = (1 - R)I_0 e^{-\alpha z} \tag{9}$$

Reflectivity may change due to the porous surface or due to the heated surface after several laser pulses to the same location (Bäuerle D 1996). Therefore, intensity absorption on the target may change within time depending on these variations. However, attenuation length/depth "$1/\alpha$" usually stays around 10nm for many materials and it is strongly wavelength dependent.

Therefore, UV lasers are the chosen ones as light sources for PLD applications because of their high absorptivity by most of the materials. When light gets absorbed by the target, the temperature in the laser spot will rise more above the evaporation temperature of the material. Thermal diffusivity "D" is the critical parameter for the surface temperature rise and it is given by:

$$D = \frac{\kappa}{\rho c_p} \tag{10}$$

And heat diffusion length "I_{th}" can be calculated from thermal diffusivity:

$$I_{th} = 2\sqrt{D\tau_L} \tag{11}$$

In these two equations the parameters "κ" is the thermal conductivity, "ρ" is the mass density, "τ_L" is the pulse length of the laser and "c_p" is the specific heat at constant pressure. These calculations are valid only for conducting materials and can be seen clearly that the heat affected depth is more over the attenuation depth. However, for the insulators, the thermal penetration depth is still limited by the attenuation depth itself independent from the heat diffusion length. Therefore the surface temperature rise is much faster than a metal target for non-conductive/insulating materials (Svendsen et al. 1996; Willmott et al. 2000; Schou J 2006; Eason R 2007). Needed time to reach the vaporization temperature "t_v" can be estimated by Equation 12:

$$t_v = \frac{\pi}{4D} \left(\frac{\kappa \Delta T_{eff} \tau_L}{F(1-R)} \right)^2 \tag{12}$$

where F is the laser fluence (Bäuerle D 1996).

After the quick temperature rise at the focal area, some of the material will be ablated from the bulk. Ablation yield (Y) from target is related to the laser influence and to the cohesive energy of atoms. Ablation yield for cohesive energy per atom U_0 is given by:

$$Y = FA/U_0 \tag{13}$$

Here A is the area of the laser beam on the target. This value is usually around 10^{15} particles per pulse for metal targets (Willmott et al. 2000). Ablation rate of atoms per unit area per time "J" from the target material is also given by the equation 14 and it is determined by the evaporation at the calculated surface temperature:

$$J = \frac{P_v}{\sqrt{2\pi A^* k T_s}} \tag{14}$$

Here "P_v" is the vapor pressure at the surface temperature T_s, A^* is the atomic weight (Svendsen et al. 1996; Schou J 2006). When the temperature at the focal spot continues to increase, evaporation of the material may turn into explosive boiling and this causes the nano and micro particle formations on the growing film. This can be observed also when the laser penetration depth is too high (Svendsen et al. 1996; Schou J 2006; Eason R 2007; Bäuerle D 2010).

As it mentioned before, after the particle removal from the target, a plasma layer occurs over the target surface which is so called "Knudsen Layer (Z_K)". This layer can be calculated as:

$$Z_K = \frac{19}{\sqrt{2}n_p\beta} = 19\psi \tag{15}$$

Here n_p is the plasma plume particle density, β is the collision cross section and ψ is the mean free path. Mean free path is proportional to vacuum pressure inside the chamber and can be calculated by equation 16.

$$\psi = \frac{RT}{\sqrt{2}\pi d^2 N_A P} \tag{16}$$

where N_A is the Avogadro Number, R is the ideal gas constant, T is the temperature, P is the environment pressure and d is the particle radius (Bäuerle D 1996). After the plasma layer formation, incoming laser beam gets absorbed by this layer with invers bremmstrahlung. When the laser pulse terminates for each pulse, partially ionized gas layer forms over the target. Thickness of this layer is around 100µm and has temperature more than 10^4 K. This condition causes a great pressure and lets the plasma layer expanded to the sample surface under vacuum adiabatically. Divergence of the plasma plume is defined by "$cos^n\theta$". Here n is the value which defines the order of the divergence. This value changes from 4 to 30 and related to the laser fluence and the spot size over the target surface. Reactive/inert gas environment inside the chamber may change the divergence during deposition. However, only vacuum environment was studied in this thesis. (Eyettand et al. 1987; Weaver et al. 1995; Tyuninaand et al. 2000; Schou J 2006; Eason R 2007; Carradò et al. 2011).

1.4   Cell-Surface Interaction

When a substrate; like an implant material, interacts with a living system, protein monolayer occurs following the protein adsorption on the surface primarily. After this quick protein adsorption, cells come over the surface and detect the specific proteins for adhesion and start to proliferate for tissue forming. However, sometimes they may release their selves from the adhered locations (Ratner et al. 1996). All proteins have their own specific structures and these structures are determined by non-covalent bonds. They are usually found in spherical forms. After the first protein adsorption on to the surface, surface may be enriched for single type of protein and this phenomenon limits the adsorption of further proteins. Some fundamentals of protein adsorption to the surface are:

- Presence of monolayer on the substrate surface
- Surface selectivity to the proteins in living system
- Biological activity of the proteins on the surface
- Concentration of the specific proteins in living system (Ratner et al. 1996)

As summary, properties of the implant surfaces, in combination with the specific properties of each type of protein, influence the protein adsorption to the surface. Therefore, these properties affect the cell adhesion to the surface.

Adhesion of a cell to substrate happens through sensing the surface proteins by partially embedded receptor proteins in the cell membrane which are called integrin. Cells are tending to adhere to the surface adsorbed proteins due to the different biological activity of the surface proteins (Figure 1.12). In addition, cell membrane is also responsible for absorption, secretion, liquid transfer and communication with the other cells (Ratner et al. 1996). Actin filaments inside the cytoplasm enables the movement of the cell on the surface and also enables the cell adhere to the surface through the receptors integrin as mentioned. They are all named as "cytoskeleton". These receptors (integrins) are built of two types of polypeptides which are named as alfa (α) and beta (β). Integrins can attach the cells by connecting themselves to the surface and to some binding molecules inside the extracellular matrix (ECM) like fibronectin and laminin. Here laminin is an adhesive protein which is responsible from the connection of the endothelial cells to the ECM. ECM is the material that is produced by cells which supports the environment to the cell for mechanical supporting, surface adhesion, growing, proliferation and differentiation (Ratner et al. 1996; Walboomers et al. 2001).
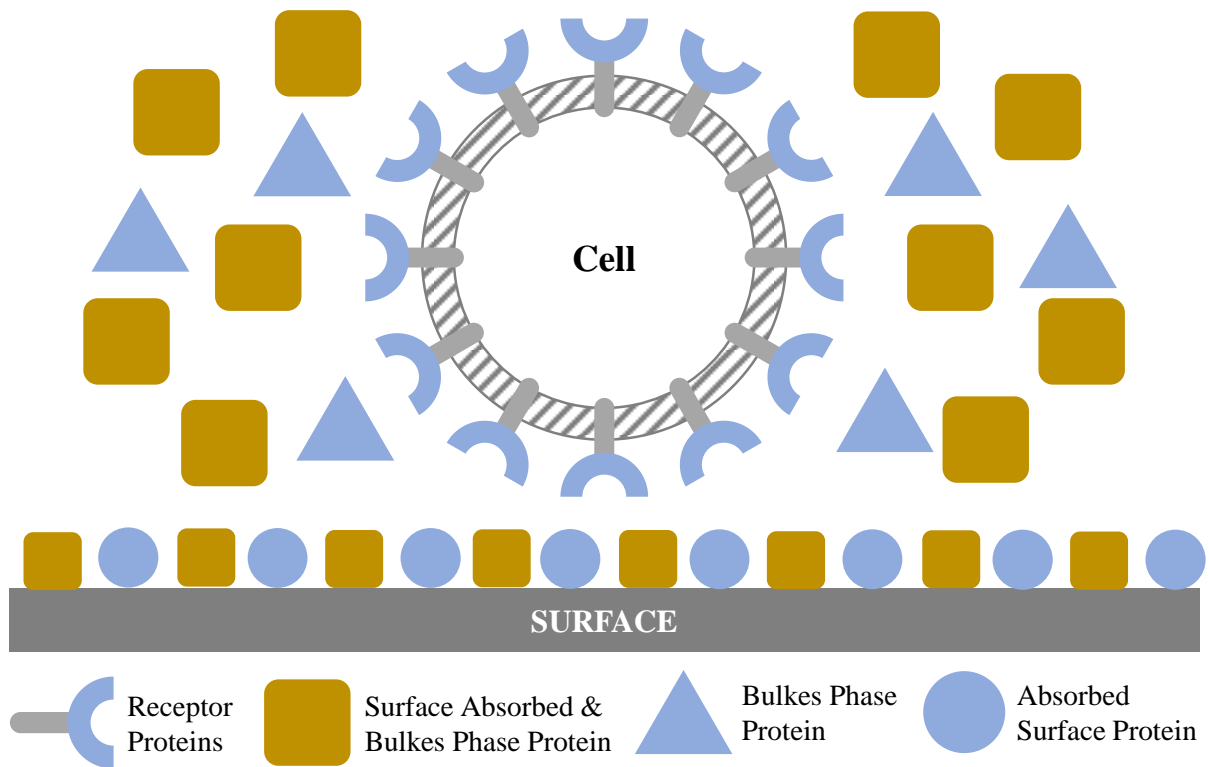
Figure 1.12: Illustration of Cell-Protein binding. Biological activities of the proteins vary if they are adsorbed by the surface or not and this stimulates the cell to adhere to the surface adsorbed proteins. (Ratner et al. 1996).

Adhesion of the cells to the surfaces can be defined with three mechanisms:

- Focal Adhesion: which is the closest and the strongest contact form of adhesion. It performs by integrins at 10 to 20nm distance from the surface.
- Close contact: which happens through the binding proteins between the cell membrane and the surface at around 30nm to 50nm distances. This contact is relatively weaker than focal adhesion.
- ECM contact: Distance in here is bigger than 100nm and cell adheres to the surface through the strands and the cables inside the ECM. (Ratner et al. 1996)

After cell adheres to surface, it starts to spread in all directions until contact inhibition process happens and three main phenomena can give some idea how the cells adhere and spread:

- Cells can directly make connection with the substrate surface by passing the pre absorbed protein layer.
- Cells can attached and spread through the adsorbed proteins.
- Cells can consume the surface proteins in order to make a direct connection. (Ratner et al. 1996)

On the other hand, spreading is influenced by the surface chemistry, surface charge and of course with surface topography. Beside their direct effect on cell spreading, these parameters have effect on the surface free energy. As a common agreement hydrophobic surfaces (low surface energy) lead poor cell spreading while hydrophilic surfaces (high surface energy) are leading satisfying cell spreading. Therefore, wetting properties of the substrate/implant material effect the cell adhesion as well as the spreading too (Ratner et al. 1996; Liang et al. 2005).

1.4.1 Contact Angle Measurement
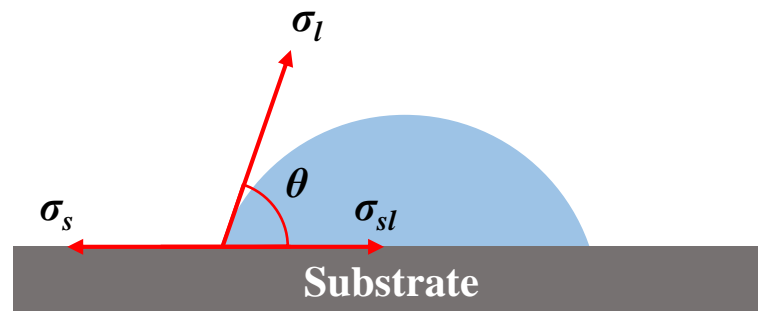
Figure 1.13: Surface energy vectors are used to calculate the contact angle of the surface for the selected liquid (Krüss GmbH 2013)

Contact angle (CA) measurement is the technique to characterize the surface energy and the wetting properties of the investigated surfaces for different kinds of liquids. Every surface exhibits a different CA for every different liquid (Marmur A 2009). Contact angle measurements are based on the Young's equation and it is given as:

$$cos\theta = \frac{\sigma_s - \sigma_{sl}}{\sigma_l} \tag{17}$$

where θ is the measured contact angle, σ_s is the surface tension of solid, σ_l is the surface tension of liquid and σ_{sl} is the tension of solid-liquid interface (Figure 1.13). From here, the surface energy "E_s" at the solid-liquid interface can be calculated by using Equation 18 (Krüss GmbH 2013).

$$E_s = \sigma_l(1 + \cos\theta) \tag{18}$$

Although Young's equation is applicable for ideal surfaces, in nature, surfaces are rough and heterogeneous. In order to define this phenomenon, Wenzel postulated an equation which takes the surface roughness into account. Depending on Wenzel's hypothesis, if the surface is

originally hydrophilic, such a surface tends to show more hydrophilic when it gets roughened. In reverse, if the surface is originally hydrophobic, such a surface tends to show more hydrophobic when it gets roughened. This is phenomenon defined by the Equation 19.

$$\cos \theta_W = r \cos \theta_Y \tag{19}$$

Here θ_Y is the Young's contact angle and r is the roughness factor (Wenzel RN 1936; Marmur A 2003; Quéré D 2008). The logic behind the Wenzel Law is: total wetting area increases when the surface roughness increases, thus this factor enhances the wetting property of the surface (Figure 1.14-a). On the other hand, as it mentioned above, surface are not perfectly homogeneous in nature. Thus, Cassie and Baxter derived another formula to estimate the wetting angle of the heterogeneous surface which is called simply "Cassie State". In their work, a surface with two different materials was investigated and the contact angle calculation for such a system can be given by Equation 20:

$$\cos \theta_{CB} = f_1 \cos \theta_1 + f_2 \cos \theta_2 \tag{20}$$

where f_1 and f_2 are the surface fractions ($f_1+f_2=1$), θ_1 and θ_2 are the contact angles of different materials alone. If one of the fractions is taken as air gap between the structures (Figure 1.14-b) then the equation transform to 21:

$$\cos \theta_{CB} = f_s(\cos \theta_Y + 1) - 1 \tag{21}$$

where f_s is the fraction of the solid part on the surface (Marmur A 2003; Ran et al 2008). However, since these two equations are the most cited ones by the scientists, there are different investigations to understand wetting properties of different surfaces. Ran et al. investigated the transition between Wenzel and Cassie states by using alumina substrates with different pore diameters and structure depths. They showed that when the pore diameters are increased, wetting property shift from Wenzel to Cassie state due to the compression forces in upper direction at the air gaps while the structure depths are unique. The same result was observed also when the depth of the structures are increased while the pore sizes are kept identical (Ran et al 2008). Extrand et al. and Gao et al. questioned the Wenzel and Cassie states with different experiments. Depending on their experiments contact angle is the function of the contact line of liquid with the surface, while Wenzel and Cassie were proposing that the contact angle is in relation with the contact area under the liquid (Extrand CW 2003; Gao et al. 2007).
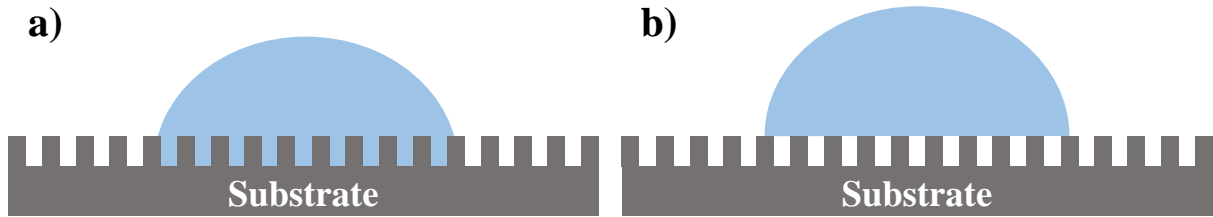
Figure 1.14: Illustration of a) Wenzel and b) Cassie-Baxter wetting states

To measure the contact angle of a surface, a camera system with software supported is in use to record the shape of the liquid on the surface. There are two different measurement methods for contact angle: Static and Dynamic Measurements methods.

1.4.1.1 Static Contact Angle

In this method a drop of liquid is placed on to the substrate surface and contact angle measurement is performed without any movement of the drop. However, drop may change its shape with in time due to some external factors like evaporation of the liquid or chemical reactions with surface material. Therefore, the time for the image capturing has to be selected depending on the desired measurement. Static method has also an advantage over the "Dynamic Contact Angle" measurement which will be explained continuously where the liquid injection pipette does not stand during the image capturing, thus, the drop is not affected by the pipette. (Krüss GmbH 2013)

1.4.1.2 Dynamic Contact Angle

In this method, water droplet on the surface increases or decreases with the pipette while pipette is still inside the liquid. In this method, the flow rate of the liquid must be controlled in order to get a realistic result. Dynamic contact angle measurement method is divided into two sub-methods where they needed to be measured and analyzed together.

- Advancing Angle: In this measurement, liquid drop volume increases while the pipette is inside the drop. When the drop shape stays stable with the increased volume, the contact angle measurement performs.

- Receding Angle: In this measurement, increased liquid volume (during the advancing angle measurement) decreases with a constant flow rate while the pipette is inside the liquid.

It is possible to calculate the roughness of the surface or the in-homogeneities at the surface with the combination of these two measurement method (Krüss GmbH 2013). As it previously, surface contact angle influences the cell-surface interaction. Because of the same reason, surface energy has to be controlled precisely in order to provide a good biocompatibility (Ratner et al. 1996).

1.4.2   Biocompatibility of PEEK and Alumina Substrates

Biocompatibility term is in use to define a material which does not induce any inflammation and never causes a tissue differentiation around the material itself. Depending on the usage area, different cell behavior to the surface is desired. Teflon vascular prosthesis where it's both surfaces show different behavior to the blood and tissue can be given as example. As can be understood from here, surface energies of the implanted materials have to be controlled precisely (Ratner et al. 1996; Liang et al. 2005).

There are various materials such as polymers, metals, ceramics or their surface modified versions for the implantation (Ratner et al. 1996; Liang et al. 2005). Roughly, there are three kinds of biomaterials:

- Inert or relatively inert biomaterials
- Bioactive materials where the implant surfaces are modified with several methods
- Biodegradables which are degrading inside the body with in a certain time

Alumina is one of the biomaterial which is used for the hip and knee implants in human body as well as titanium and its alloys (still favorite for implantation). As well as the hip and knee replacements, alumina is used for femoral implantation and in the past it was used for dental implantation as single or poly crystalline form as well (Cordingley et al. 2003; Kurtz et al. 2007). Furthermore, it was pointed that the porous alumina can be used to replace large section of bones (Carradò et al. 2008).

The reason for the choice of alumina as implant material is lying behind its chemical and mechanical properties such as: inertness, hardness, low friction, possible for fine polishing and good biocompatibility inside the body (Carradò et al. 2008; Molloy et al. 2012). Although

there are many literatures available about the usage of alumina as implantations, applying in vitro tests, which is a method to understand the behavior of a certain material for the specific cell types outside the body in the mean of surface chemistry and topography, are necessary to understand the properties of the new developed implants. For this technique cell culture models are being applied (Liang et al. 2005). In this purpose several in vitro tests were performed with alumina surfaces. Veith et al. pointed out the usage of one dimensional Al/Al_2O_3 NWs for biological applications (Aktas et al. 2011; Aktas et al. 2012; Veith et al. 2012; Lee et al. 2013). By following his previous works, Aktas et al. pointed out that the Human Umbilical Vein Endothelial Cell (HUVEC) and Human Umbilical Vein Smooth Muscle Cell (HUVSMC) cell types can be controlled over Al/Al_2O_3 NWs which can be effective for selective adhesion of one type of cell. They used standard glass, micro-structured alumina plate and Al/Al_2O_3 NWs with two different densities for the cell culturing. They observed that it is possible to control the proliferation and adhesion of these two kinds of cells on Al/Al_2O_3 NWs which leads to a selective cell adhesion (Aktas et al. 2012). Veith at el. pointed the same result in his review (Veith et al. 2012). Similarly, Aktas et al. investigated the fibroblast cell behavior to the same Al/Al_2O_3 NWs. They compared the Al/Al_2O_3 NW coated glass substrates with fibronectin coated glass substrate for fibroblast adhesion tests. They observed that Al/Al_2O_3 NWs shows strong fibroblast adhesion similar like fibronectin coated glass substrates (Aktas et al. 2011). Another fibroblast study by Veith et al. is about the effect of micro and nano features over the surface where Al/Al_2O_3 surface was treated with the laser pulses. They observed that the fibroblast cell density increases when the surface is covered with combination of micro and nano features where the surface supports good environment for cell proliferation (Veith et al. 2010b). By using the same material, Lee et al showed the guidance of the axon of Dorsal Root Ganglion (DRG) cell along the grooves which were realized by laser interference lithography technique on Al/Al_2O_3 NWs (Lee et al. 2013). Webster et al. reported enhanced osteoblast cell adhesion on alumina NWs in comparison to glass substrate (Webster et al. 2005). On the other hand, zirconia doped hydroxyapatite ($Ce-ZrO_2$:HA) layers sputtered on porous alumina with PLD had been tasted in cell culture model with mesenchymal stem cells (MSC) and well attachment, spreading and surface covering on material was observed (Carradò et al. 2008). Another PLD study for the deposition of bioactive material is investigated by Bajpai et al.. They sputtered HA over 316 stainless steel rather than using Ti-6Al-4V implant material in an alumina matrix. They used alumina in this sputtering target to increase the strength and stiffness of the deposited HA layer (Bajpai et al. 2010).

As well as the ceramics and metals, polymers are also used for surgical and dental implants as mentioned. Polyethylene (PE) is used for joint replacements while silicones, elastomers and polyether urethanes are used for the devices where contact with the blood is established. On the other hand, acrylic polymers are used for bone cements and dental implants (Williams et al 1987; Kang et al. 2012). Pashkuleva et al. tested poly [ethylene-co-(vinyl alcohol)] copolymer, poly (e-caprolactone) and cellulose acetate using osteosarcoma cells. Before seeding the cells, they treated the substrate surfaces with UV irradiation and separately with O_2 plasma too. They observed that the cell adhesion and proliferation rates are higher than the non-treated surfaces for all polymer types. Additionally, cellulose acetate substrate showed successful result at in vivo test and they pointed out the nano scale roughness of the surfaces for such a result (Pashkuleva et al. 2010).

PEEK is another thermoplastic which is also used in medical implants. Chemical inertness, mechanical stability, high temperature resistance and excellent biocompatibility at in vitro tests makes PEEK a favorable material for implantation. Today PEEK and its product family PAEK: (Poly-aryl ether ketone), PEKEKK: (Poly-ether ketone ether ketone ketone) and carbon fiber reinforced PEEK are being used in total hip replacement rather than Ti, in femoral stems, in arthroplasty, in spinal implants and as bearing surface of hip and knee implants rather than polyethylene (Ferguson et al. 2006; Kurtz et al. 2007; Williams D 2008). The reason of using PEEK rather than Ti or alumina implants for these surgical replacements is the physical and chemical properties of it. While PEEK supports the bone growth, possible bone and implant damages inside the body can be minimized in comparison to Ti due to its close Young module to human bone (Sagomonyants et al. 2008). Additionally, X-ray and Gamma Ray transparency of PEEK lets the medical doctors investigate the bone growth behind the implant with these examination methods where it is impossible with the metallic implant (Kurtz et al. 2007; Williams D 2008). On the other hand, PEEK finds application fields in the cardiovascular implantations. Wheatley et al. mentioned about the usage of PEEK as frame material for the polyurethane hearth valve prototype (Wheatley et al. 2000). Kubena et al. published a patent on the field of a self expanding stent made out PEEK to use for predominantly in the esophagus, intestines, biliary ways and air ways (Kubena et al. 2012)

Although PEEK can be used directly, a surface modification can make PEEK much compatible with the tissue. It is known that Ti and HA coated PEEK implants show improvement at the bone-implant interface (Kurtz et al. 2007). As known that the contact angle of the surface has a correlative relation with the blood which means cell and tissue contact,

therefore, some plasma surface modifications were done on polymers in order to enhance their biocompatibility (Haa et al. 1997; Kurtz et al. 2007; Bazaka et al. 2011). It is suggested by Haidar et al. with oxygen rich surfaces it is possible to enhance the endothelial cell adhesion (Haidar et al. 2011). Similarly, PEEK surface was treated with oxygen plasma by Ha et al. in order to enhance the bone bonding to the PEEK via increasing the adhesion strength between plasma treated PEEK and calcium phosphate coating solutions (Haa et al. 1997). On the other hand, laser surface modifications were performed on PEEK substrates in order to enhance the wetting property of the material for the increased cell adhesion (Riveiroa et al. 2012).

1.4.2.1   Biocompatibility of Organic and Inorganic Materials for Endothelial Cell

Endothelial cells (ECs) are the natural cells that they cover the inner side of the blood vessels, thus, enhanced endothelialization is important for the long term usage of vascular implants. However, abnormal proliferation of smooth muscle cells (SMCs) over the implant surfaces seems to be one of the reasons which cause thrombosis (Khang et al. 2008; Aktas et al. 2012; Oberringer et al. 2013). In order to prevent this factor, fast endothelialization is important, for example, surface modification of stents can be a solution to prevent this problem for stent implantations. In this content, different surface modification techniques were performed over different kinds of materials. Aktas et al. experienced the nano and micro structured surfaces for controlling of the EC and SMC and they observed that the EC proliferation increases with the smaller nano features (Aktas et al. 2012; Veith et al. 2012). Sprague et al. indicated that, creating micro grooves to the inner side of the stent in the direction of blood flow can increase the EC proliferation rate while decreasing the apoptosis rate (Sprague et al. 2012). Khang et al. used another method to investigate the rat aortic endothelial cells (RAEC) reaction to the Ti stents by surface structuring. They deposited Ti layer over glass substrates with different roughness values and structures. They observed 216% increasing on the sub-micron surface structures and 58% increasing on the nanometer scale surface structures for the cell densities in comparison to the smooth Ti layer (Khang et al. 2008). Oberringer et al. structured stainless steel surfaces with femtosecond laser; which is used as stent material, in order to understand the human dermal micro vascular endothelial cells (HDMEC) reaction to the surfaces with different structure densities together with fibroblast cells. In their experiments, they observed that the fibroblast cells differentiated to miyofibroblast (MF) cells and low density structures show non-disturbed EC proliferation while decreasing the MF proliferation

rate (Oberringer et al. 2013). Similarly, Haidar et al. examined the surface oxygen amount effect on HUVEC and HUVSMC proliferation on stainless steel substrates for intravascular implants. In this content they introduced a thin SiO_x layer over substrate surface and compared with the non-treated one. They observed that the oxygen rich surfaces show better HUVEC proliferation and adhesion while HUVSMC proliferation rate was reduced in compare to the non-treated surfaces (Haidar et al. 2011). Introducing TiO_2 layer over the implants like artificial heart valves and stents is another approach for the cardiovascular implants from inorganic materials. It is reported that such a layer decreases the platelet adhesion to these surfaces (Chu et al. 2002).

As well as the metals, polymers are also in use with blood contact implants such as artificial blood vessels and heart valves. Dacron (polyethylene-therephtalate (PET)) and e-PTFE (Polytetrafluoroethylene) which is known as Goretex are the materials which are in use for such kinds of implants (Chu et al. 2002). However, due to their non-satisfactory results on blood contact, their surfaces have to be treated in order to support immobilization of anti-thrombogenic moieties like fibronectin, laminin, collagen and peptides which are involved for a good EC seeding to the surface (Dekker et al. 1992; Chu et al. 2002). Plasma surface modification is a key method which can support necessary surfaces for such applications. Dekker et al. observed that the surface modification of PTFE with oxygen and nitrogen plasmas is enhancing the HUVEC adhesion to these surfaces in comparison to non-treated PTFE. Additionally, they reported that the amount of the adhered cells to the plasma treated surfaces (after 6 hours of cell culturing) is similar to Tissue Culture Polystyrene (TCPS) which is a well-known cell culturing plate (Dekker et al. 1992). Another study with PTFE from Dekker et al. indicated that the human serum albumin (HSA), human immunoglobulin (IgG), human high-density lipoprotein (HDL) in %20 serum containing culture medium show increased adsorption on the plasma treated PTFE surface and human fibronectin (Fn) adsorption to the surfaces increased with the increasing of the surface wettability (Dekker et al. 1991). Additionally, they observed that the plasma treated surfaces shows improved cell spreading while there was almost no spread cell over non-treated one (Dekker et al. 1991; Dekker et al. 1992). Althaus et al. studied the adhesion and proliferation of HDMEC's and Adipose tissue derived stem cells (ASCs) over micro and nano structured PEEK surfaces. They used micro injection technique for the production of micro structures (as grooves) and plasma etching technique for the production of nano structures. They used ammonia and oxygen in addition to argon gas for the plasma etching. They observed that, both cells adhere and proliferate much better on plasma treated surfaces in comparison to the non-treated ones. Similar to Dekker et al, they compared the TCPS with the plasma treated surfaces and observed that the processed surfaces are

promising in cell surface interactions. Additionally, they reported that the ASC's aligned over micro grooves with 20 μm width and 1 μm depth (Althaus et al. 2012).

Biodegradable polymers are another type of materials used for the cardiovascular implants, like vascular tissues and stents. poly-L-lactic acid (PLLA), poly(glycolicacid) (PGA) and PGA coated PLLA are in use of reconstruction of vascular tissues (Chu et al. 2002). Chu et al compared the non-treated PLLA, Fn coated PLLA, ammonia plasma treated PLLA and Fn coated plasma treated PLLA for the cell adhesion of HUVEC and rabbit micro vascular endothelial cell (RbMVEC). They observed that the plasma treated PLLA substrate shows much better cell growth in comparison to non-treated and Fn coated substrates. Additionally, cell growth rate was enhanced after Fn coating over plasma treated surfaces (Chu et al. 1999; Chu et al. 2002). Previously, in order to increase the efficiency of the metallic stent, drug elution was used and named as Drug Eluting Stents (DES). However, when the effectiveness of the introduced drug to the stent surface is over, thrombosis and restenosis appears with in the following time because of the presence of the stent inside the vein. In order to prevent this phenomena biodegradable stents were introduced where they may contain drugs in their porous body and get disappear in human body (Ratner et al. 1996; Kwon et al. 2012). PLLA (poly-L-lactic acid) is one of the biodegradable polymers for stent production (Liu et al. 2010; Kwon et al. 2012). Liu et al. used another biodegradable polymer poly(ε-caprolactone) (PCL) to produce stent which is a semi-crystalline polymer and having good flexibility at 37˚C (Liu et al. 2010).

Within this concept, several substrates which are Al/Al_2O_3 NWs, bulk alumina plates, Alumina coated plasma and laser treated PEEK substrates were prepared and endothelial cell behavior over these substrates was investigated in this thesis.

1.5   Aim of the Work

Following the improvement in the implantation technology, polymers were started to use in implantation as well as the ceramics and metals. However, their surfaces may need to be treated with several methods to improve their biocompatibility as mentioned above previously. Unfortunately, due to their physical properties, polymers are not suitable to be modified with high temperature modification methods. Therefore, surface modification of polymers has to be carried out at low temperatures. Techniques such as laser and low pressure plasma methods are effective to modify polymer surfaces in this way. In this context, laser surface modification and plasma surface modification techniques were planned to modify PEEK surfaces where the modified surfaces were planned to compare with the biologically proved and tested materials which are alumina and Al/Al_2O_3 core/shell nanowires. Laser surface modification was divided into two sections such as: Surface Structuring and Pulsed Laser Deposition.

The specific aims can be sort as:

1) Investigation of the laser parameters for the surface structuring of PEEK, alumina plate and Al/Al_2O_3 core/shell nanowires.

2) Investigation of the plasma process parameters for the etching of the PEEK substrates (effects on fiber growth)

3) Investigation of the process parameters for PLD of alumina on PEEK surface types where the PLD of alumina was planned to support identical chemistry on PEEK substrates.

4) Investigation of the biological performance of the prepared PEEK and alumina surfaces for endothelial cells growth factors.

5) Comparing the prepared PEEK surfaces with alumina substrates; which have the same surface structures, for endothelial cells growth factors.

2 MATERIALS AND METHODS

2.1 Materials

2.1.1 PEEK

PEEK substrates were ordered from the company Goodfellow (Germany) where they have poly-aromatic linear, semi-crystalline structure. PEEK is a thermoplastic polymer and it can also exist in amorphous form (Jenkins MJ 2000). It is a promising material in different fields due to its physical and chemical properties. PEEK has high melting (T_m: 343˚C) and glass transition (T_g: 143˚C) temperatures which make it suitable for processing and machining too (Harsha et al. 2003; Narushima et al. 2009; Goodfellow Corporation 2012; Victrex Manufacturing Limited 2012). Because of its good mechanical properties, it is used in aerospace, marine and microelectronic industry. Furthermore, its high strength with relatively low Young's module, additional to its inertness, makes it suitable to use in bone implants rather than metals and alloys (Green et al. 2001; Feng et al. 2003; Sagomonyants et al. 2008; Song et al. 2008).

For the following experiments, PEEK substrates were cut into pieces of 10 mm* 10 mm squares for the following experiments. Physical properties of the PEEK that was used in this dissertation can be seen in Table 2.1. Captured image of a PEEK plate and its chemical structure can be seen in Figure 2.1.

$$[-C_6H_4-CO-C_6H_4-O-C_6H_4-O]_n$$
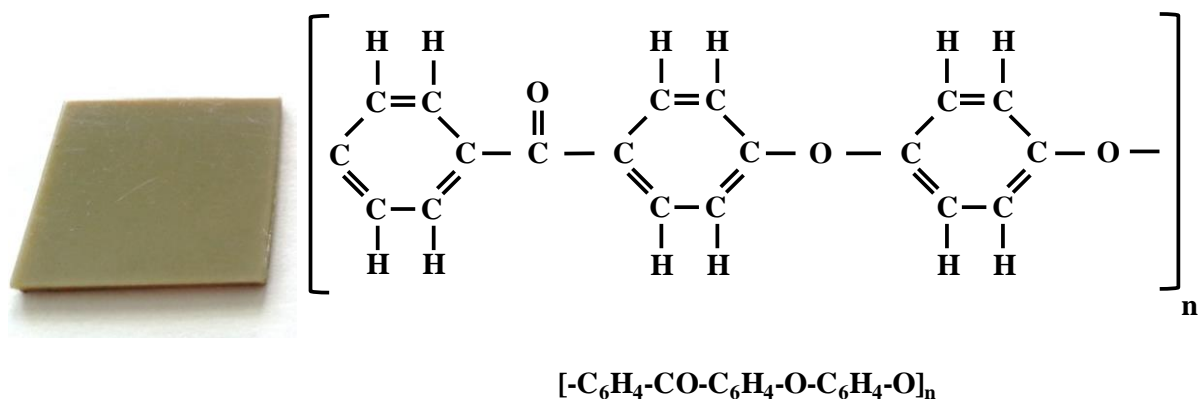
Figure 2.1: Captured image of PEEK plate (on left) and chemical structure with the chemical formula below (on the rigt)

Table 2.1: Properties of α-Alumina and PEEK material which had been used in this thesis
*: General properties for α-Alumina and PEEK (Goodfellow Corporation 2012)

		α-Al$_2$O$_3$	PEEK (Semi-Crystalline)
Density (g/cc)		3.9	1.26 - 1.32
Water Absorption (%)		0.0	0.5
Tensile Module (GPa)		350	3.7 – 4.0
Coefficient of Thermal Expansion (ppm/K)		6.8 (293.15 - 473.15 K) 8.5 (293.15 - 1273.15	47 (<T$_g$) 108 (>T$_g$)
Thermal Conductivity (W/m K)		$\geq$ 26	0.25
Dielectric Constant		10.1 (@ 1 MHz)	3.2 (@ 1kHz)
Volume Resistivity (ohm cm)		$\geq 10^{13}$	10^{16}
*Chemical Resistivity	Acids – concentrated	Good	Good-Poor
	Acids - dilute	Good	Good
	Alkalis	Good	Good
	Alcohols	Good	Good

2.1.2 Alumina

α-Alumina plates which were used in this thesis were ordered from the company Ceramtec GmbH (Germany) and α-alumina target for the PLD application was order from the company Kurt J. Lesker (United Kingdom). Aluminum oxide (or Alumina) is one of the most favorite materials for engineers. Like most of the ceramic materials, it is also chemically inert and has high melting temperature (2050˚C_α-Alumina) (Smith WF 1996). They are used in automotive industry, electronic device production, cutting tools, barrier layers as coatings and in medical field as implant materials due to their electrical and high thermal resistivity, chemically inertness, hardness, corrosion resistance and good biocompatibility (Ratner et al. 1996; Liang et al. 2005; Boumaza et al. 2009). Although there are different phases of alumina, most known type is alpha alumina (or corundum) (α-Al$_2$O$_3$) which has hexagonal close packed crystal structure. Aluminum atoms are placed in octahedral coordinates between oxygen atoms in ratio of two-thirds (Boumaza et al. 2009; Feret et al. 2000; Chemicalland21 2012). Corundum can be found in nature as transparent. Ruby and sapphire are some kind of corundum and they have their specific color from impurities inside (for ruby: chromium, for sapphire: iron, titanium) (GEO 347K 2012). Some other phases of alumina can be listed as γ-, η-, θ-, κ-, χ-, β-

and δ- which are so called transition alumina and they are metastable unlike α-alumina. Ordered alumina substrates were cut into 10 mm*10 mm squares similar to PEEK substrates. Properties of alumina that used in this thesis are given in Table 2.1 (Patnaik P 2003; Boumaza et al. 2009; Aktas OC 2009).

2.1.3 Al/Al$_2$O$_3$ Core/Shell Nanowires

Deposition of Al/Al$_2$O$_3$ core/shell nanowires (NWs) were performed by CVD technique over 12 mm diameter microscope coverslips. Depositions were performed at 10^{-2} mbar pressure and at 600˚C substrate temperature. Thicknesses of the deposited NWs were kept around 750 nm.

2.2 Material Processing

2.2.1 Deposition of Al/Al₂O₃ Core/Shell Nanowires

Al/Al$_2$O$_3$ NWs consist of two materials where Al is standing as core inside an alumina shell. These nano structures were synthesized by Veith et al. at 600˚C from the decomposition of a single source precursor (^{t}BuOAlH$_2$)$_2$ by CVD technique (Veith et al. 1996a; Aktas OC 2009; Veith et al. 2010a; Lee et al. 2013). Precursor was synthesized by Veith et al. with the following steps: first of all 120 mmol of LiAlH$_4$ was dissolved in 80 ml of diethyl ether inside a cooler flask. Following this step, 40 mmol of aluminum trichloride was dissoleved in 80 ml diethyl ether inside a cooler flask and added in to the LiAlH$_4$ solution at room temperature. After that, lithium chloride was precipitated. 160 mmol of tert-butanole is added in to the rest of the solution and waited four to five hours for hydrogen production. After that lithium chloride is filtered and the solvent evaporated under vacuum of 10^{-3} bar at ambient temperature (Veith et al. 1996b; Aktas OC 2009)
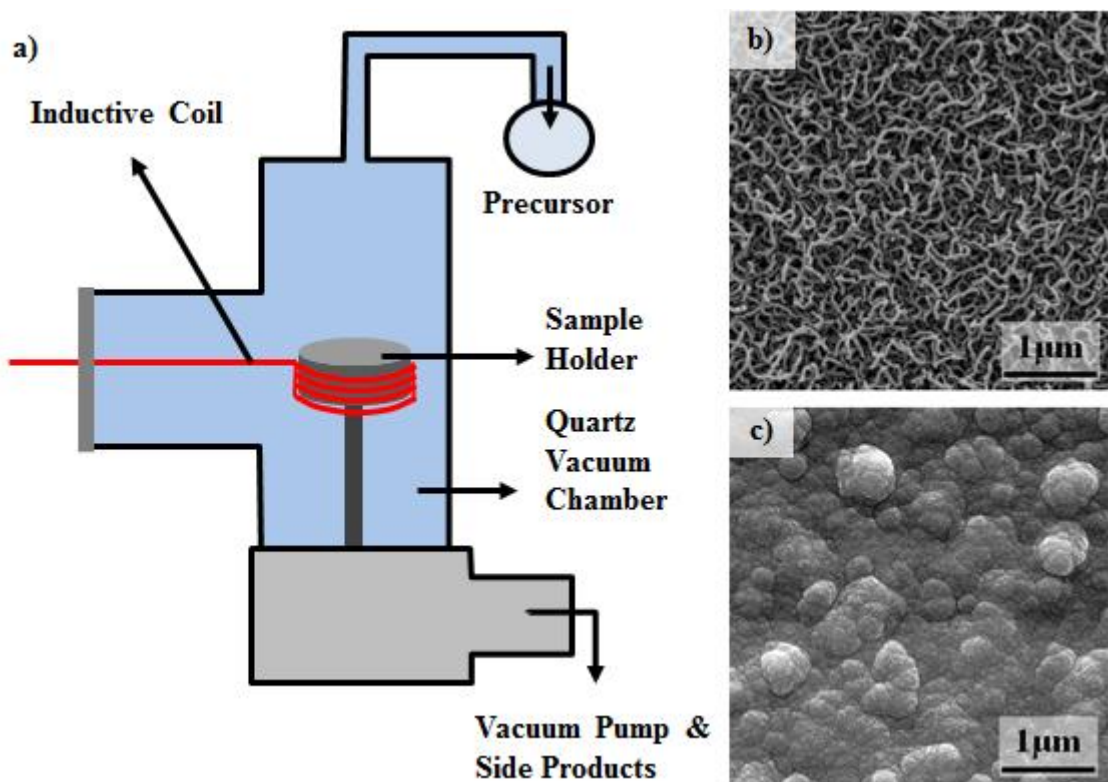
Figure 2.2: a) Schematic illustration of CVD device for the synthesizing of NWs on glass substrates. b) Decomposition of (^{t}BuOAlH$_2$)$_2$ at 600˚C sample holder temperature for NW structures, c) Decomposition of (^{t}BuOAlH$_2$)$_2$ at 300˚C sample holder temperature for nano ball structures (Veith et al. 2010a; Veith et al. 2012).

During the deposition of (^{t}BuOAlH$_2$)$_2$ single source precursor, the process parameters have high importance which are deposition time, substrate temperature and vacuum pressure. It was shown before that with this precursor, it is possible to deposit different kinds of structures over substrate surface by varying the deposition temperature. A comparison of temperature difference for the depositions is given in Figure 2.2 additional to the schematic illustration of the deposition chamber which was used in this thesis (Veith et al. 2010a; Veith et al. 2012).

2.2.2 Plasma Surface Structuring

Plasma etching experiments were done with a fully automatic commercial device (Plasma Electronics GmbH/Germany) which is coupled with a 13.56 MHz RF generator and several gas and precursor inlets in order to work with different process gases where they can be used for etching and plasma deposition (PECVD). Vacuum chamber has a cubic design and can be evacuated down to a pressure of 0.001 Pa. Electrode inside the vacuum chamber can be adjustable in size for the desired substrate dimensions. Additionally, small electrode is equipped with a ceramic heater which can provide different substrate temperatures during the processing.

Table 2.2: Plasma surface structuring parameters on PEEK substrates for optimum parameter investigation and defined plasma structuring parameters for final applications

RF Power (W)	20	20	30	40
Process Gases and Time	Ar / 5 min	O$_2$ / 55 min		
Gas Flow (sccm)	25	100	250	400
Defined Parameters	100 sccm at 30 W RF power			

During the experimental work of PEEK processing by plasma, three different RF power and three different O$_2$ gas amounts were investigated in order to understand the effects of process parameters on PEEK substrates. PEEK substrates were cut into size of 10 mm×10 mm and placed over 5 cm×5 cm electrode after surface cleaning with ethanol. In order to protect the substrate surfaces from additional scratches during the cleaning, optical grade soft tissue papers were used where they normally used for cleaning sensitive optical components like lenses, polarizers or beam splitters. After placing the substrates, the chamber evacuated down to pressure of 1 Pa and this pressure was set as the starting pressure for all experiments.

Process time was fixed to 1 hour and each experimental parameter was repeated for three times. When the base pressure is reached, process started with Ar gas plasma for 5 minutes which is used for secondary surface cleaning in order to remove any organic contaminations from the surfaces. After the secondary cleaning of the surfaces, Ar gas flow stopped immediately and O_2 gas started to flow which is the main process for the entire experiments. Process parameters are given in Table 2.2 and photo of plasma device with etching process image can be seen in Figure 2.3. Defined plasma processing parameters from these entire experiments were applied to the PEEK surfaces for cell culturing experiments (Table 2.2).

Figure 2.3: Plasma device and the image of the O_2 etching process.

2.2.3   Laser Surface Structuring

2.2.3.1 Single Lens Surface Structuring

A microlens array (Thorlabs) was used for the laser surface treatment experiments which can perform more than 4000 identical structures over substrate surface. However, because of the short focal length of the microlens array, a new optical system was designed to protect the lens surface from the back sputtering where the back sputtered alumina particles can cause scratches on the lens surface during periodic cleaning. Microlens array system and the new optical setup can be seen in Figure 2.4. New optical setup consists of a single focusing lens which is in combination with an iris diaphragm and a neutral density (ND) filter. After the

design, new laser output energies were recalculated depending on the planned energy values which should be applied later on. General optical setup and the laser properties/energies are given in Figure 2.4 and Table 2.3 respectively.
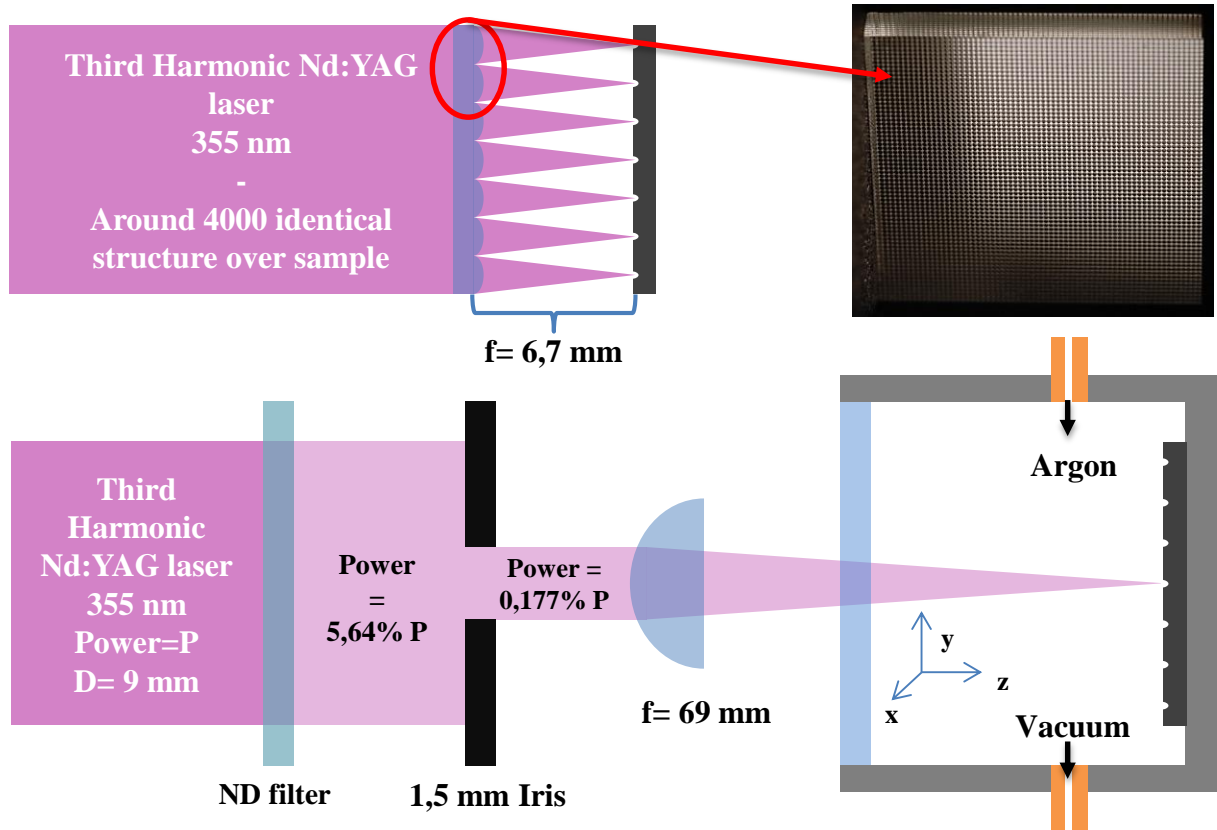
Figure 2.4: Schematic illustration of microlens array optical setup (up) and singlet lens optical setup (down).

Laser source which is used in this thesis is a pulsed solid state Nd:YAG laser (Spectra-Physics Quanta-Ray Pro Series) with around 10 ns pulse duration in average (varies due to the harmonic generator). The operation frequency can vary between 9-11 Hz and all the experiment were done with a fixed 10 Hz repetition rate. As processing wavelength, 355 nm was selected due to its low thermal effect on PEEK polymer as shown at Figure 1.3. Riveiro at al reported the same result with an addition of fundamental wavelength of Nd:YAG laser (1064 nm) (Riveiroa et al. 2012).

Table 2.3: Specification of Quanta-Ray Pro Series laser and applied parameters for single lens experimental procedure (Newport Corp. 2012b)

Repetition Rate (Hz)	10								
Energy @ wavelength	2J @ 1064 nm		1J @ 532 nm		0.55J @ 355 nm		0.18J @ 266 nm		
Pulse Width (ns)	~ 10								
Beam Diameter (mm)	< 10 (~9)								
Linewidth (cm^{-1})	< 0,003 @ Injection Seeded								
Material	PEEK				Al_2O_3				
Energy (mJ)	1.3		2.2	4.5	4.5		8.9		13.3
Number of Pulses (#)	1	5	10	15	20	15	20	25	30	35
Wavelength (nm)	355								
Repetition Rate (Hz)	10								
Environment	Air		Vacuum			Argon			

Laser energies for drilling/structuring process were reduced at the new optical setup. Corresponding calculations are given below. As can be seen in Figure 2.4, PEEK and alumina substrates placed continuously inside a compact vacuum chamber and the chamber is mounted on a three axis translation stage which can move in positive and negative directions with a maximum 4.5 mm/s speed and < 50 μm resolution. Vacuum chamber has two ports for vacuum and argon gas inlets. For the vacuum experiments, vacuum level was adjusted to 10^{-2} mbar and for argon flow experiments the chamber was filled with pure argon gas (5.0 pure) till the argon gas flow out from vacuum port of the chamber (Figure 2.4). For these entire experiments, chamber was equipped with a borosilicate glass viewport which lets the laser beam pass inside and isolate the chamber from air environment. After the laser energies adjusted to the desired parameter, a mechanical shutter (Thorlabs) was used in order to set the timing for the structuring processes for different pulse numbers. As an example, shutter timer was set to 3.5 s for 35 pulse numbers at 10 Hz repetition rate. For each laser parameter, translation stage was moved 150 μm in x-y direction respectively.

For the calculation of new laser parameter for the new optical setup, one microlens can be considered as a laser beam which is masked with the size of microlens and then focused with a singlet lens to the focal point. Based on these points, the intensity of the light on the substrate generated with one microlens on the lens array was calculated as:

$$P_1 = Z\ mW$$

$$\frac{Z}{\pi r_1^2} = \frac{P_2}{\pi r_2^2} \tag{22}$$

where Z, P_1, P_2, r_1 and r_2 are the necessary laser power, laser output power, reduced output power at microlens diameter, radius of laser beam and radius of reduced output beam at microlens diameter respectively. Here r_1 is 4500 μm and r_2 is ≈ 75 μm. When values are inserted in Equation 22, reduced laser power can be calculated as:

$$P_2 = \left(\frac{75}{4500}\right)^2 Z = 2{,}778 * 10^{-4}\ Z \tag{23}$$

If the intensity is the ratio of the power at the focus area then the intensity of light focused with single microlens "*I*" will be:

$$I = \frac{P_2}{\pi r_3^2} = \frac{2{,}778*10^{-4}\ Z}{\pi 12{,}5\mu m^2} = 3{,}395 * 10^{-5}\ Z \tag{24}$$

Here r_3 was taken as 12.5 μm due to the measured radius of laser treatment on NW substrate and this intensity value is the fixed value for the NW substrate treatment. All these calculations are illustrated in Figure 2.5. First power adjustment for microlens treatment was done on NW substrates due to their low thickness (~750 nm) where they can be totally removed with the laser pulse and defined as 75 mW. Thus, power and crater diameter determination was defined over NW substrates. After the calculation of the enough intensity in order to get the optimum parameter on NW substrates, it is necessary to calculate the same intensity with a single lens which has 69 mm of focal length. Important point in here is to get the same focal spot size. This can be calculated by using a simple spot size calculation formula (Newport Corp. 2012a):

$$2\omega_0 = 2r_3 = \frac{4\lambda F}{\pi D} \tag{25}$$

As it can be seen from Equation 25, the most important parameters for the spot size (ω_0) calculation in our case are the focal length "*F*" and the incoming laser beam diameter "*D*". Thus, in order to keep the spot sizes same or close for microlens array structuring and singlet lens structuring, F/D ratio for both setups must be same or close to each other. Therefore the new laser output beam diameter must be calculated for 69 mm focal length lens.

$$\frac{F_1}{D_1} = \frac{F_2}{D_2} \rightarrow \frac{6{,}7mm}{\simeq 150\mu m} = \frac{69mm}{D_2} \rightarrow D_2 \simeq 1{,}5mm$$

In order to provide this size of laser beam, a mechanical iris diaphragm had been installed before focusing optic. Opening of the iris had been roughly set to 1.5 mm. This reduction also decreases the laser beam power and the new main laser output power must be calculated again with the new power. The important point in here the power P_2 must be same for any beam sizes after iris diaphragm reduction in order to provide the same intensity which was calculated at Equation 24. Therefore we can consider the P_2 is in use with 1.5 mm diameter reduced laser beam and we can calculate the necessary output power as Equation 26.

$$\frac{P_2}{r_{2,2}} = \frac{P_{1,1}}{r_1} \rightarrow \frac{2,778*10^{-4}\,Z}{\pi\,750\mu m^2} = \frac{P_{1,1}}{\pi\,4500\mu m^2} \rightarrow P_{1,1} = 9,992 * 10^{-3}\,Z \tag{26}$$
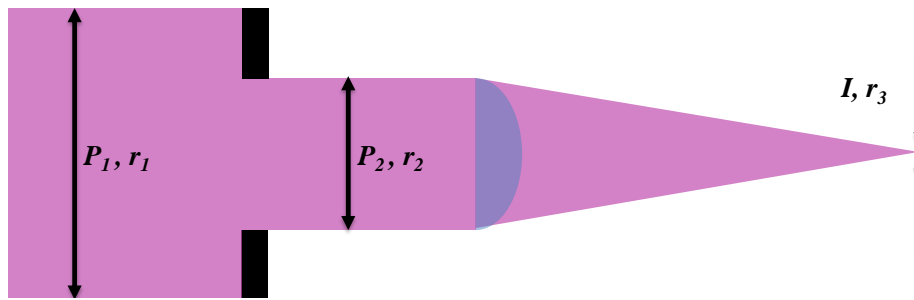
Figure 2.5: Schematic illustration for calculation of focusing with single microlens. It is possible to consider the setup like a blocked laser light with the same size of microlens and then focused with a singlet lens to the focal point.

Table 2.4: Re-Calculated powers for the structuring experiments of PEEK and alumina substrates and their energy conversion for 10 Hz.

Defined Microlens Array Output Power (mW)	Re-Calculated Singlet Lens Output Power (mW)	Energy Conversion of Re-Calculated Power (mJ)
75	~13	~1.3
125	22	2.2
250	45	4.5
500	~89	~8.9
750	133	13.3

However, when we insert the minimum necessary power which was defined before as 75 mW (this is the output power of the 7.5 mJ at 10 Hz repetition rate) in Z, the calculated value of $P_{1,1}$ will be 0,749 mW. This value is well below the measuring range of the power meter head that in used for experiments. Therefore, the $P_{1,1}$ value was accepted as a filtered value of direct laser output power and in order to provide such a high filtering, one ND filter was inserted in to the

optical path before reducing iris diaphragm. The filtering value of the ND filter was measured as 5.64% via several power measurements of high power laser output before and after filtering. Thus, after the re-calculation of $P_{1,1}$ value before filtering, the new value of direct laser output power (P^*) will be as Equation 27. Depend on these calculations, the new defined powers and their energy conversions are given in Table 2.4.

$$P^* = \frac{100*P_{1,1}}{5,64} = 0,17733\ P_1 \tag{27}$$

Table 2.5: Laser Microlens and Plasma Treatment parameters for substrate preparation.

Material	Al/Al$_2$O$_3$ NWs	Alumina Plate	PEEK
Treatment Type	Microlens Surface Treatment		
Parameters	7.5 mJ/pulse, 1 Pulse	250 mJ/pulse, 15 Pulses	7.5 mJ/pulse, 1 Pulse
Environment	Air		

2.2.3.2 Microlens Surface Structuring

As it given in Figure 2.4 schematically, microlens array setup was used to perform periodic surface structures on PEEK surface types, alumina plates and Al/Al$_2$O$_3$ core/shell NWs. Microlens array was fixed one focal length far from the substrate surface and the defined laser parameters from section 2.2.3.1 were applied to the alumina plate surface. Defined parameters are given in Table 2.5 and applied to the planar, plasma treated PEEK additional to the prepared Al/Al$_2$O$_3$ core/shell NWs and alumina plates.

2.2.4 Pulsed Laser Deposition

2.2.4.1 Designing of PLD System

Deposition of alumina by PLD was examined in order to define the optimum process parameters for the ideal coating which will be introduced to the previously realized micro and nano PEEK structures. In order to understand the relation between the thickness of the deposited layers and deposition time, laser pulse energy and number of the laser beams (single beam and double beam) were investigated. Additional to these parameters, multiple laser beam

investigation (which is designed, investigated and defined in this thesis for the first time with name "Matrix Shaped Pulsed Laser Deposition (MS-PLD)") was carried out to get the optimum homogenous coating distribution over the substrate surface (Akkan et al. 2013b). In this content, "Pulse Laser Deposition System" was designed and realized in the laser laboratory of CVD Group at INM-Leibniz Institute for New Materials (INM) as shown schematically in Figure 1.10 and built system can be seen in Figure 2.6.
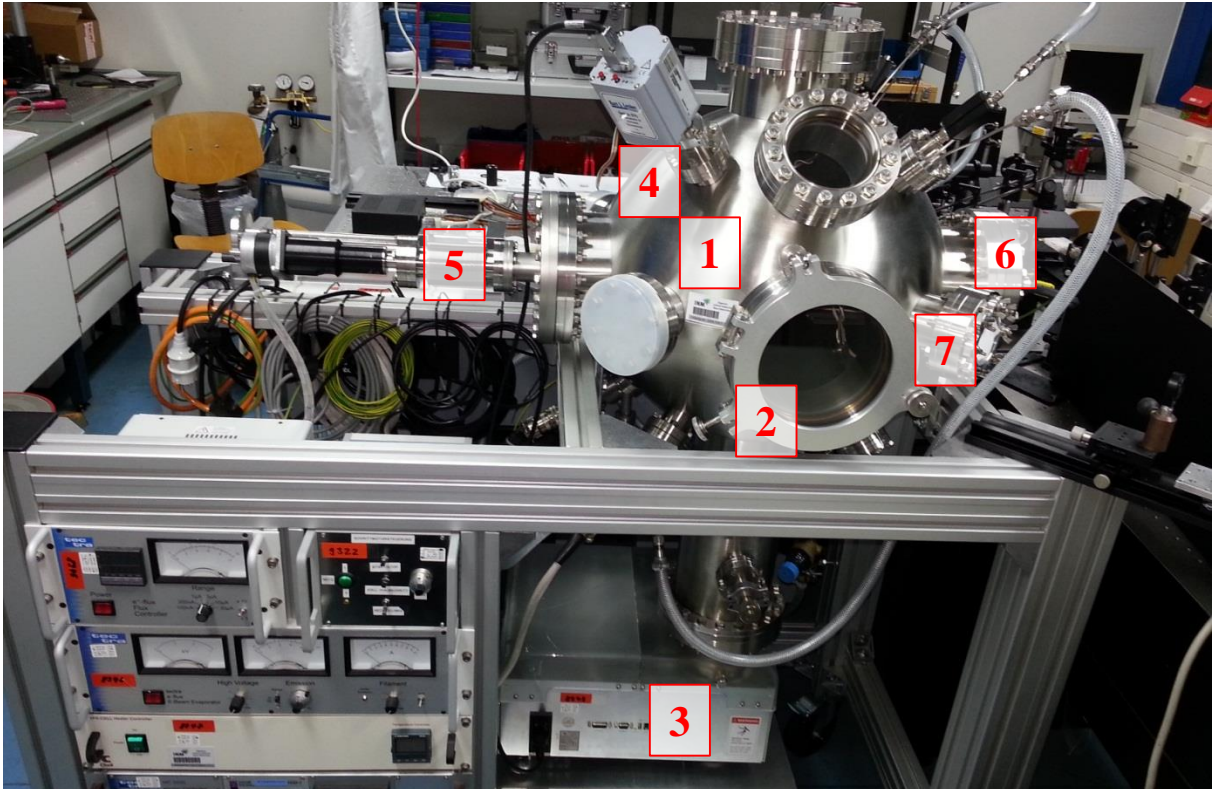
Figure 2.6: Complete PLD system: 1) Ultra-high vacuum chamber, 2) Quick Load element, 3) TPS pump system, 4) Vacuum Gauge, 5) Linear shift, 6) Heating plate sample holder, 7) Borosilicate laser viewport

PLD system consists of a spherical chamber (Kurt J. Lesker Company) which is suitable for ultra-high vacuum applications. For the easy installation of the substrates and the desired deposition target materials, a "quick load" element (Vacom GmbH, Germany) was installed on one of the 8" flanges of the chamber. Turbo Pump System (TPS-Compact, Agilent Technologies) was installed to the vacuum chamber in order to reach the desired vacuum level quickly and the system supported with a wide range vacuum gauge (Kurt J. Lesker Company, KJLC 979 Series) to monitor and follow the vacuum pressure of the chamber. This gauge can measure the pressure down to $6.7*10^{-10}$ mbar. A rotation stage (LewVac Components Ltd., United Kingdom) was installed to protect the deposition target from the drilling effect in

combination with single axis linear shift (Kurt J. Lesker Company) which is used to locate the target to the necessary distance from the substrate under vacuum condition. For the substrate holding, a "self-built substrate holder" was designed and produced from polycarbonate material and placed over a vertically installed boralectric heating plate (Tectra GmbH, Germany) which can be used to heat up substrates with suitable substrate holder up to 2000K. However the PLD system was designed to work with two UV-Fused Silica viewports, due to the getting coated by the time with several materials, they replaced with borosilicate glasses (Edmund Optics) and they are installed over a "replaceable viewport flanges" for the easy installation which was designed and realized in the workshop of INM. As laser source, third Harmonic of Nd:YAG laser (355 nm) was selected.
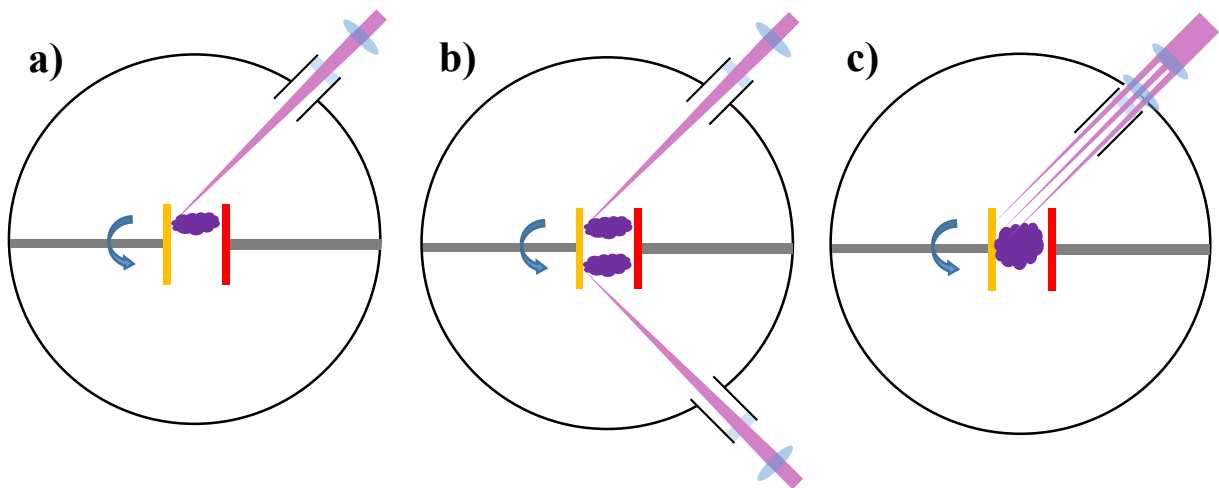
Figure 2.7: Optical setups for three different deposition systems: a) Single (1) Beam, b) Double (2) Beam and c) Matrix Shaped PLD.

2.2.4.2 Optical Setup for PLD System

As mentioned above, in order to get the optimum deposition homogeneity three different optical setups were designed which are single beam, double beam and Matrix Shaping (MS-PLD) (Figure 2.7). Laser parameters for these setups are given in Table 2.6. Titanium target was used for the definition of deposition homogeneity rather than alumina target because of its optical visibility in the visible range of electromagnetic spectrum even if with thin layers. Target materials were supplied from Kurt J. Lesker Company and their purities are for %99.99 for α-alumina and %99.2-%99.7 for titanium. Distance between the target and substrate was fixed around 8 cm.

Table 2. 6: Laser parameters had been used in PLD with three different optical setups.

Material	Ti			Alumina		
Optical Setup	1 Beam	2 Beam	M-Shaped	2 Beam		
Deposition Time (min)	10			10		20
Laser Pulse Energy (mJ)	100			35	60	100

For single beam deposition, laser output was divided in to two non-equal energy beams with a beam splitter (R: 5%, T: 95%) and the transmitted part of the beam was directed towards to vacuum chamber through two mirror periscope setup and incoming beam was focused to the Ti target surface with a 500 mm focal length lens from outside of the viewport (Figure 2.7-a). Reflected part (5%) from the beam splitter was used to monitor the laser energy in use. Focusing lens was fixed over optical cage rods and these rods were fixed to the vacuum chamber. Advantage of such a setup is to eliminate any possible shifting in distance and location. For the double beam deposition setup, laser output was divided into two beams with a high energy beam splitter (R: 48%, T: 52) before the previously mentioned beam splitter and these beams were directed to the vacuum chamber with the same method as explained in single beam setup and focused over the Ti target. Focused beams are perpendicular to each other (Figure 2.7-b).

Focusing a collimated light is depending to the wavelength of the light source and to the radius of curvature (ROC) of the focusing lens. Focal length can be calculated simply with equation 28.

$$\frac{1}{F} = (n-1)\left(\frac{1}{R_1} - \frac{1}{R_2} + \frac{(n-1)t_c}{nR_1R_2}\right) \tag{28}$$

Here n is the refractive index of the lens for the specified wavelength, t_c is the central thickness of the lens, R_1 and R_2 are the radiuses of curvatures of first and second surfaces of the lens, respectively (Newport Corp. 2013). In order to find the focal point of the lens over the Ti target, laser energy was set to its possible lowest energy and path was followed with a piece of paper. Lens traveled over the cage rods forward and backward until the sharpest point was observed. Real time photos of single beam PLD application can be seen in Figure 2.8.
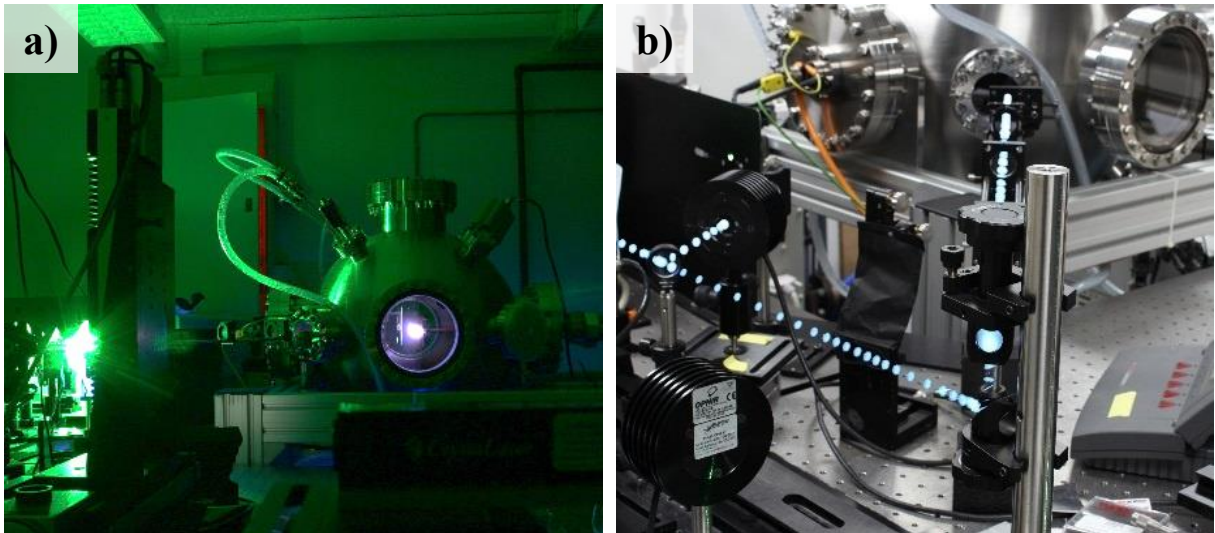
Figure 2.8: Real time photos of PLD application with long exposure time a) PLD system with laser output. Green light is the second harmonic of Nd:YAG laser where third harmonic is generated from, b) Single Beam Deposition Setup: blue round lights are the fluorescence effect of third harmonic on a piece of paper.

MS-PLD setup was built on the same optical path with single beam setup and to realize this optical system (Figure 2.7-c), microlens array which was mentioned in section 2.2.3.2 was used. Corresponding characteristics of the microlens array are given in Table 2.7. This optical setup is based on laser beam homogenization system (Suss Microoptics, Switzerland) which is produced by using a microlens array in combination with a focusing lens. Schematic illustration of the homogenizer setup is given in Figure 2.9-a. In such an optical setup, microlens array acts like a beam splitter and splits the incoming laser beam into beamlets. The second lens which is called "Fourier Lens" transforms the diverging beams into parallel bundles. Each bundle interferes again with the others at the image plane (target surface) where the back focal point of the fourier lens is found (Figure 2.9-b) (Voelkel et al. 2008; SÜSS MicroTec AG 2012).

Table 2.7: Properties of Microlens Array which had been used in this thesis.

Material	UV-Fused Silica
Focal Length (mm)	6.7
Period of Lenses (μm)	150
Diameter of Single Lens (μm)	146
Thickness of Array (mm)	1.2
ROC (mm)	3.036
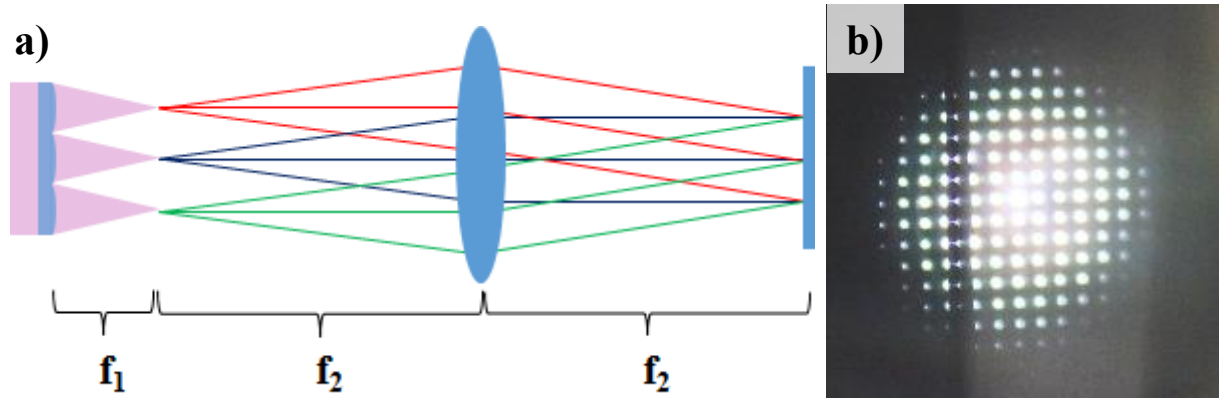
Figure 2.9: a) Schematic illustration of laser beam homogenizer optical setup in order to produce periodic patterns over surfaces. f_1 and f_2 are the focal lengths of the microlens and focusing lens respectively. b) Periodic diffraction patterns over target material to sputter from many points which can simulate tens of laser beams in focus towards to the target.. (Voelkel et al. 2008; SÜSS MicroTec AG 2012)

Characteristics of the lens array and focal length of the fourier lens have importance for the determination of the effective area at the image plane, distances between the periodic diffraction patterns and their homogeneities. They can be calculated easily as given below:

Generated effective area "E_a" can be calculated as:

$$E_a = \left| \frac{D_{ML} \times f_{FL}}{f_{ML}} \right| \tag{29}$$

Here D_{ML} is the diameter of a single microlens, f_{FL} and f_{ML} are the focal lengths of the fourier lens and single microlens respectively. Periods of the generated diffraction patterns "P" are given as:

$$P = \frac{f_{FL} \times \lambda}{D_{ML}} \tag{30}$$

Here λ is the wavelength of the laser beam as usual (SÜSS MicroTec AG 2012).

As it mentioned above, 500 mm focal length lens and microlens array with 6.7 mm focal length was used to design this optical setup. Necessary values can be calculated easily when the current data for these lenses are inserted into these equations. Calculated results are given in Table 2.8 additional to the results of fourier lenses with shorter focal lengths. As can be seen from there effective area is increasing when the focal length of the fourier lens increases. It is also right to say the same for the periods of the diffraction patterns. Additionally, effective area with generated diffraction patterns will have the same geometric shape with the microlens array. In

this case, the generated shape is circular because of the circular aperture of each microlens. This effect can be seen in Figure 2.9-b. Additionally, effective area is limited with the first five diffraction patterns in x- and y- directions from the center. As usual, central pattern has the highest intensity and further patterns are losing their intensities slightly but this effect decreased at the future experiments by moving the microlens array from its regular position. On the other hand, there are some more diffraction patterns out of the mentioned range as can be seen in Figure 2.9-b but they can be ignored due their too low intensities (Voelkel et al. 2008)

Table 2.8: Calculated radius of effective area and the distance between generated periodic diffraction patterns.

Fourier Lens Focal length (mm)	E_a (mm)	P (mm)
500	11.657	1.183
400	9.326	0.947
300	6.994	0.710
200	4.663	0.473
150	3.497	0.355

2.2.4.3 Deposition of Titanium for the Homogeneity Determination

Ti material was deposited over glass substrates rather than alumina by using three different techniques in order to understand the thickness distribution of the deposited layers which is called in this thesis as homogeneity. As given in Table 2.6, 100 mJ laser beam energy (for each incoming beam) was applied to the Ti target under 10^{-6} mbar pressure. Captured real-time photos of the deposition processes are given in Figure 2.10.
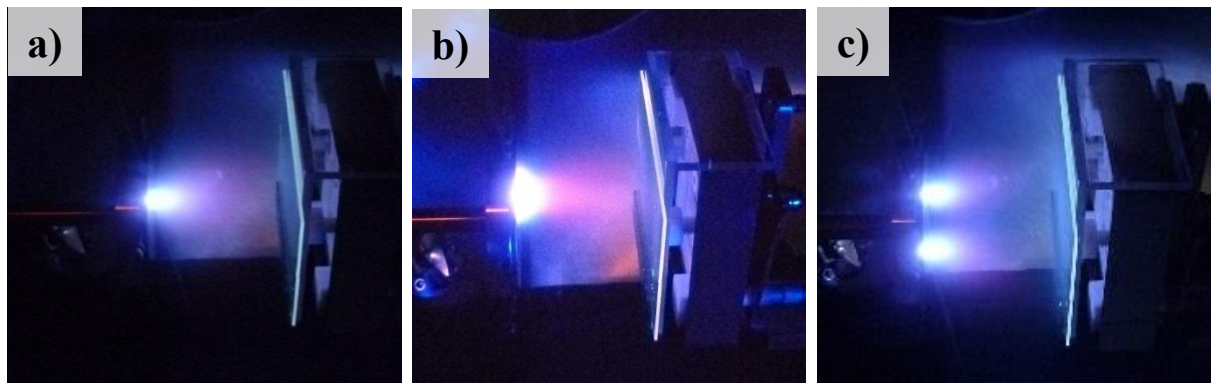
Figure 2.10: Three different setups of PLD for homogeneity determination via deposition Ti on glass substrates. a) Single beam PLD, b) MS-PLD and c) Double beam PLD.

2.2.4.4 Deposition of Alumina on Prepared Glass and Silicon Wafer Substrates

Double beam deposition technique was applied to alumina target for 10 and 20 minutes with three different laser energies of 35 mJ, 60 mJ and 100 mJ per pulse and per beam under fixed vacuum pressure of 10^{-6} mbar. The distance between the focal spots was fixed to 15 mm similar to that used for titanium deposition. Deposition of alumina over glass and silicon wafer substrates at 100mJ beam energy can be seen in Figure 2.11.
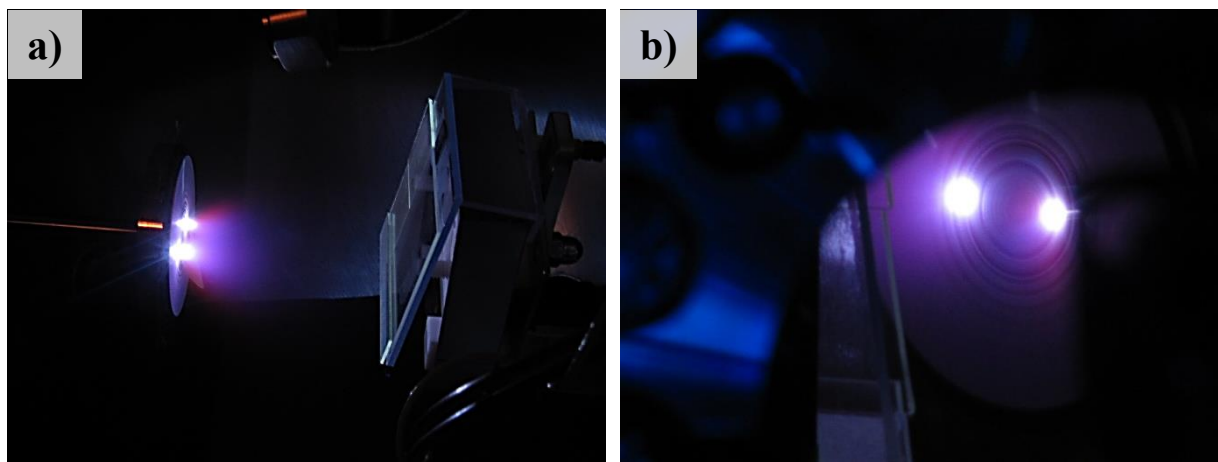
Figure 2.11: Double beam deposition of alumina over the glass and silicon wafer substrates.

2.3 Cell Tests

2.3.1 Sterilization of Samples

Two types of sterilization methods were applied to treat the prepared substrates. For alumina substrates dry heat technique was used. Substrates were placed in a closed glass Petri dish and covered with aluminum foil. Prepared dishes were placed in an oven for 3 h at a temperature of 180°C. For alumina coated PEEK substrates autoclave (vapor heat) technique was selected and applied. Substrates were put in a special container and then placed in the autoclave which sterilizes the substrates around 120°C temperature of under 1 bar pressure. Cycle timing for autoclave sterilization is 20 min.

2.3.2 Cell culturing

Human umbilical vein endothelial cells (HUVEC; Invitrogen, Germany) were used in these experiments in order to see the effects of prepared surfaces on cells. HUVEC were cultured under 5.0% CO_2 in LSGS (Low Serum Growth Supplement; Invitrogen) supplemented Medium 200 (Invitrogen). After getting the optimal confluence (~80%), cells were trypsinated and seeded over previously sterilized substrates with a density of 250 cells per mm^2. Seeded cells were incubated for 1, 3 and 6 days. For all experiments 24 well plate (Greiner) was used.

2.3.3 Immunocytochemical staining

Since the PEEK surfaces are known as auto-fluorescent, only alumina samples were stained (Althaus et al. 2012). For the visualization of the cytoskeleton, F-actin fibers of the cells were stained using fluorescence label Phalloidin (Alexa Fluor 555 label; Invitrogen). As well as for the focal points observation, Vinculin was stained using mouse anti-human primary antibody (Invitrogen) and Alexa Fluor 488 anti-mouse secondary antibody. Therefore, medium was discarded and the cells were fixed with 4% of PFA (paraformaldehyde; Sigma-Aldrich, Deisenheim, Germany) for 10 min. Following the previous step, cells were permeabilized by

using 0.1 % Triton X-100 solution (Carl Roth, Karlsruhe, Germany) for 5min. After blocking with 1 % BSA solution (Carl Roth) for 30min each substrate was mounted with 75 µl Vinculin primary antibody which is diluted as 1:1000 in PBS (Phosphate buffered saline) solution and continuously incubated for 1h in a dark humid environment at RT (room temperature). Then primary antibody solution was discarded and samples were washed three times with PBS. Following the washing step, 75 µl of staining master solution was mounted over each substrate for 25 min in a dark humid environment at RT. The master staining solution is formed from 1:200 secondary Alexa Fluor 488 antibody in PBS mixed with Phalloidin (0.45 U). Following the incubation process, substrates were washed three times for 5min with PBS and finally rinsed with distilled water to remove any crystals accumulation. After letting them dry under air condition each sample was embedded in 10 µl ProLong® Gold antifade reagent including DAPI (Invitrogen). Finally substrates were placed in a dark room at RT for 24 h. To avoid accumulation of air bubbles between the substrates and the coverslips, their around were sealed with finger nails and stored in a 5°C fresh environment The microscopy analysis had been performed using Keyence BZ 9000 fluorescence microscope. The specificity of the primary antibody was always controlled in every experimental via set using a normal cover slip as control.

2.3.4   Determination of Metabolic activity (WST-1 assay)

Metabolic activities of the HUVEC's were determined by WST-1 assay (Cell Proliferation Reagent; Roche Diagnostics, Mannheim, Germany) which is based on the absorption measurement of formazan formation. Cells were incubated on different surface structures and incubated up to 3 days at 37°C. The determination of cell metabolic activity was carried out after addition of WST-1 reagent and the formazan formation was measured as described in the manufacturer's instruction manual (F. Hoffmann La-Roche 2005). The mean absorbance of cells from the positive control was defined as 100%, and the absorbance of the treated cells was related to this value. First day results from the glass and non-treated PEEK substrates were used as positive control for alumina and alumina coated PEEK surfaces respectively.

2.4 Measurements Methods and Techniques

2.4.1 Whitelight Interferometry

Depth measurements of laser treated PEEK and alumina plates were performed by using whitelight interferometer (NewView™ 7000 Series, Middlefield, CT, USA) which gives 3D images of the structures with high accuracy in z axis scanning (<0.1nm). Additional to 3D images, roughness measurements of alumina deposition were performed with the same device.

2.4.2 Atomic Force Microscopy (AFM)

Roughness measurements of the alumina coated PEEK substrates additional with the Al/Al_2O_3 core/shell nanowires and alumina plates (before and after laser treatement) were performed with AFM (NanoWizard 3 by JPK Instruments AG) at different scan ranges depending on the substrate and the structure size.

2.4.3 Scanning Electron Microscopy (SEM) and Energy Dispersive X-Ray Spectroscopy (EDS)

SEM images were taken by the FEI-ESEM-Quanta 400-FEG and EDS measurements of the alumina deposition by PLD were performed by a combined device from company EDAX.

2.4.4 X-Ray Photoelectron Spectroscopy (XPS)

XPS measurements of the deposited alumina layers on PEEK substrates were performed by the device of Omicron Nanotechnology Full Lab, at ultra-high vacuum conditions (around 10^{-9} mbar). Al-Anode (1486.6eV) was used as X-Ray source and the angle between the X-ray source and the analyzer was fixed to 54.7°.

2.4.5 Contact Angle Measurements

Static contact angles of the prepared surfaces were measured and surface energies were calculated with Equation 18. Measurements were done with a video contact angle system (Krüss GmbH, Hamburg, Germany) for the 1st, 3rd and the 6th days in addition to the treatment day (Day 0). Samples were placed on a flat substrate table which can move in three directions as desired. During the contact angle measurements ultra-pure water was used

2.4.6 Determination of the Coating Distribution of PLD layers

Homogeneities of the deposited layers were tested with a self-built optical measurement device (Figure 2.12). In this optical setup, He-Ne laser (632 nm) which has 1 mm diameter was used as the light source. Due to its small output beam size, laser beam was expanded ten times before it get focused on the coated side of the substrates. Expanded laser beam was focused as a line with a cylindrical lens; which has 150 mm focal length, to the top edge of the glass substrate where the deposited side faced to the laser source after masking with 5 mm×5 mm square mask. Some partial of the laser light was transmitted depending on the Beer-Lambert law and re-collimated with another cylindrical lens. After the re-collimation, transmitted light was focused with a spherical lens into a fiber optic cable and transferred to the UV/VIS spectrometer (Baki Spectrometer, Beam Arge/Turkey). Transmitted intensities from the depositions were collected by scanning the substrate in one direction at every 2.5 mm steps. Aim of the line focusing was to collect data from a narrow line with a 5 mm width in the opposite direction of the scanning in order to eliminate any uncertainty in measurement where the substrate may have some impurities inside. Collected intensities were listed with their location data and normalized to the highest intensity.
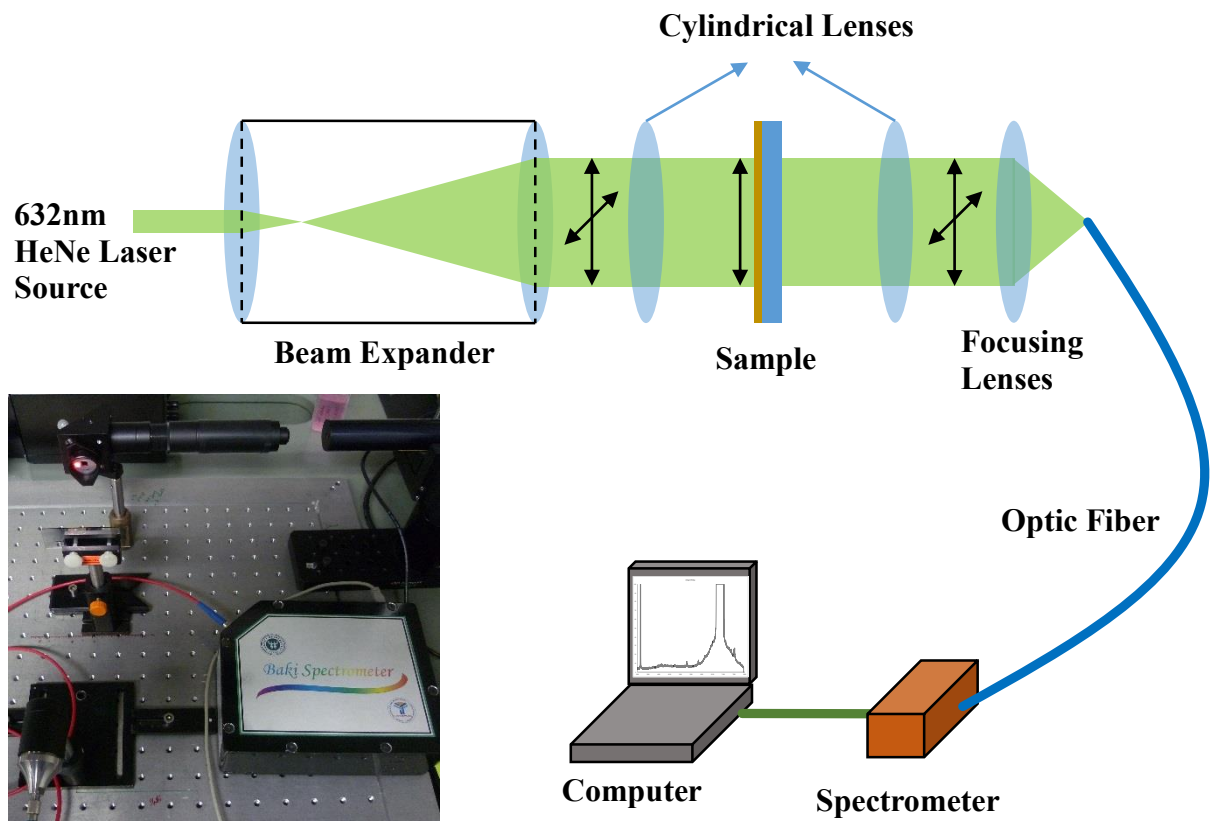
Figure 2.12: Optical setup for the homogeneity measurement of the Ti layers. Expended laser beam is focused in the form of a line to scan the substrate. Transmitted lights were collected with a spectrometer and measured intensities were normalized.

3   RESULTS

3.1   Plasma Surface Modification of PEEK (NW formation)

As it mentioned previously, O_2 plasma etching of PEEK produces nano/micro size polymer wires. Lengths of these wires are depending on the applied RF power and the O_2 gas amount inside the chamber. However, diameter of the fibers remains around 20 nm in diameter.
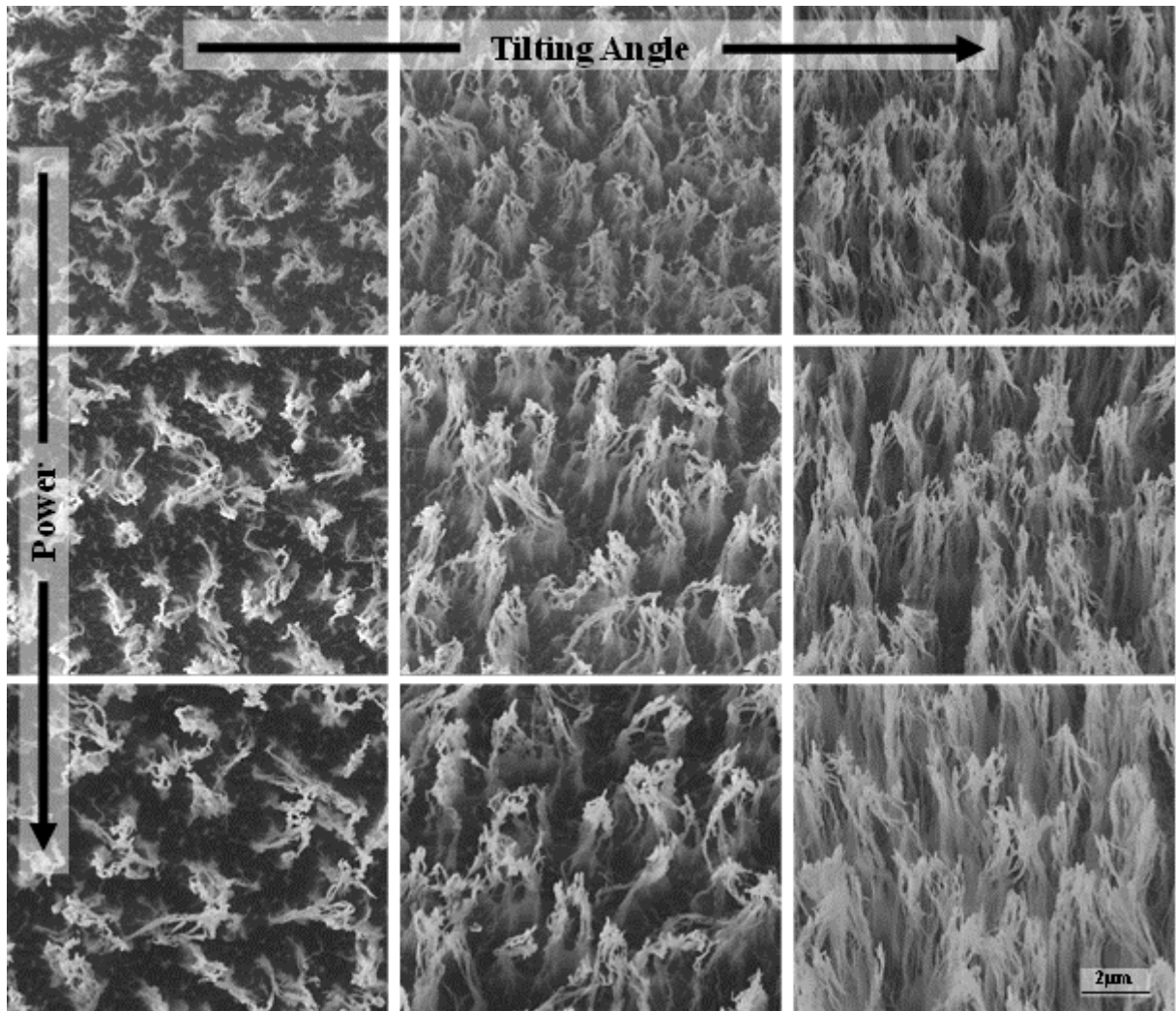
Figure 3.1: SEM micrographs of PEEK NWs at different tilting angles. Angles are changing as 0˚, 15˚, and 37˚ respectively from left to right on the combined images. Effects of the RF power on the wire length can be seen from low power to high power in comparison to the tilting angles. Applied RF powers 20W, 30W and 40W from top to down respectively.

3.1.1 Effect of RF Power Variation on Fiber Growth.

At the first plasma etching part, effects of RF power on the growth factor of PEEK NWs were investigated. Within this concept, three different RF powers were applied to the electrode which was given before. During the experiments, Ar gas; which was used for secondary cleaning of the substrate surface, was fixed to 25 sccm flow rate for 5 minutes of plasma cleaning and O_2 gas flow was fixed to the 250 sccm for the rest of the process which was totally 1 hour. Lengths of the PEEK NWs were measured by using the SEM images where the substrates were tilted with angles of 15° and 37°. Measured wire lengths were corrected depending on the tilting angles afterwards. Average values were calculated for each type of substrate. SEM images can be seen in Figure 3.1 for three different powers and at different tilting angles. All the images were taken with identical magnification and due this reason, it can be seen that when the RF power increases the length of the wires increase. It seems that there is a linear relation between the applied RF power and the wire length. This effect can be seen more clearly in Figure 3.2. Additionally, density of the produced fibers can be seen at incident angle in Figure 3.1 and they are practically same for all powers.
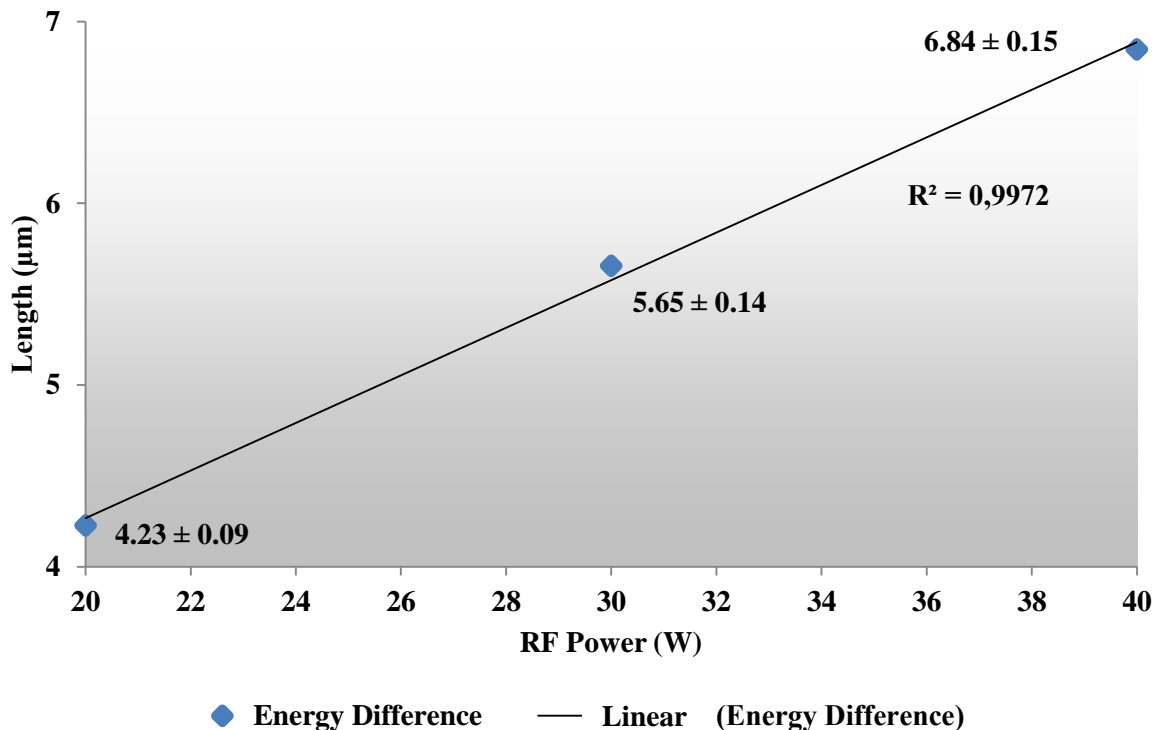
Figure 3.2: Graph of PEEK NW length versus applied RF power.

3.1.2   Effect of O_2 Etchant Gas Variation on Fiber Growth.

As second approach to understand of PEEK NW growth in their length, similar to the first approach, different amounts of O_2 etchant gas were investigated. Within this concept, three different gas flows were used under fixed RF electrode power which was 30W. Similar to the first approach, Ar gas flow was used for 5 minutes as secondary cleaning process and after that the process continued for rest 55 minutes with different O_2 gas flows. Lengths of the PEEK NWs were measured and average values were calculated for each kind of parameters. SEM images of the corresponding results can be seen in Figure 3.3. As can be seen from 37° tilted images of Figure 3.3 (down line) the wire length is increasing when the O_2 gas amount inside the chamber increase. Here the gas amounts are 100 sccm, 250 sccm and 400 sccm respectively. However, when the length/gas amount distribution were examined (Figure 3.4), it is not possible to say that the length increment is as linear as RF power distribution as previously observed. There is almost no difference between the 250 sccm and 400 sccm gas flows. However, due to the high value of the R^2 value, wire length increasing can be considered as linear with the increased oxygen amount.
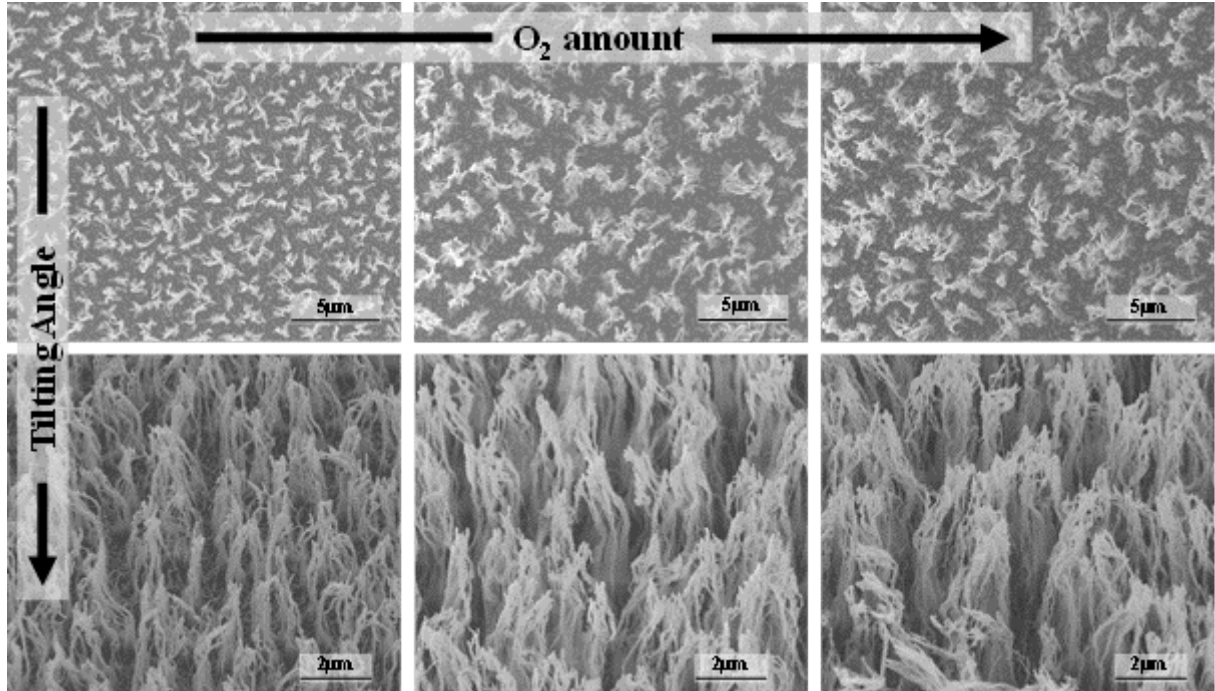
Figure 3.3: SEM micrographs of PEEK NWs at different tilting angles (0° and 37°). Effect of the O_2 etchant gas on wire length can be seen from left to right 100 sccm, 250 sccm and 400 sccm respectively.
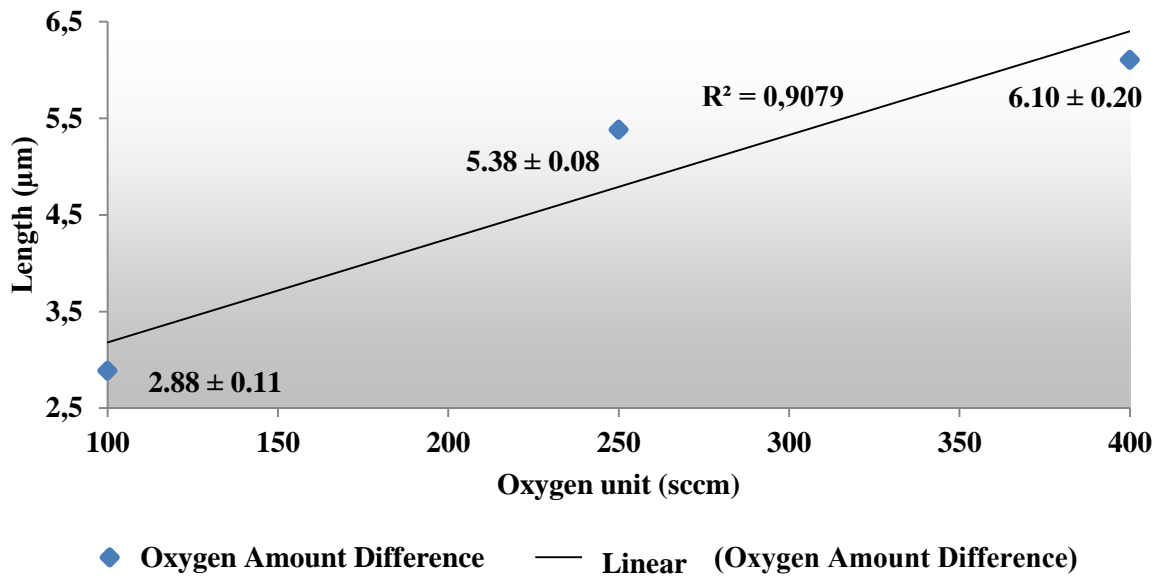
Figure 3.4: Graph of PEEK NW length versus oxygen gas flow inside the chamber.
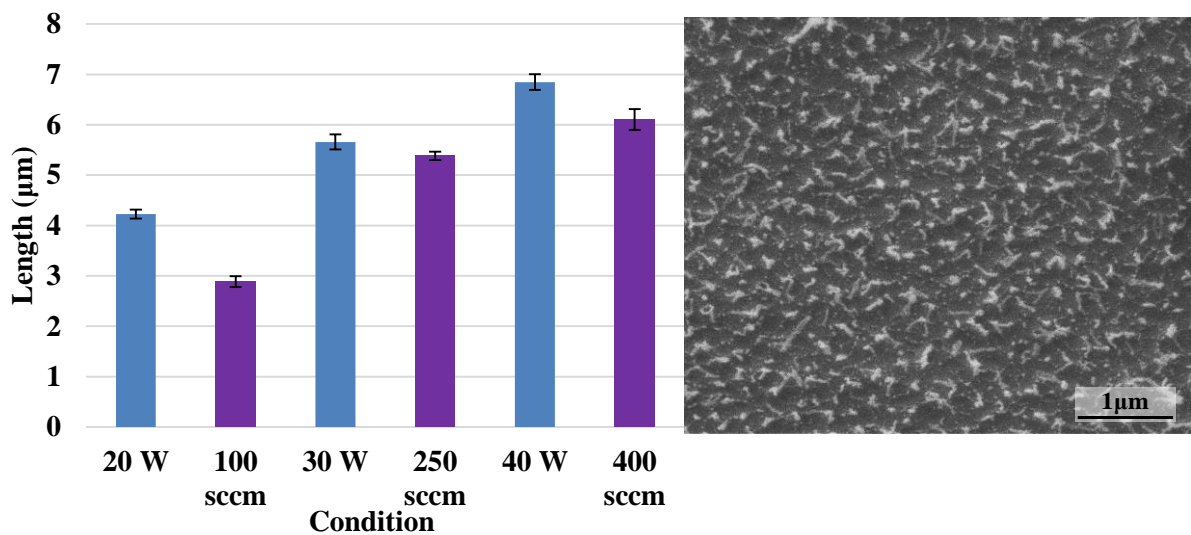
Figure 3.5: Summary of the NWs length depends on the experimental condition.

In order to choose the optimum length for the further cell test, all parameters were arranged and presented in Figure 3.5. From here, parameter which provides the shortest wire size was selected (100 sccm at 30 W RF power) and used to perform PEEK NWs where these structures considered as comparable surface type to the Al/Al$_2$O$_3$ core/shell NWs. Furthermore; to get shorter fibers, process time was shortened. However rather than short fibers, small island-like structures were observed. A SEM image of these structures is given in insert image of Figure 3.5.

3.2 Single Lens Laser Structuring of Alumina and PEEK Substrates

3.2.1 Laser Structuring of PEEK

As it explained in detail before, a new optical setup was performed for laser surface structuring studies which can be also named as a drilling or material removal study. In order to understand the laser material interaction for material removal from bulk, following experiments were realized. As can be seen in Figure 3.6-a, structure starts to appear when the focused laser beam strikes the substrate surface and this process forms a keyhole. Keyhole helps laser to heat up the surface more by increasing the light absorptivity of the material due to the reflections from rough area. When the laser beam moves in deeper, material vaporizes and molten parts flow out from the hole because of the generated high vapor pressure. If the laser pulse intensity is too high for the vaporization, as explained before in Part 1.1.2.4, a plasma plume occurs and this blocks a part of the laser energy. In that case, performed hole may not be in good quality (non-uniform). Additionally, local pressure from the plasma expansion helps for the material removal too.
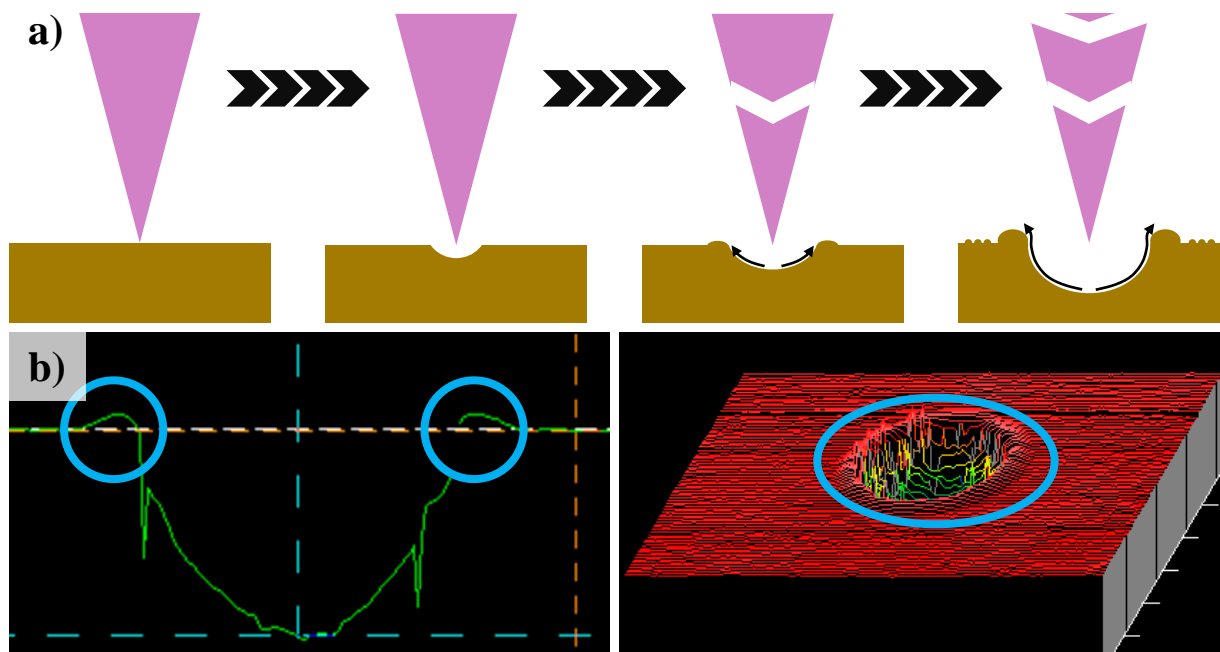
Figure 3.6: a) Schematic of pulse laser material ablation. After first pulse, melt forms and with the continues pulses the molten part eject via vapor and plasma pressure flow. This causes re-solidification at the hole entrance. b) Whitelight interferogram of PEEK substrate with several laser pulses. Re-solidified parts are highlighted with light blue circles.
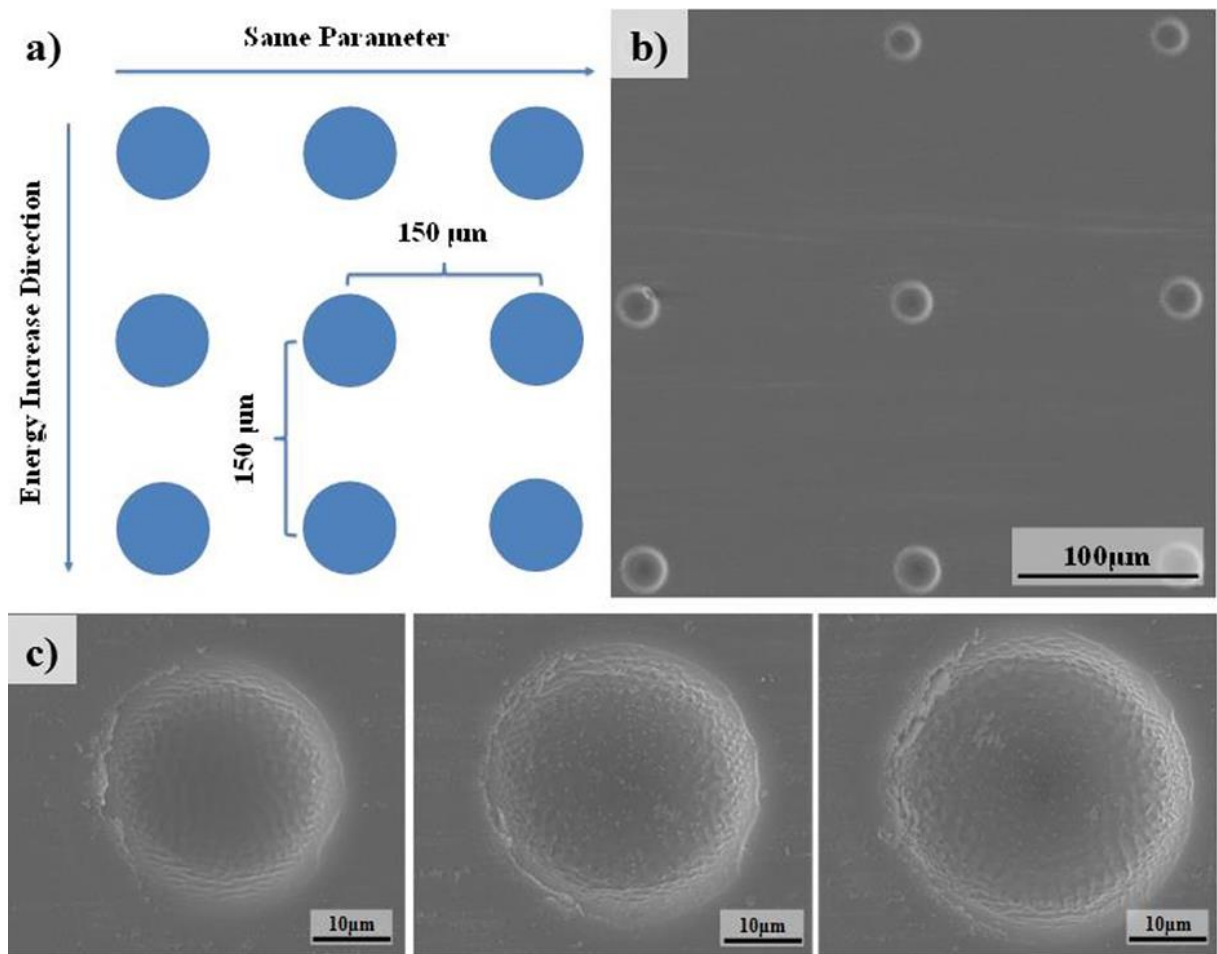
Figure 3.7: Schematic illustration of single lens experiment parameter variation and SEM pictures of PEEK substrate treatments a) Parameter changes in direction of x and y, b) SEM image of 20 pulses series in air environment c) Magnified SEM images of 20 pulses in air environment with energies from left to right 1.3mJ, 2.2 mJ, 4.5 mJ respectively. Crater diameter is increasing with energy increment.

Speed of the material removal from the hole is supersonic, thus, this causes shockwaves. Removed molten material usually splashes or re-solidifies at the surface around the hole (Schou J 2006). This can be seen in Figure 3.6-b at the whitelight interferometer image of the PEEK substrate.Three different energies and five different pulse numbers were applied in these experiments with the explained optical setup in Part 2.2.3.1 and mean value of each parameter was calculated. As illustrated in Figure 3.7-a, 150 μm spacing was left between each structure. From left to right, spots have the same specifications with each other and from top to down the laser energy was increased step by step as planned in order to understand the laser energy effect on the material removal. It can be seen clearly in Figure 3.7-c from left to right, the crater diameter is increasing with the increased energy. Energies applied from left to right in Figure 3.7-c (PEEK surface) are 1.3 mJ, 2.2 mJ, 4.5 mJ respectively. Each parameter was repeated for

70
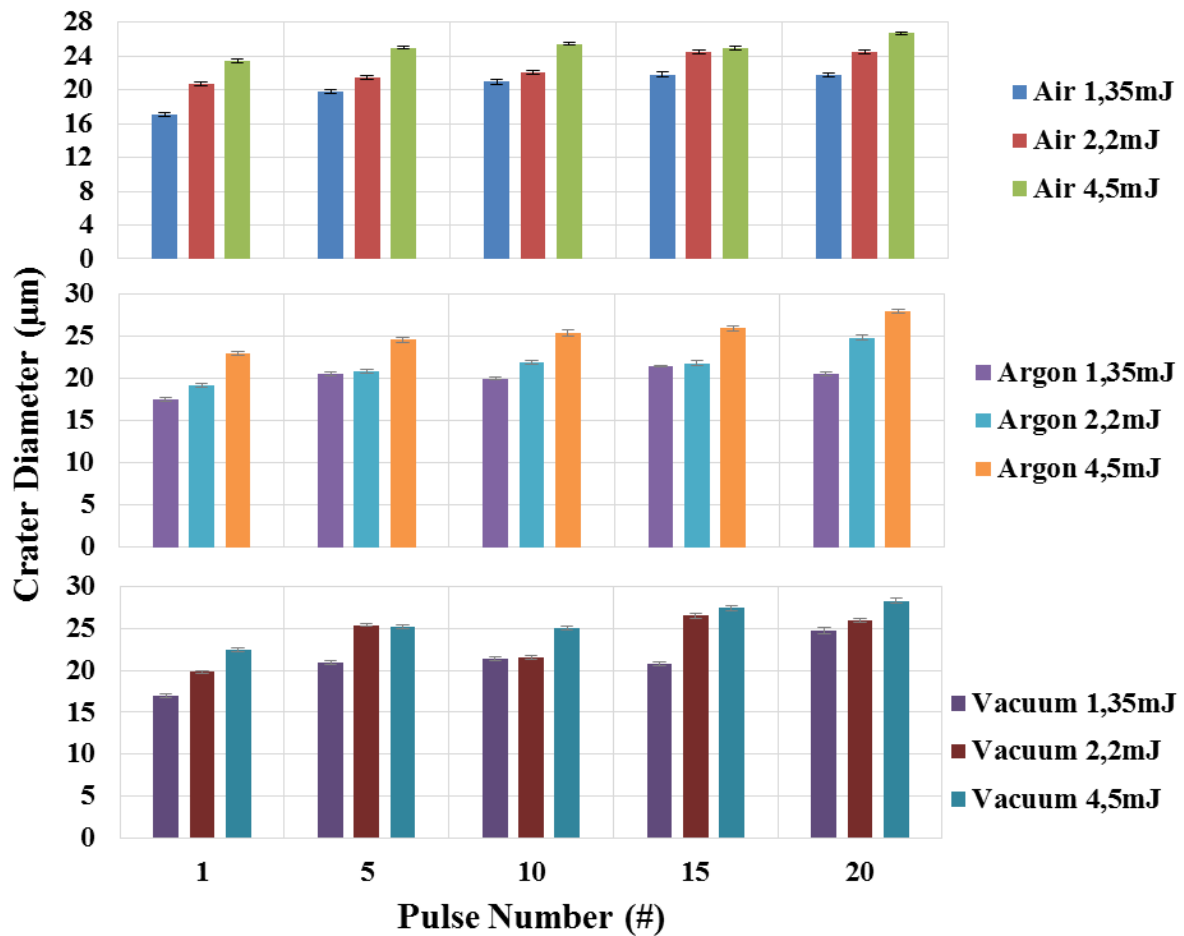
Figure 3.8: Crater Diameter distribution of PEEK substrate with different pulse numbers, different energies and at different environments. Increment can be seen clearly, however it is limited with few microns.

different environments of air, vacuum and argon gas flow. Crater diameter distributions for environmental, energy and pulse number conditions are given in Figure 3.8. It is clear that the crater diameters increase when the pulse number and the pulse energy increases. However, when the values were checked, it is indicating that the variations of diameters are limited with few microns. Mean values of the crater diameters depending on the conditions are given in Table 3.1-a.

Depth measurements were performed by whitelight interferometer. When plots were drawn with the mean depth values versus to pulse number (Figure 3.9), it can be clear seen that the depths are increasing linearly with the number of the pulses. However, some variations out of linearity can be seen. They may be the results of laser energy fluctuations during pulse repetition. Measured depth values are represented in Figure 3.9 and mean values of the depths are given in Table 3.1-b.

Table 3.1: a) Crater diameters and standard errors b) Crater depths and standard errors of PEEK in different environmental conditions and laser pulse numbers (units are in μm)

a)		1.35 mJ	2.2 mJ	4.5 mJ
Environment	#	Diameter (μm)		
Air	1	17.08 ± 0.25	20.66 ± 0.20	23.33 ± 0.23
	5	19.75 ± 0.24	21.47 ± 0.22	24.97 ± 0.19
	10	20.92 ± 0.30	22.08 ± 0.26	25.41 ± 0.18
	15	21.79 ± 0.27	24.45 ± 0.24	24.91 ± 0.17
	20	21.75 ± 0.26	24.45 ± 0.23	26.66 ± 0.17
Vacuum	1	16.95 ± 0.23	19.79 ± 0.12	22.50 ± 0.20
	5	20.95 ± 0.23	25.41 ± 0.15	25.16 ± 0.21
	10	21.37 ± 0.17	21.58 ± 0.22	25.00 ± 0.23
	15	20.75 ± 0.20	26.50 ± 0.25	27.41 ± 0.25
	20	24.66 ± 0.37	25.91 ± 0.26	28.29 ± 0.25
Argon	1	17.50 ± 0.24	19.16 ± 0.24	22.91 ± 0.23
	5	20.50 ± 0.21	20.83 ± 0.25	24.58 ± 0.26
	10	20.00 ± 0.14	21.93 ± 0.23	25.41 ± 0.41
	15	21.50 ± 0.09	21.79 ± 0.31	25.95 ± 0.35
	20	20.58 ± 0.21	24.83 ± 0.30	28.00 ± 0.28
b)		1.35 mJ	2.2 mJ	4.5 mJ
Environment	#	Depth (μm)		
Air	1	0.62 ± 0.01	0.78 ± 0.01	1.14 ± 0.02
	5	2.86 ± 0.05	3.86 ± 0.07	5.28 ± 0.10
	10	5.37 ± 0.10	7.00 ± 0.01	9.88 ± 0.01
	15	8.06 ± 0.02	10.56 ± 0.07	14.65 ± 0.08
	20	9.83 ± 0.06	13.17 ± 0.02	19.57 ± 0.07
Vacuum	1	0.59 ± 0.01	0.76 ± 0.01	1.08 ± 0.01
	5	2.45 ± 0.04	3.39 ± 0.08	4.89 ± 0.05
	10	4.61 ± 0.06	6.18 ± 0.04	8.98 ± 0.06
	15	5.88 ± 0.10	8.74 ± 0.03	11.85 ± 0.07
	20	7.85 ± 0.10	10.80 ± 0.09	15.12 ± 0.03
Argon	1	0.65 ± 0.01	0.79 ± 0.04	1.51 ± 0.02
	5	3.04 ± 0.05	3.42 ± 0.09	5.35 ± 0.04
	10	6.00 ± 0.03	7.12 ± 0.03	9.60 ± 0.03
	15	8.39 ± 0.07	10.09 ± 0.05	14.23 ± 0.03
	20	10.47 ± 0.02	12.13 ± 0.07	18.37 ± 0.05
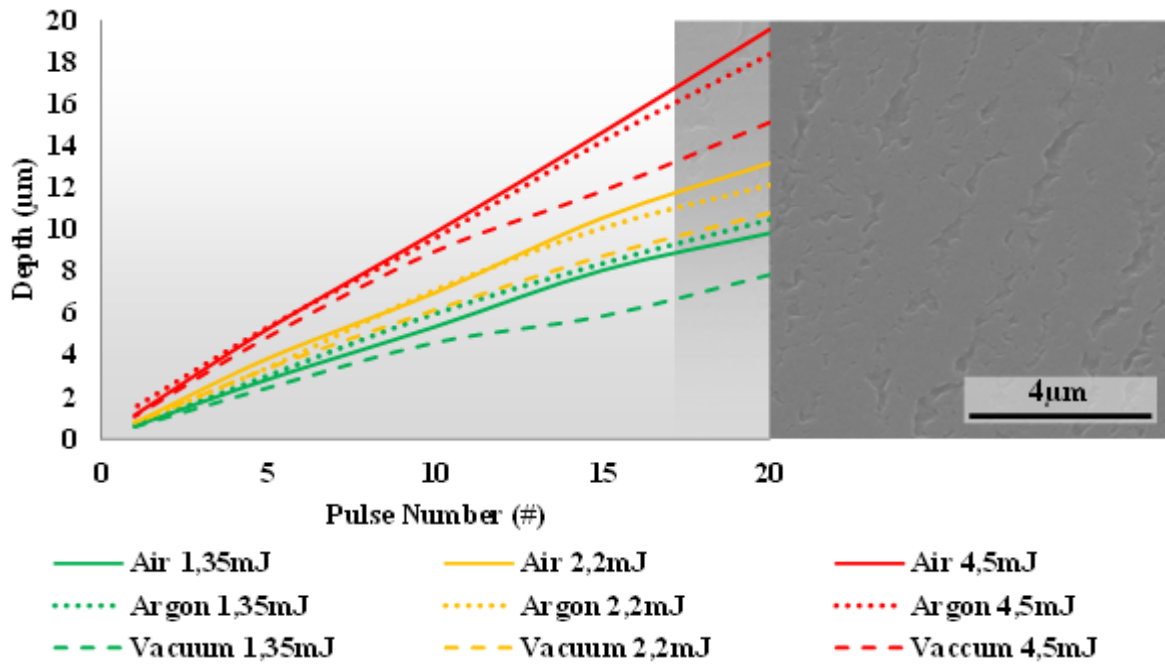
Figure 3.9: Depth of the laser treated structures at different energies and different environmental condition for PEEK substrate. Surface topography of non-treated PEEK substrate can be seen in inserted image.

Linear increasing of the structure depths indicates a certain ablation rate where the amount of the ablated material is almost the same for every single laser pulses. Therefore, the ablation rate versus to applied laser fluence was investigated. It was observed that the ablation rate shows linear increasing with the increased laser fluence. Additionally it was observed that the ablation rate is almost independent from the environment for PEEK substrate (Figure 3.10). Furthermore, depth distributions versus energy and pulse numbers are given in Figure 3.11. It can be clearly seen there the depths are increasing when the laser pulse energy increases.
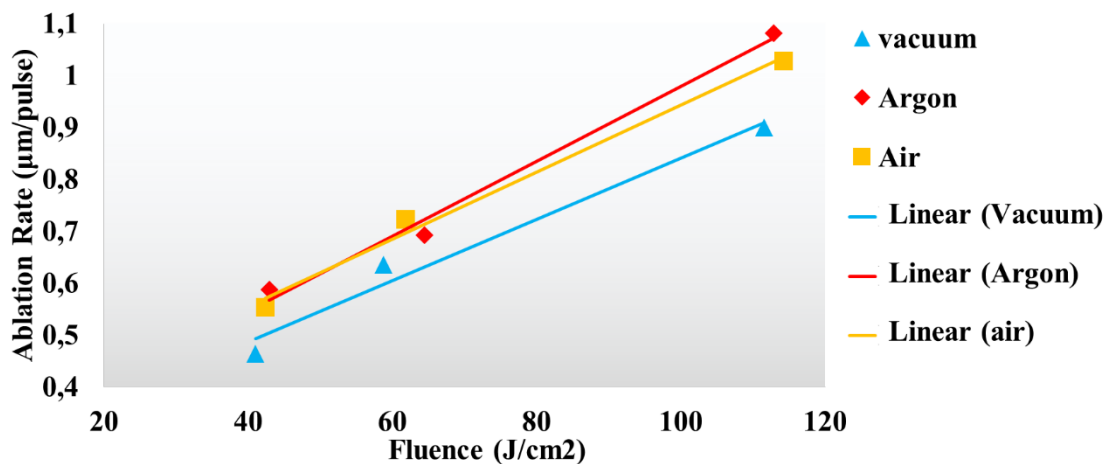
Figure 3.10: Laser material ablation rate versus to laser fluence. Having close ablation rates with linear increasing indicates that the material ablation rate is almost independent from the environment.
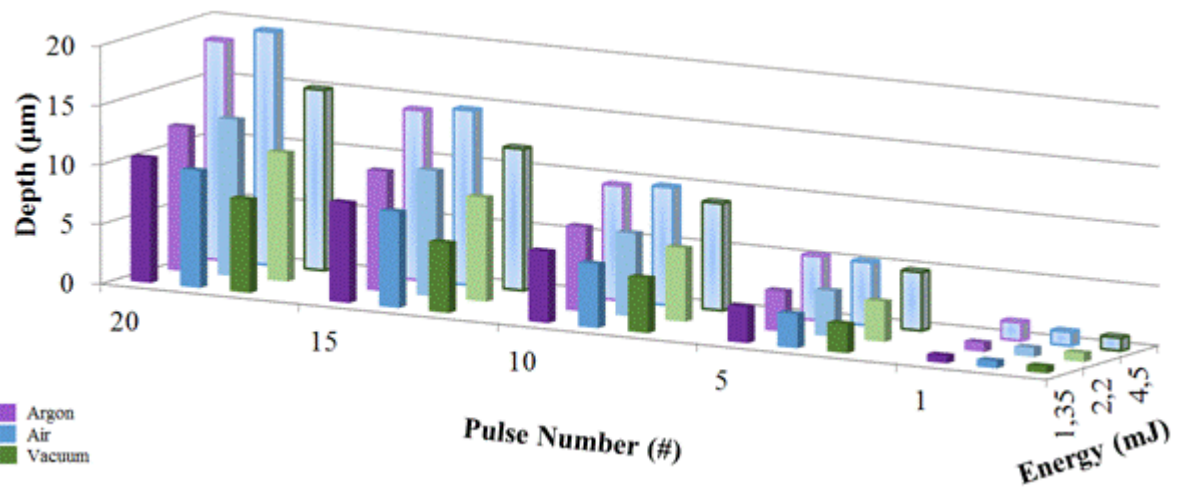
Figure 3.11:Summary of depth distribution at different energy, pulse number and atmospheric conditions for PEEK substrate.
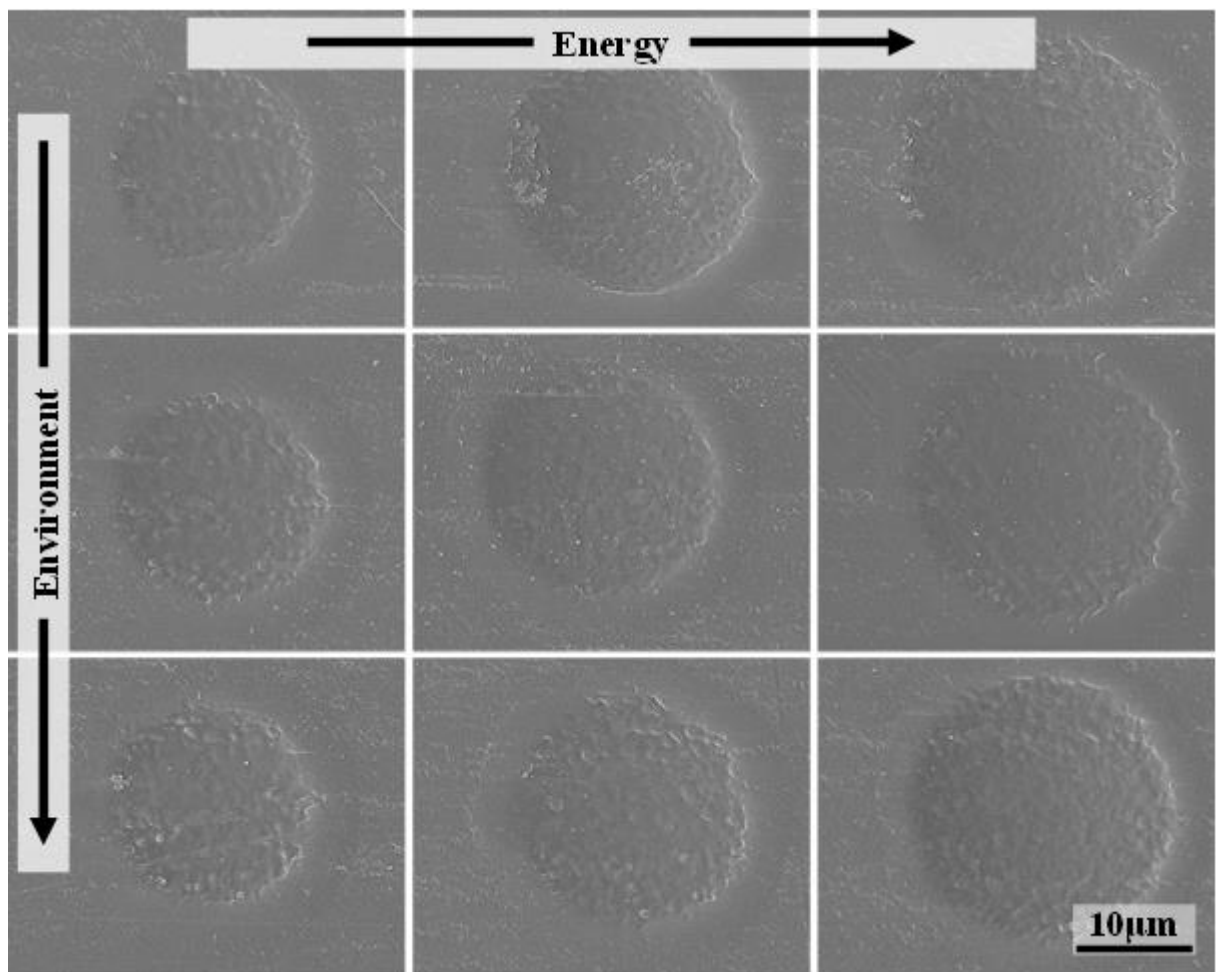
Figure 3.12: SEM images of realized structures at different laser energies and in different atmospheres for 1 laser pulse. From left to right: 1.35 mJ, 2.2 mJ, 4.5 mJ pulse energies, from top to down: Air, argon and vacuum (10^{-2} mbar) respectively.
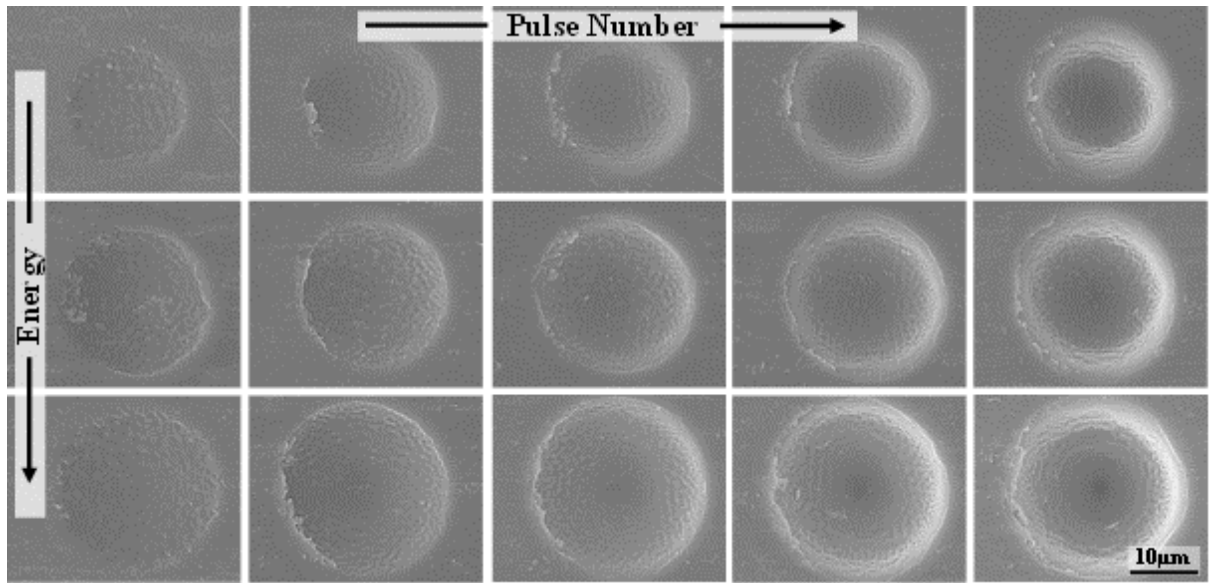
Figure 3.13: SEM images of treated PEEK surfaces: 1.35 mJ, 2.2 mJ, 4.5 mJ pulse energies and 1, 5, 10, 15, 20 pulses respectively.
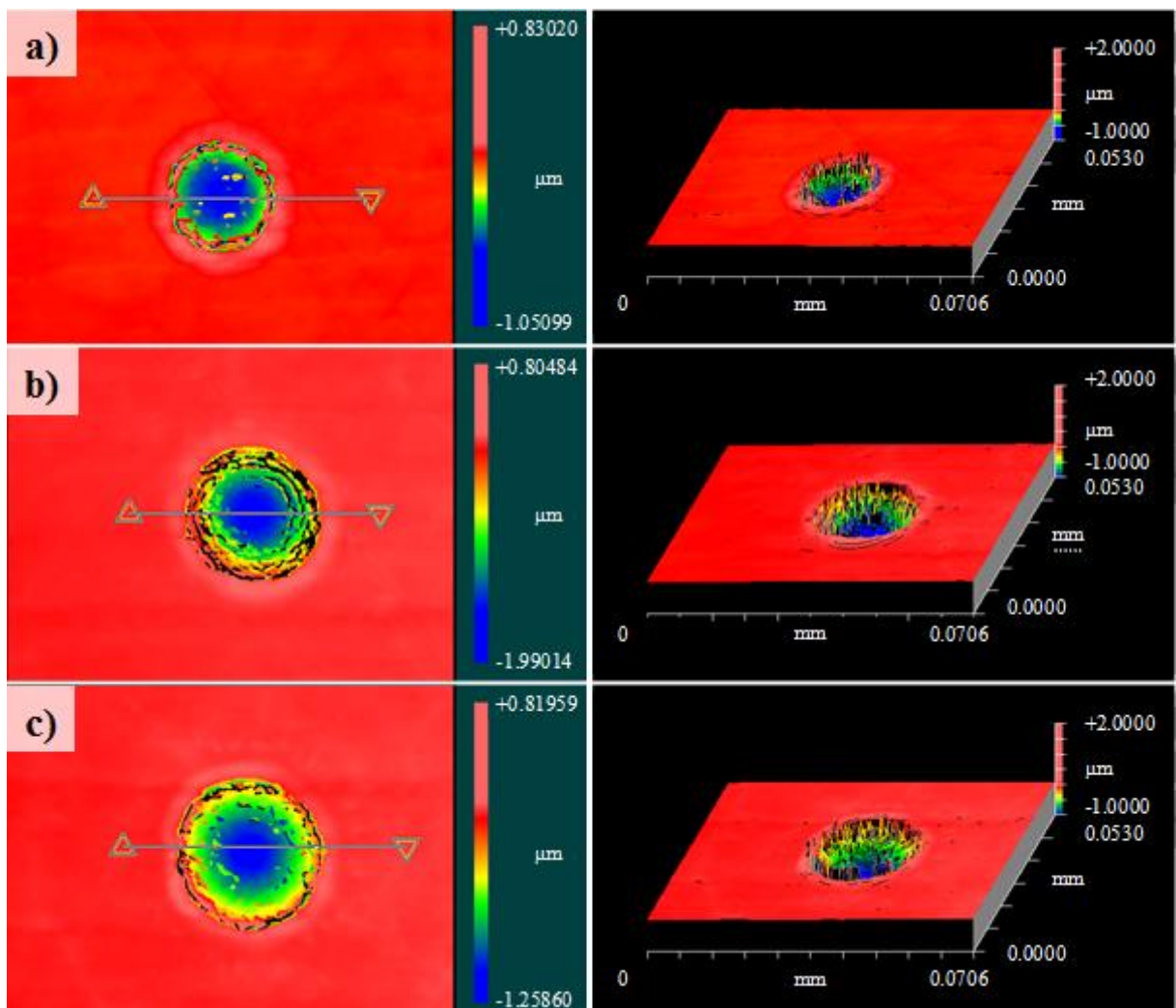
Figure 3.14: 2D and 3D whitelight interferometer images of PEEK surfaces treated by 1 laser pulse in air atmosphere at different energies a) 1.35 mJ, b) 2.2 mJ and c) 4.5 mJ.

In Figure 3.12, SEM images are presenting the energy and environmental differences on crater diameter and depth for single laser pulse. Energies are changing from 1.33 mJ to 4.5 mJ from left to right and environments are air, argon and vacuum (10^{-2} mbar) from top to down, respectively. Similar to Figure 3.12, in Figure 3.13 depths and crater diameters can be seen for energy and pulse number variations for air environment. The conic structures at 15 and 20 laser pulses at 4.5 mJ pulse energy can be seen clearly. As it mentioned before, crater diameters for the same energy lines are not changing dramatically. As an example, for air environment, at an energy of 4.5 mJ, crater diameter increase only around three micrometer (Table 3.1). This is also clear at Figure 3.13. This indicates that the experimental setup is adjusted in focal distance precisely. In comparison to SEM images, 2D and 3D images of whitelight interferometer can be seen in Figure 3.14 where the single laser pulse was carried out at different laser energies for air atmosphere as an example.

3.2.2 Laser Structuring of Alumina

The parameters that applied for PEEK surface treatment is not enough to treat alumina substrates due to its rigid structure. Therefore, in order to understand the effect of laser energy and pulse number on alumina plate treatment, energy values of 4.5 mJ, 8.9 mJ and 13.3 mJ were applied with 15, 20, 25, 30 and 35 pulses as given before in Table 2.3. However, defining the optimum depth for alumina plate is difficult unlike PEEK and NW surfaces due to its surface topography. Therefore, shapes of the structures and depths are affected from surface topography. Due to this reason, optimum experimental results from alumina plate substrates were selected as application parameters with microlens setup for cell test later on.

When the crater diameters were examined (Figure 3.15), it can be seen there, some of the craters are getting smaller while the laser pulse number is increasing unlike PEEK substrates. Primary reason may be the surface topography where the focused laser beam strike at the surface on a non-flat location. Secondary reason for this may be the laser energy fluctuations inside the laser itself. However, as can be seen from the standard errors, crater diameters of each parameter vary around their average value. Measured crater diameters of alumina substrate can be seen in Table 3.2-a. SEM images of treatments for different atmospheres versus pulse energy and for pulse number versus pulse energy are presented in Figure 3.16 and 3.17 to show crater diameter variation.
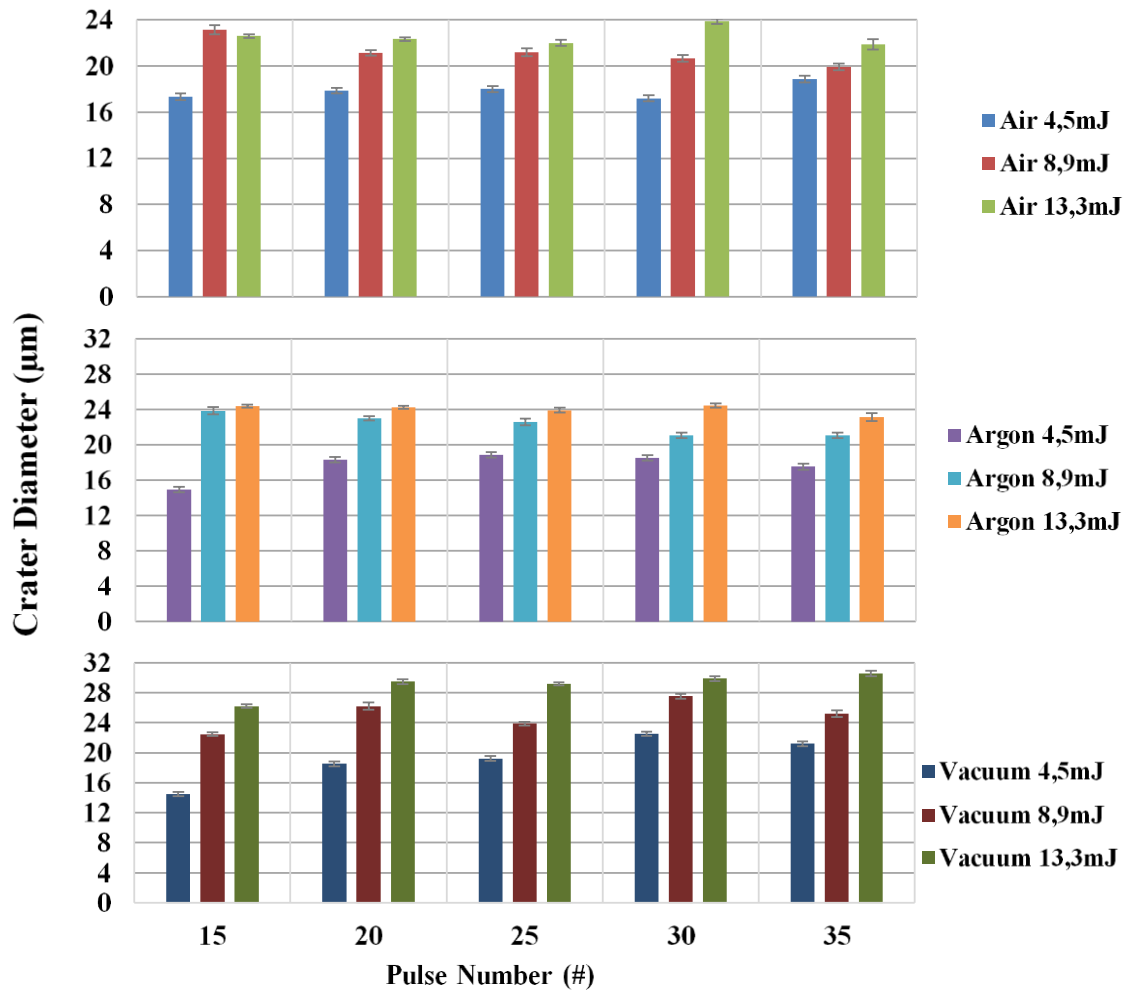
Figure 3.15: Crater diameter chart versus to laser pulse numbers. Degreasing of crater diameter in some energy parameters was observed. However, diameters are varying around the average value for energy lines.
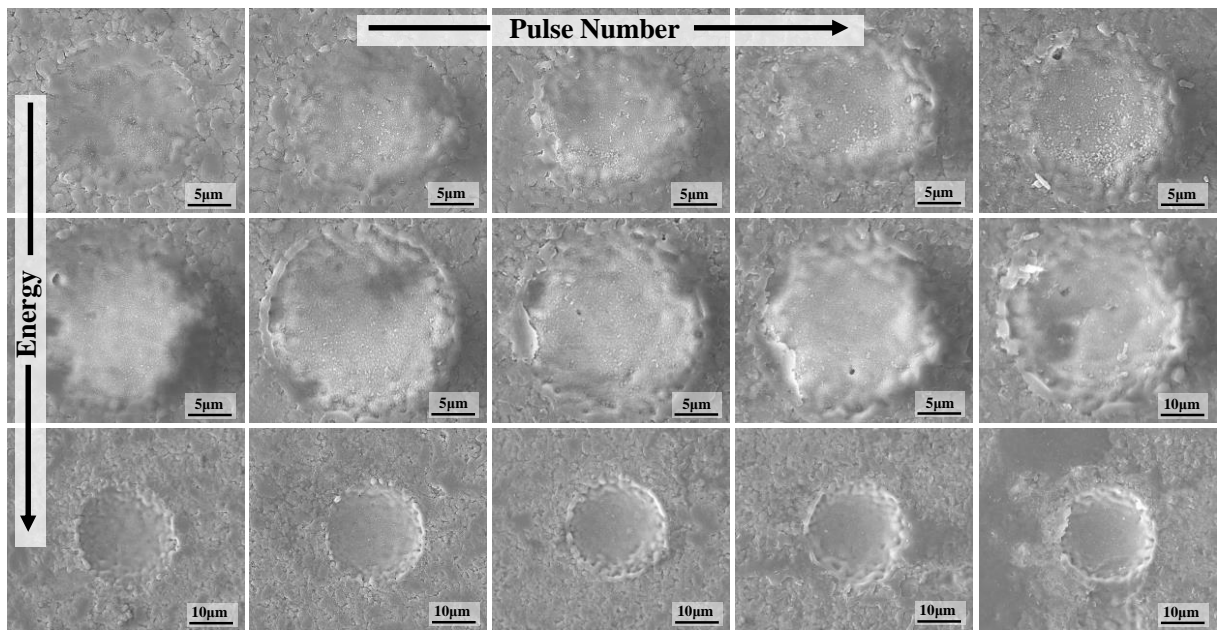
Figure 3.16: SEM images of alumina treatments with different pulse numbers and different energies in air. From left to right: 4.5 mJ, 8.9 mJ, 13.3 mJ pulse energies, from top to down: 15, 20, 25, 30, 35 pulses respectively.

Table 3.2: a) Crater diameters and standard errors b) Crater depths and standard errors of alumina plates in different environmental conditions and laser pulse numbers (units are in µm)

a)		4.5 mJ	8.9 mJ	13.3 mJ
Environment	#	Diameter (µm)		
Air	15	17.33 ± 0.28	23.13 ± 0.39	22.6 ± 0.17
	20	17.86 ± 0.26	21.13 ± 0.23	22.33 ± 0.16
	25	18.00 ± 0.28	21.20 ± 0.35	22.00 ± 0.27
	30	17.20 ± 0.28	20.66 ± 0.31	23.86 ± 0.23
	35	18.86 ± 0.28	19.93 ± 0.31	21.86 ± 0.46
Vacuum	15	14.46 ± 0.28	22.46 ± 0.22	26.20 ± 0.27
	20	18.53 ± 0.32	26.20 ± 0.47	29.46 ± 0.33
	25	19.20 ± 0.32	23.86 ± 0.26	29.20 ± 0.20
	30	22.53 ± 0.30	27.53 ± 0.31	29.86 ± 0.35
	35	21.20 ± 0.34	25.20 ± 0.43	30.53 ± 0.35
Argon	15	14.93 ± 0.29	23.86 ± 0.30	23.86 ± 0.30
	20	18.30 ± 0.31	23.00 ± 0.29	23.00 ± 0.29
	25	18.86 ± 0.32	22.60 ± 0.27	22.60 ± 0.27
	30	18.53 ± 0.32	21.06 ± 0.27	21.06 ± 0.27
	35	17.53 ± 0.32	21.06 ± 0.27	21.06 ± 0.27
b)		4.5 mJ	8.9 mJ	13.3 mJ
Environment	#	Depth (µm)		
Air	15	1.10 ± 0.09	2.04 ± 0.07	2.29 ± 0.08
	20	1.75 ± 0.14	2.60 ± 0.12	2.80 ± 0.15
	25	2.25 ± 0.08	3.16 ± 0.10	3.46 ± 0.07
	30	2.81 ± 0.09	3.63 ± 0.09	4.22 ± 0.09
	35	3.01 ± 0.11	4.36 ± 0.11	5.15 ± 0.14
Vacuum	15	0.87 ± 0.09	1.45 ± 0.09	1.92 ± 0.08
	20	0.91 ± 0.11	1.81 ± 0.13	2.29 ± 0.08
	25	1.28 ± 0.10	1.86 ± 0.08	2.56 ± 0.06
	30	1.36 ± 0.10	2.30 ± 0.13	2.90 ± 0.12
	35	1.97 ± 0.14	3.04 ± 0.12	3.37 ± 0.16
Argon	15	1.27 ± 0.09	2.21 ± 0.07	2.27 ± 0.08
	20	1.86 ± 0.11	2.64 ± 0.10	2.76 ± 0.11
	25	2.30 ± 0.09	3.16 ± 0.09	3.39 ± 0.10
	30	2.88 ± 0.12	3.56 ± 0.11	4.16 ± 0.12
	35	3.08 ± 0.13	3.94 ± 0.13	4.81 ± 0.12
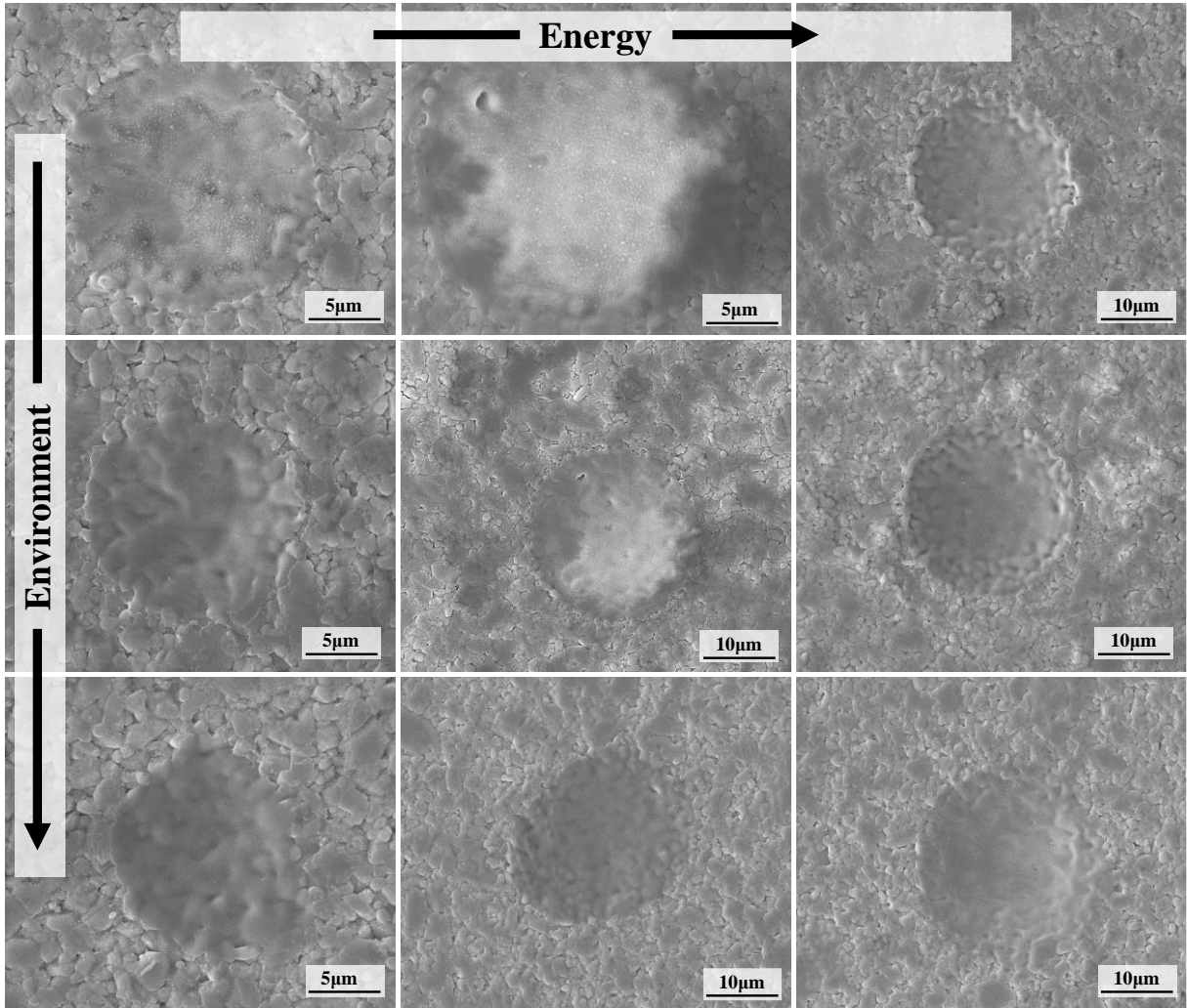
Figure 3.17: SEM images alumina structures achieved at different laser energies in different atmospheres for 15 pulses. From left to right: 4.5 mJ, 8.9 mJ, and 13.3 mJ pulse energies, from top to down: air, argon, vacuum.
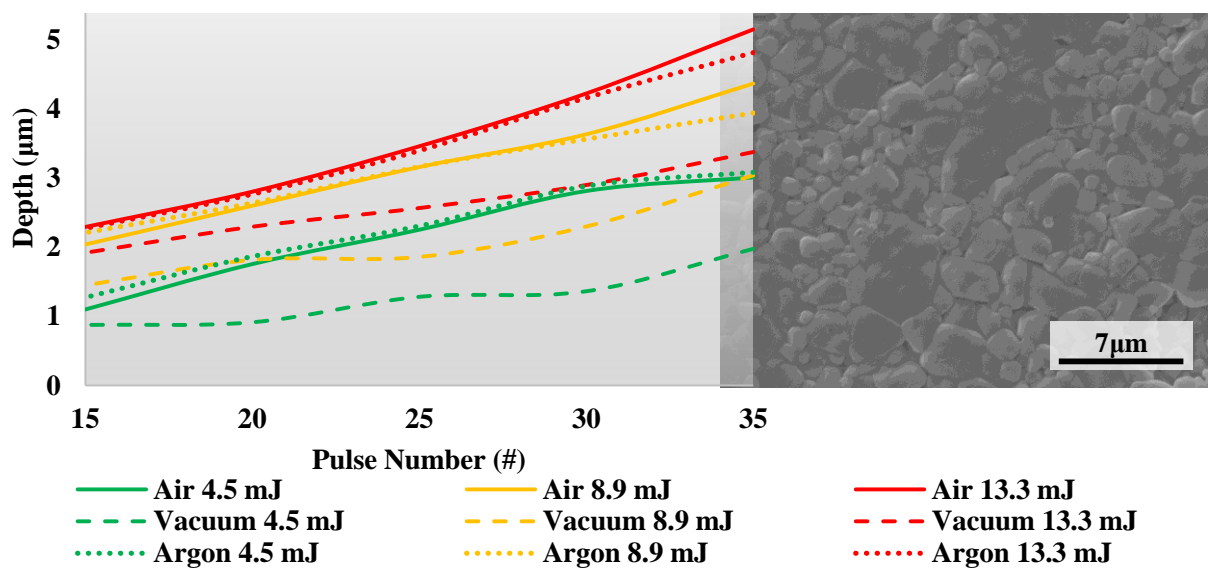
Figure 3.18: Depth of laser treated structures versus to laser pulse number for alumina substrate. Depths are increasing linearly.

Linear graphs for depth distributions are given in Figure 3.18. It can be seen there some curves are slightly out of the general linearity where the surface roughness has clear effects on structuring process. However, the observed variations are still in an ignorable range and all data can be seen in Table 3.2-b. In order to show the roughness of the ceramic surface visually, SEM image of non-treated ceramic surface is given in Figure 3.18. Similar to the PEEK substrates, ablation rate versus to applied laser fluence was investigated for alumina substrates too. It was observed that the ablation rate shows linear increasing with the increased laser fluence. Distribution is given in Figure 3.19. When the plots of air and argon checked they can be considered as same for the ablation rates, however, the vacuum plot starts from a lower value although it has closer slope to the others.
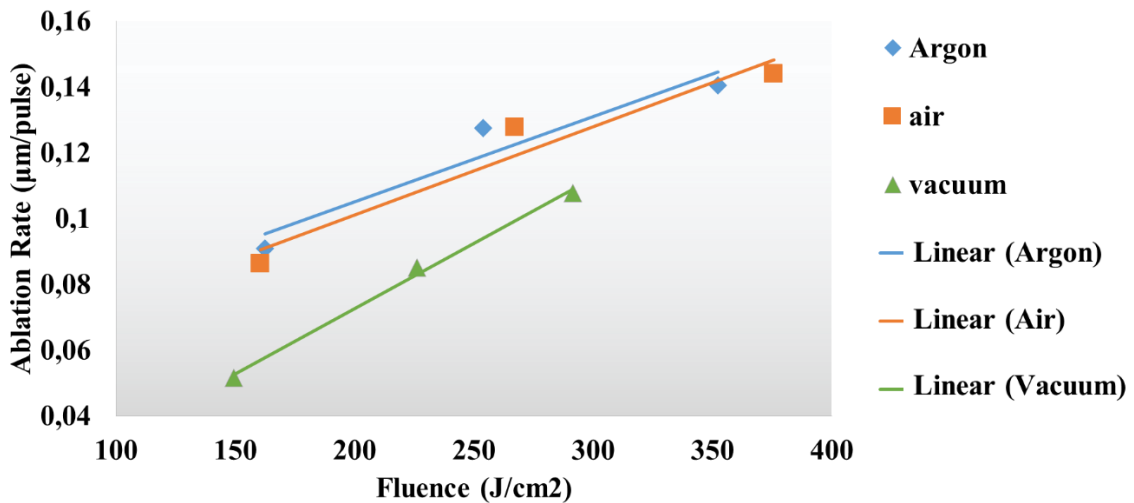
Figure 3.19: Laser induced alumina ablation rate versus to laser fluence. For air and argon the ablation rate can be considered as same.

In order to see the depth variation of alumina plates versus to energy differences, depths measurements versus to laser pulse energy and pulse number are given in Figure 3.20. It is clear from the graph that the depths of the structures are following the laser pulse energy. However it is not possible to see a linear increment for crater diameters. In Figure 3.21, 2D and 3D images from the whitelight interferometer can be seen. Whitelight interferometers use a specially designed magnifying objective to focus broadband light source over substrate surface and scan the surface in z-axis with a specific step. However, it gets difficult or in some cases impossible to collect data from alumina substrates due to the unordinary reflections. Thus, such missing data are shown as black in image. On the other hand, in this case, it is possible to collect data from the bottom of the structure because of the smooth laser drill which allows measurement of the structure depths.
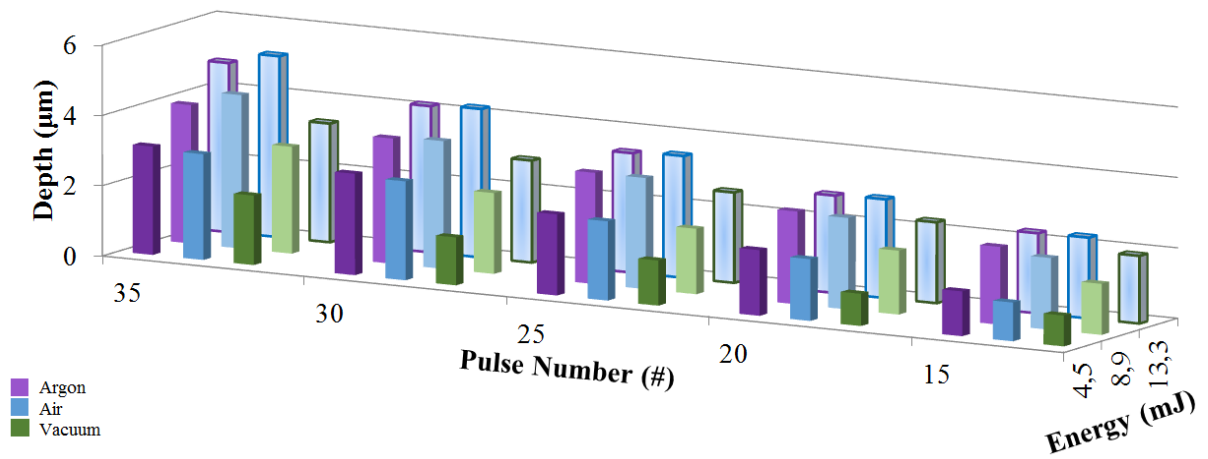
Figure 3.20: Depth distribution variations by laser pulse energy, pulse number and atmospheric conditions of alumina substrate
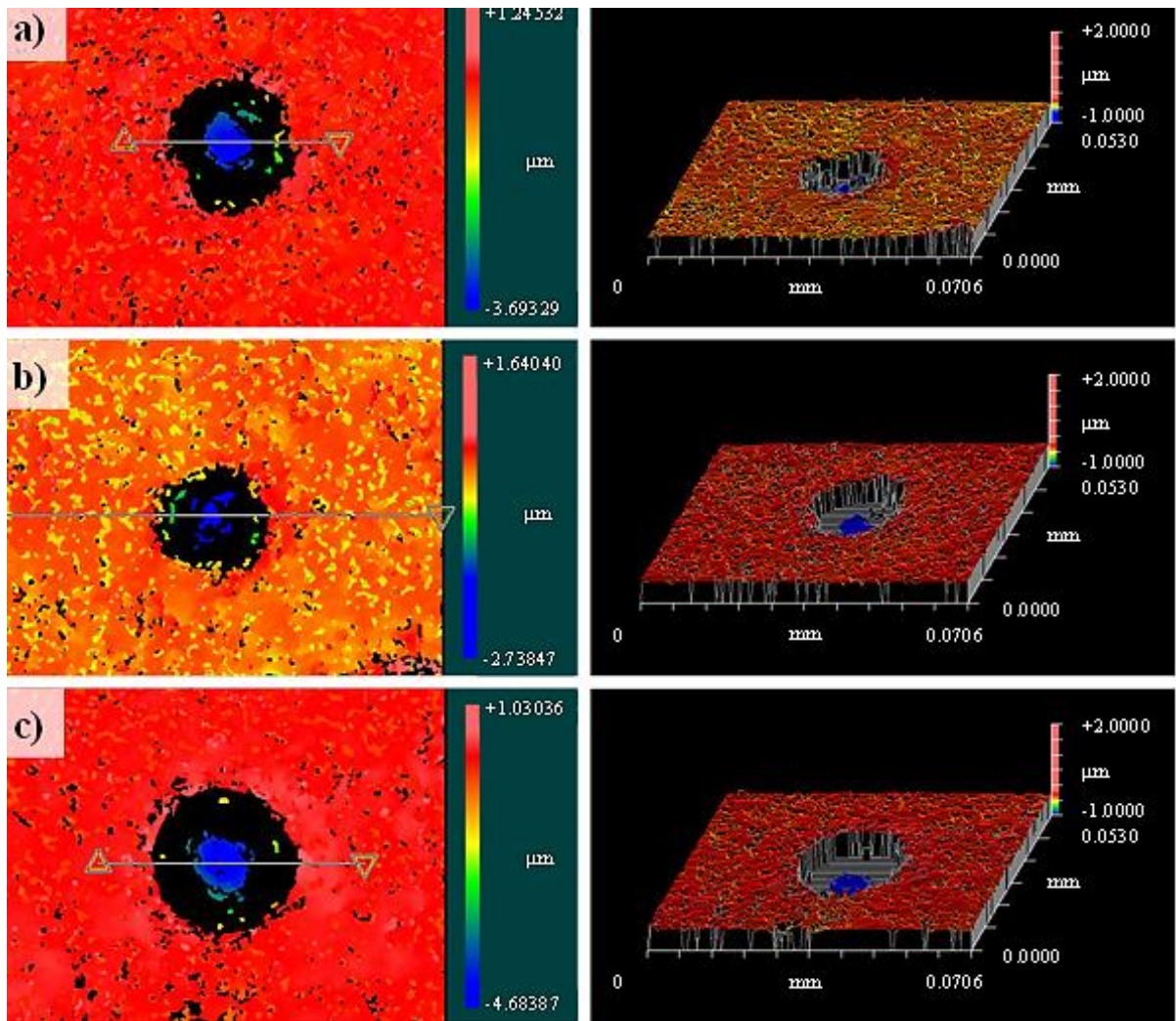
Figure 3.21: 2D and 3D whitelight interferometer images of 35 laser pulse in air atmosphere with different energies a) 4.5 mJ, b) 8.9 mJ and c) 13.3 mJ

3.3   PLD of Titanium and Alumina on Glass Substrates for Homogeneity and Thickness Determination

3.3.1   Homogeneity Determination of PLD

As mentioned previously, Ti was deposited on glass substrates for the determination of the PLD process for homogeneity at three different deposition techniques (Section 2.2.4.3). Visual deposition results can be seen in Figure 3.22 for single beam PLD, MS-PLD and double beam PLD.
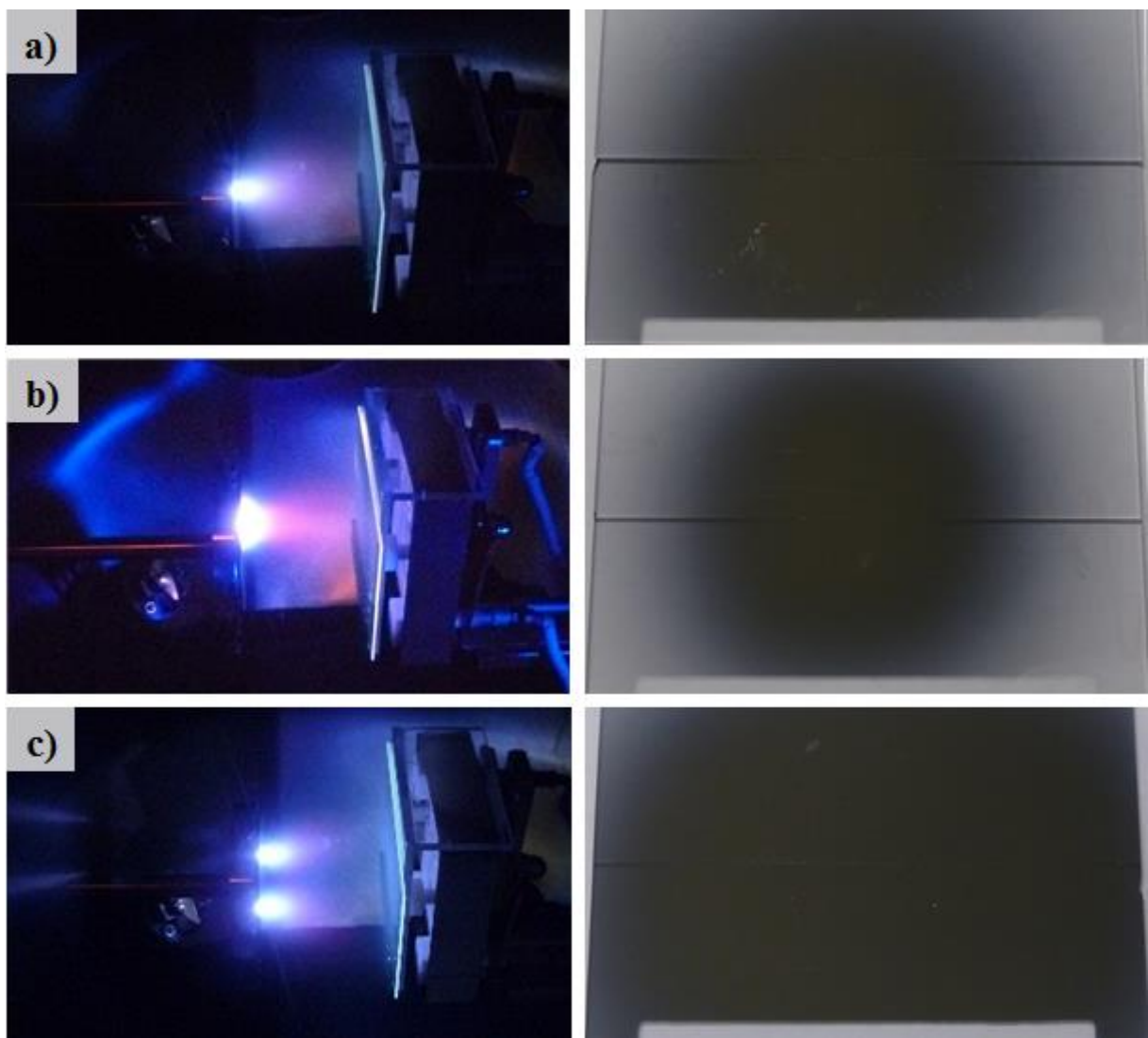
Figure 3.22: Photos of deposition methods. a) Single beam PLD, b) MS-PLD and c) Double beam PLD. The deposition results are given in the next of each method respectively. Non coated areas at the bottom of the glass substrates are the locations where the sample holder blocks the deposition.

Homogeneity of the deposited Ti layers on glass substrates were tested with the self-made device as explained in section 2.4.6. Measurements were performed at the top of the glass slide (totally coated part), Homogeneous layers were accepted down to 80% of the central thickness. Results from the deposited layers are presented in Figure 3.23.
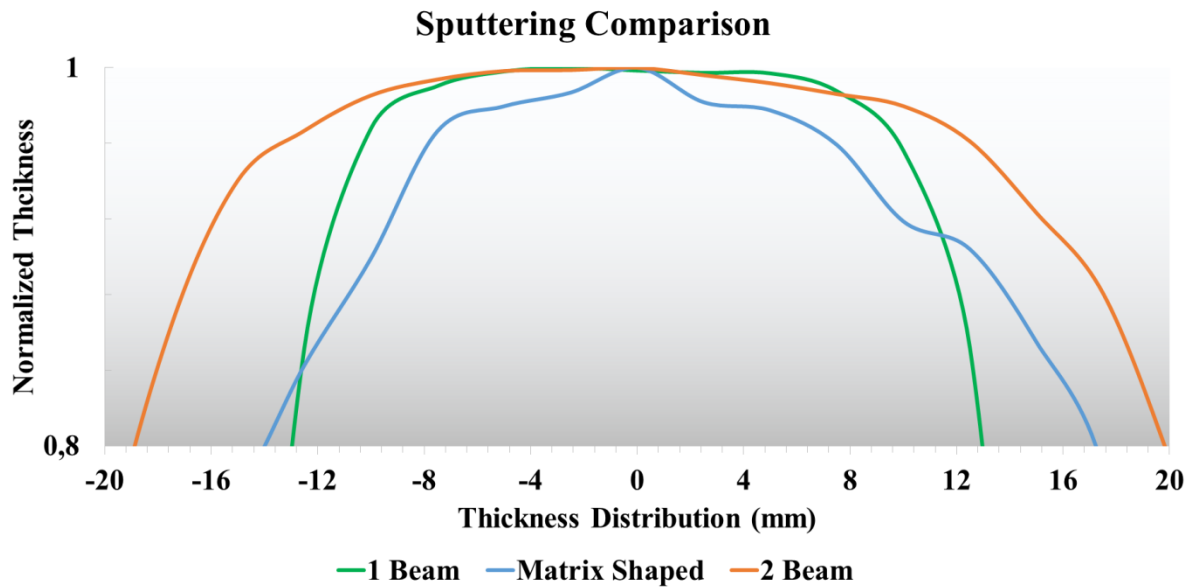
Figure 3.23: Thickness distribution of single beam, double and MS-PLD deposition techniques.

3.3.2 Determination of the Deposited Alumina Layers by Double Beam PLD

From the section 3.3.1, double beam PLD technique was selected as homogeneous layer distribution and thin alumina deposition on PEEK substrates were carried out with double beam PLD technique. Depositions were performed for 10 and 20 min at 35 mJ, 60 mJ and 100 mJ laser pulse energies for each beam. During the depositions, distance between the laser beams on the target surface was fixed to 15 mm.

Table 3.3: R_a values of deposited alumina layers over silicon wafers (in comparison to non-coated silicon wafer).

Substrate	35 mJ	60 mJ	100 mJ	35 mJ	60 mJ	100 mJ	Si
R_a Values (nm)	0.470	0.442	0.476	0.602	0.421	0.504	0.504
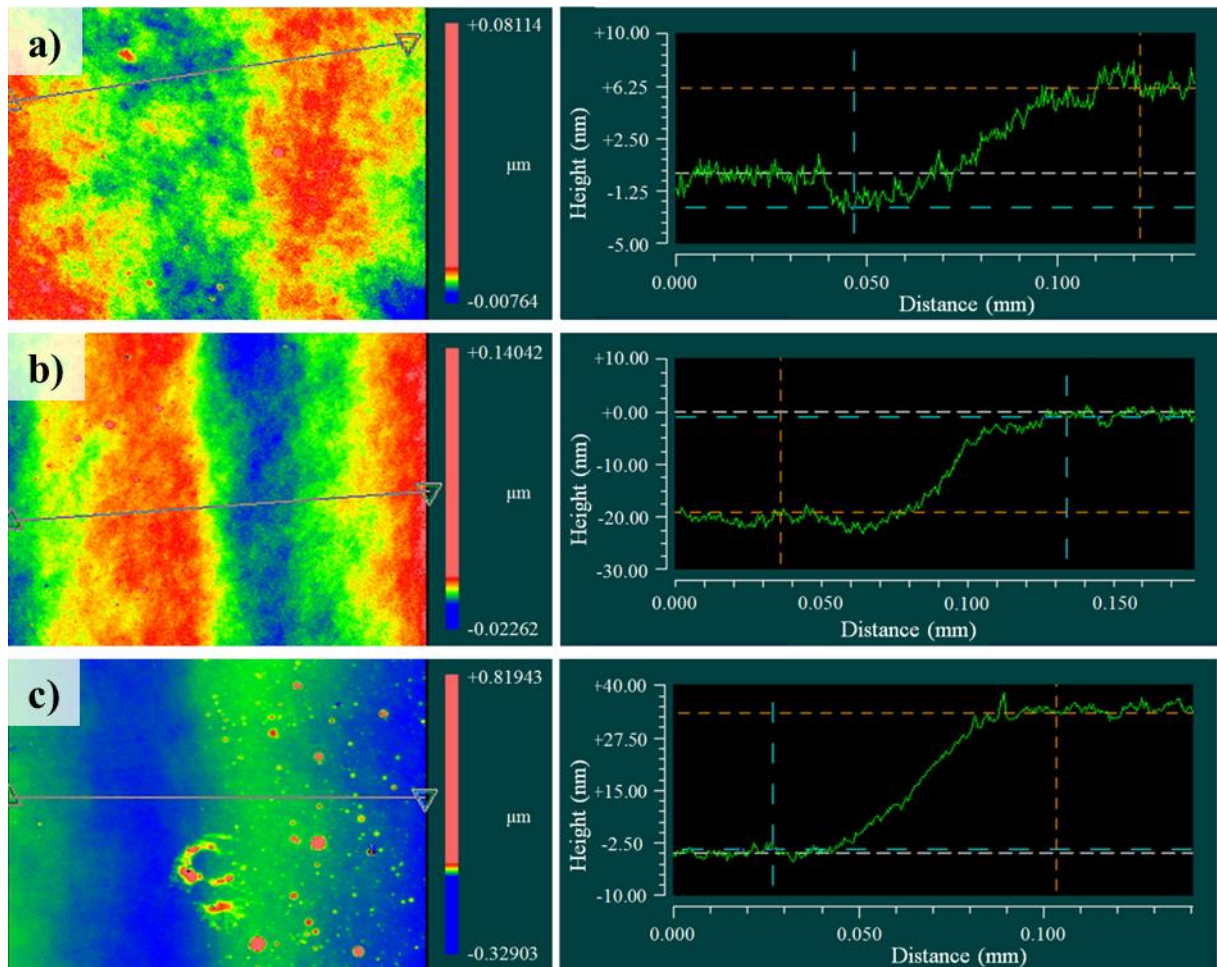
Figure 3.24: Whitelight interferometer images for 10 minutes double beam deposition of alumina over glass substrates. a) 35 mJ energy, b) 60 mJ energy and c) 100 mJ energy per beam

Deposition thicknesses were measured with whitelight interferometer from the interface of the non-coated and the coated area on the glass substrates (Figure 3.22-c Right: Bottom of the glass slide). From the homogeneity determination by Ti layer, it was observed that the location for the performed measurements of the alumina layer was found at 80% thickness point. Therefore, measurements were corrected by this factor to their central thicknesses. Whitelight interferometry images from the measurements are given in Figure 3.24 and 3.25 for 10 min and 20 min deposition periods respectively. Graph of the thickness values versus to laser beam energy for 10 min and 20 min deposition times are given in Figure 3.26. Deposition rates were calculated from the measured thicknesses and found as 0,014 Å/pulse for 35 mJ beam energy, as 0,034 Å/pulse for 60 mJ beam energy and as 0,051 Å/pulse for 100 mJ beam energy. Roughness measurements of the depositions on silicon wafer surfaces were measured by using whitelight interferometer and given in Table 3.3 in comparison to non-deposited silicon substrates.
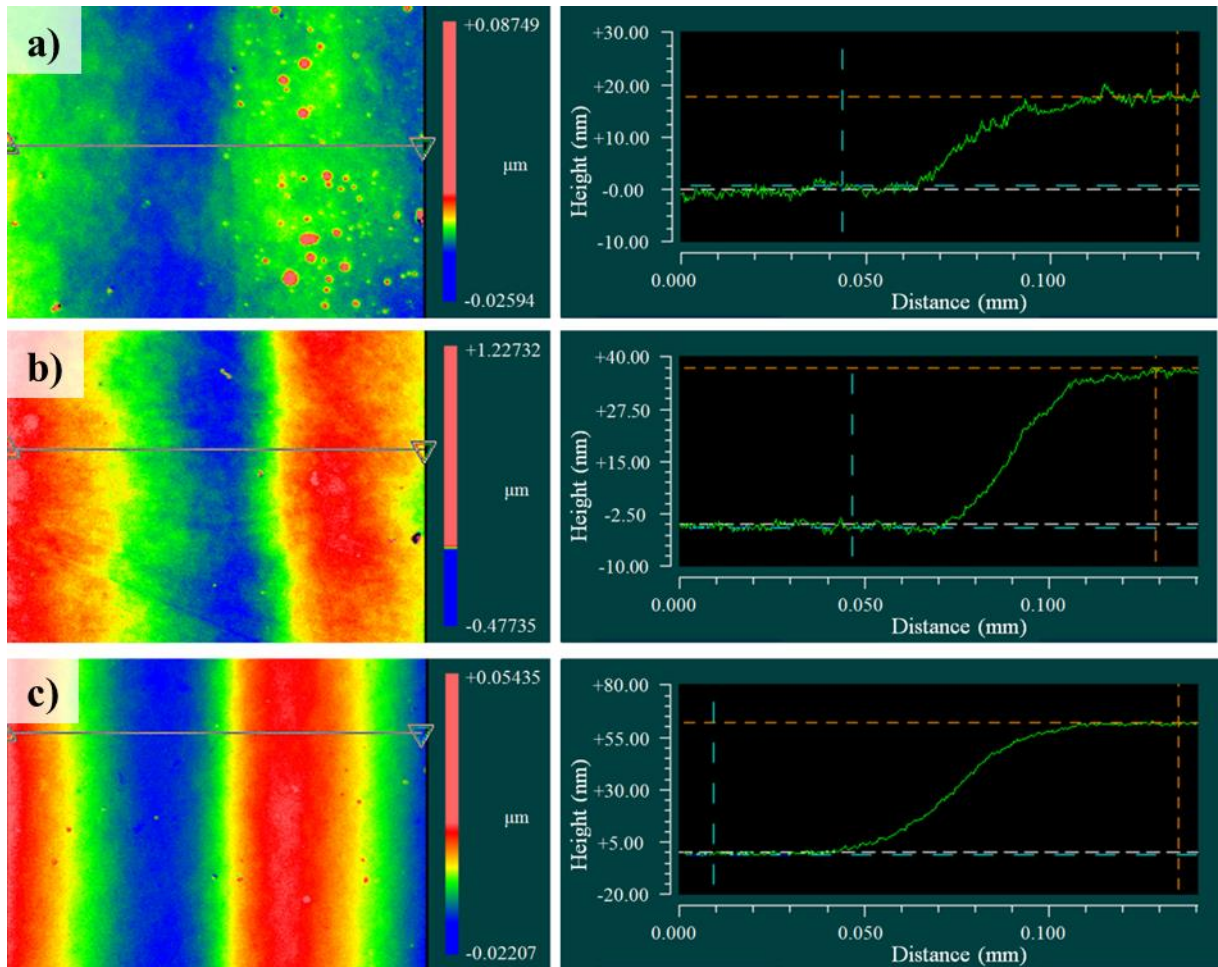
Figure 3.25: Whitelight interferometer images for 20 minutes double beam deposition of alumina over glass substrates. a) 35 mJ energy, b) 60 mJ energy and c) 100 mJ energy per beam.
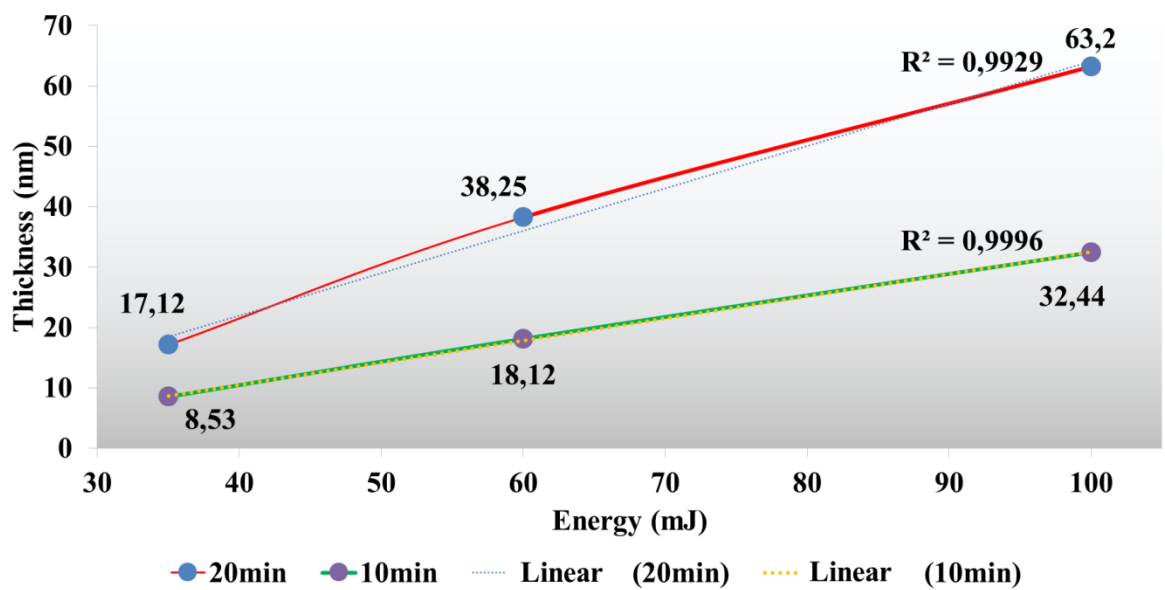
Figure 3.26: Corrected central thickness distribution of double beam alumina deposition over glass substrates at different laser beam energies. (Measured thicknesses are inserted to the graph.)

In Figure 3.26, it is clear to mention that coating thickness increases when the laser beam energy increases and R^2 numbers show that the increasing shows highly linear behavior. It can be seen in Figure 3.24 and 3.25, deposited layers are highly smooth however some particles were detected. These can be the characteristic result of PLD application where such droplets can be seen on the grown film (Eason R 2007). Deposited layer on silicon wafers were examined by SEM additionally (Figure 3.27). Similar surface structures were observed as whitelight interferometer. During the SEM imaging, EDS spectrums were collected simultaneously to see aluminium and oxygen peeks from the silicon wafers.
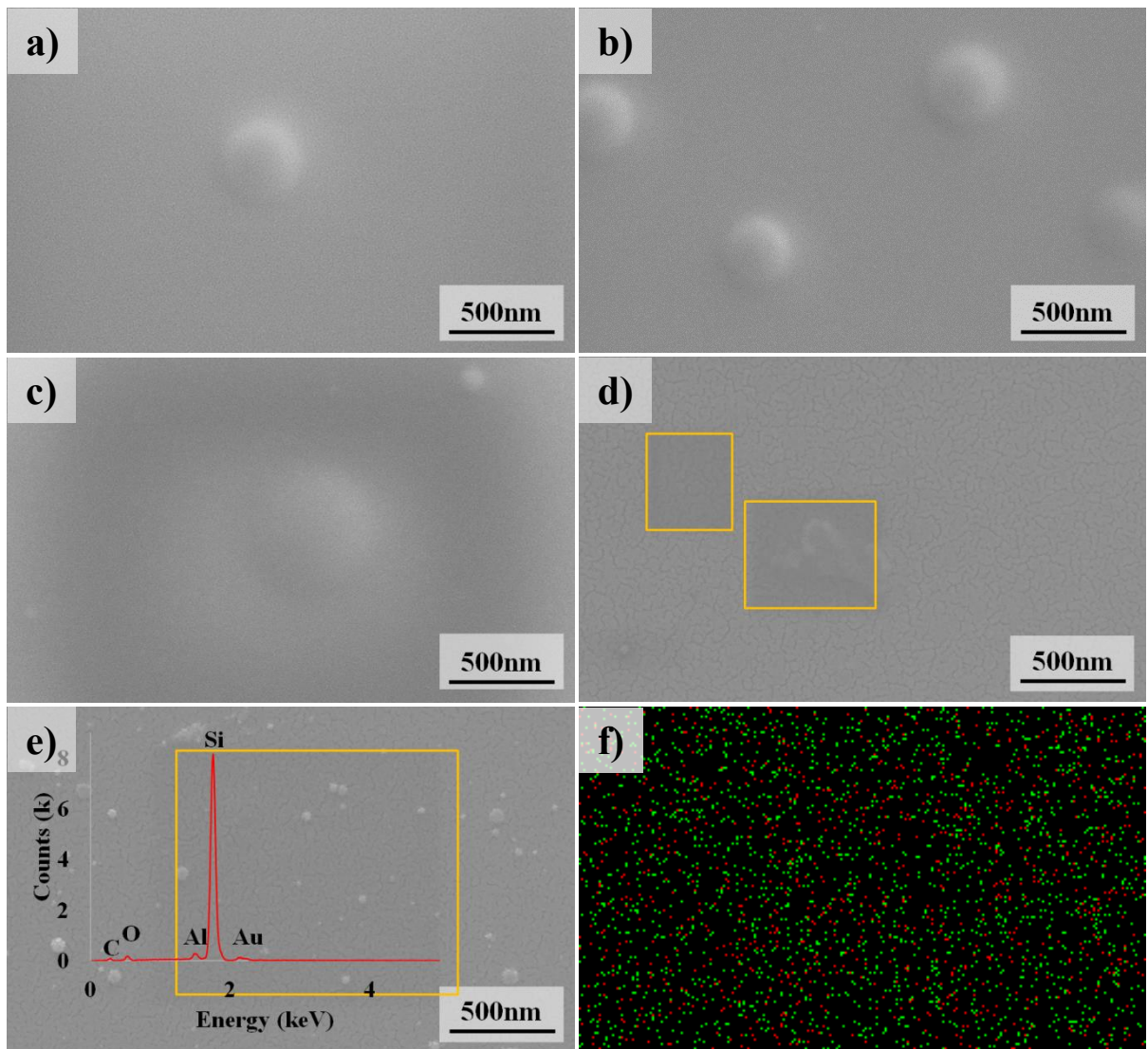
Figure 3.27: SEM micrographs of double beam alumina layers with: a) 100 mJ, b) 60 mJ and c) 35 mJ laser beam energies. d) Image of non-coated silicon wafer surface and e) Coated silicon wafer surface inserted with EDS spectrum. Yellow boxes indicate the locations where the EDS spectrums were collected. f) Mapping method by EDS: Green dots indicate aluminum atoms while red dots indicate oxygen atoms over the surface.

3.4 Microlens Array Laser Structuring of PEEK and Alumina Substrates and Pulsed Laser Deposition of Alumina on Treated PEEK surface

As mentioned before, defined laser energy and pulse parameters from the single lens surface structuring (section 2.2.3.1-2 and section 3.2.1-2) were applied to the alumina plates, Al/Al$_2$O$_3$ core/shell NWs, PEEK plates and plasma treated PEEK substrates. Following the structuring of the surfaces, PEEK substrates were coated with ultra-thin alumina layer by double beam PLD technique. Schematic illustration of the processes PEEK substrates (in order to perform alumina coated PEEK substrates) can be seen in Figure 3.28.
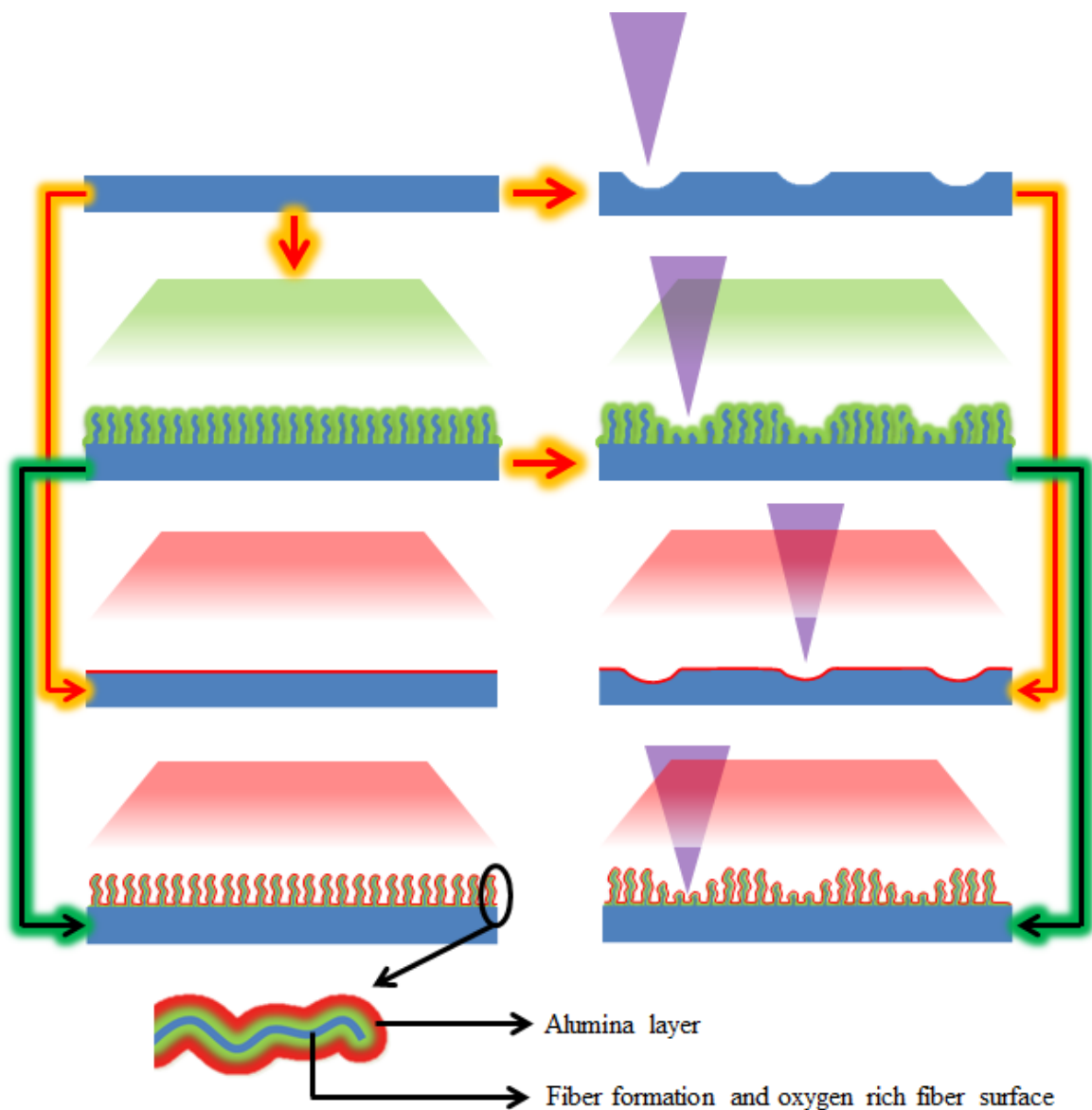
Figure 3.28: Schematic illustration of alumina coated PEEK substrates preparation as a flow diagram. Below magnified illustration of a final single PEEK fiber can be seen. Purple indicates the laser beam in focus while green and red are indicating the plasma and PLD processes respectively.

Deposition of the ultra-thin alumina layers on PEEK surfaces (alumina deposited non-treated PEEK substrate (*NT-PLD*), alumina deposited laser-treated PEEK substrate (*LT-PLD*), alumina deposited plasma treated PEEK substrate (*PT-PLD*) and alumina deposition following the plasma and laser treatments of PEEK substrate (*PLT-PLD*))were examined with SEM in order to see the effects of PLD process on these surface types. Non-treated (*NT*) and *NT-PLD* substrates can be seen in Figure 3.29 and 3.30. Figure 3.29-c and -d are the *LT-PLD* substrates. It is clear that deposited layers are perfectly smooth and is not altering the surface topography. Some alumina particles can be seen at the surfaces (Figure 3.29-c) which are the characteristic results of PLD application as mentioned before. They can be ignored due to their low particle density on the surface and small sizes.
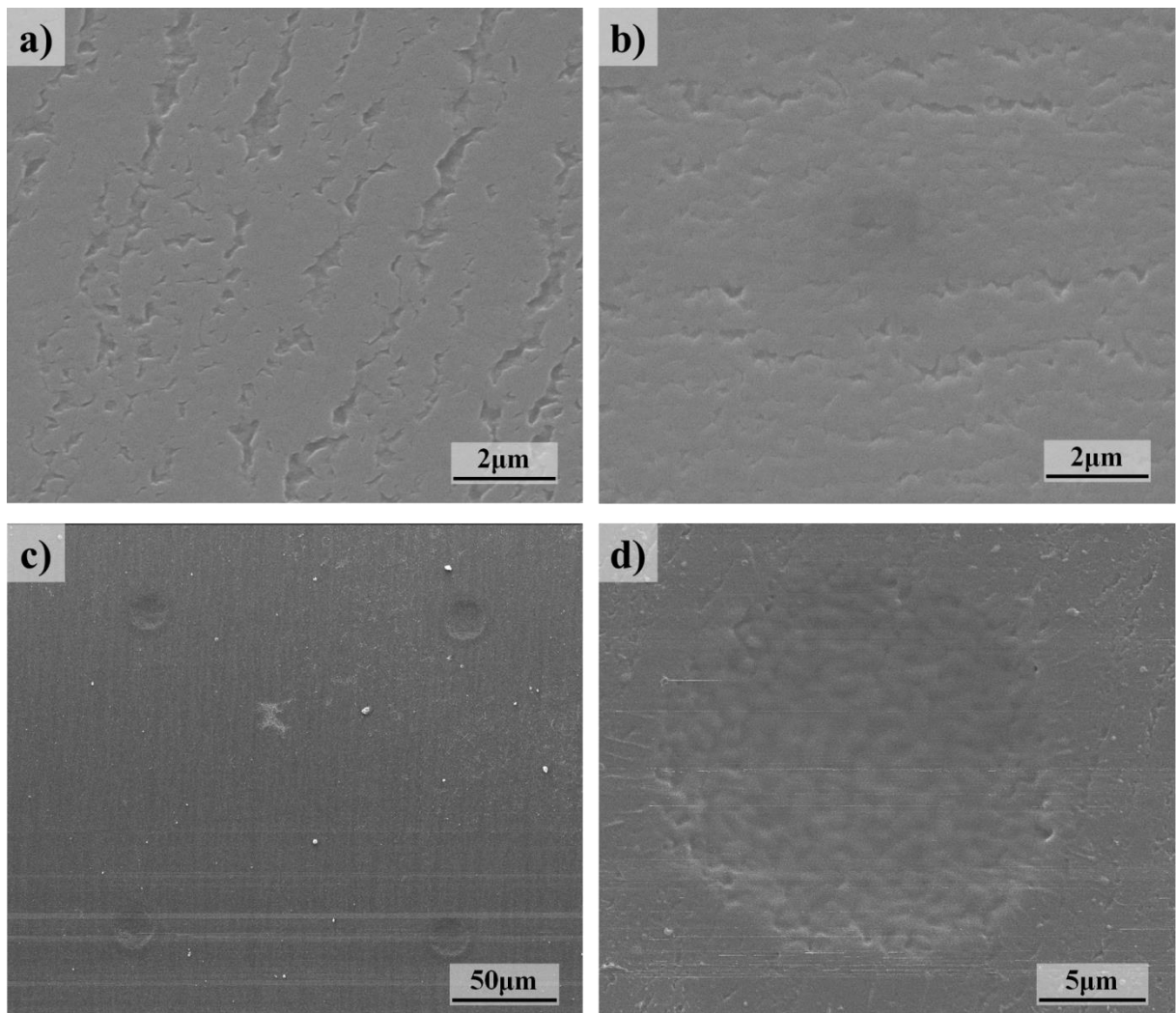
Figure 3.29: SEM images of a) *NT-PEEK* substrate in comparison to b) *NT-PLD*. c) and d) are the alumina deposited samples after laser treatment with single laser pulse at 7.5 mJ laser output energy which is the optimum laser pulse energy for PEEK surface structuring.
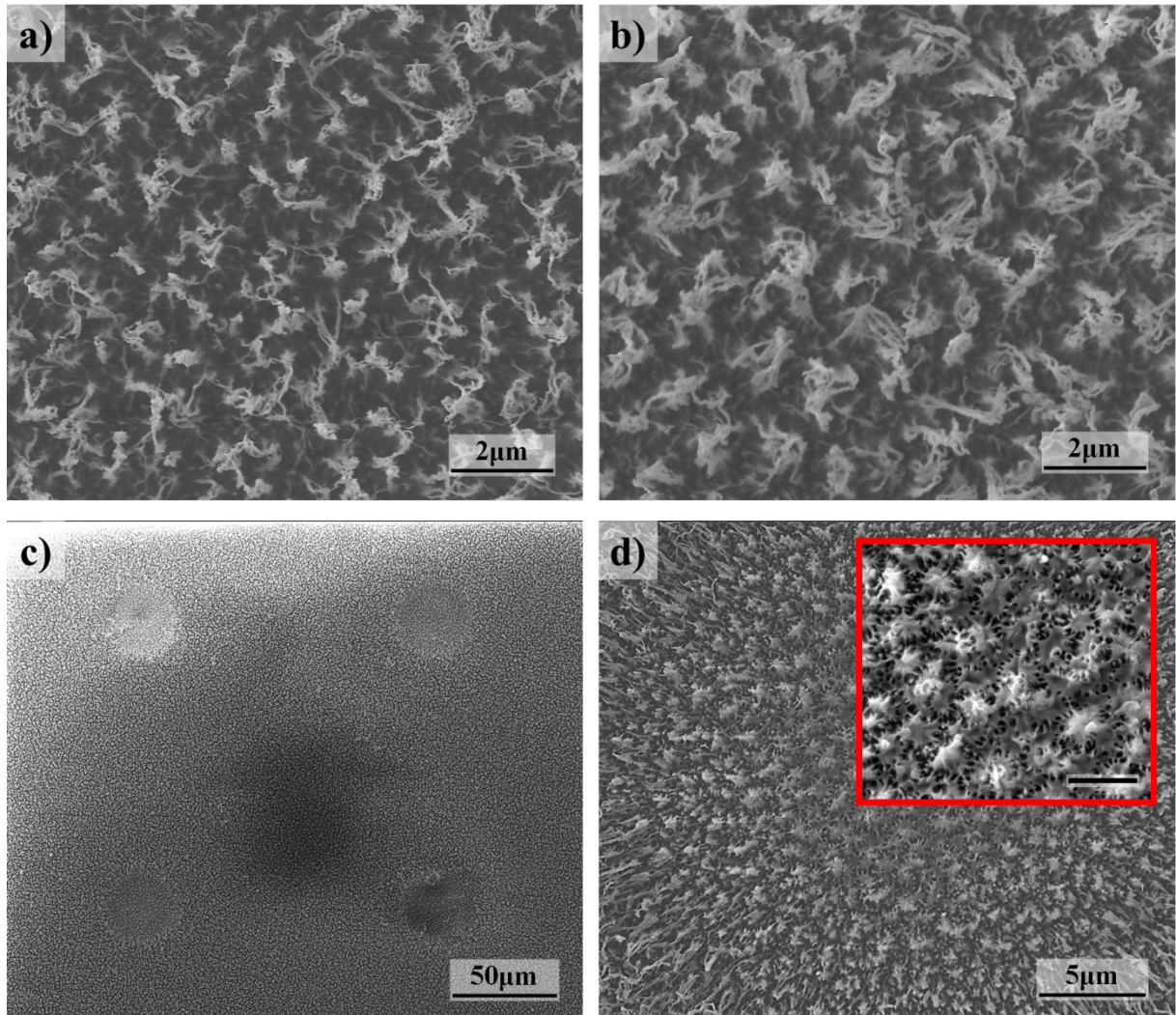
Figure 3.30: SEM micrographs of a) Plasma treated (*PT*), b) Alumina deposited substrate after plasma treatment (PT-PLD), c) and d) Alumina deposited substrate after plasma and laser treatment processes (*PLT-PLD*). Inset pictures shows the close look to the inside of the laser treated area (scale bar is 2 μm).

As can be seen in Figure 3.30-a and -b, thickness of the PEEK NWs by plasma treatment (*PT*) are increasing after alumina deposition. *PLT-PLD* substrates are given in 3.30-c and with high magnification in -d. Reformed micro structures with nano structures beneath after laser pulse can be seen at the center of the laser spot on *PLT-PLD* substrate. High magnification images for the thickness comparison are represented in Figure 3.31-a for *PT* sample and 3.31-b for *PT-PLD* sample. SEM images proof that the alumina deposition is smooth and not altering the original NW topography. Thinnest fiber diameter was measured as around 20 nm and 32 nm for the *PT* and *PT-PLD* substrates respectively and the mean values of the overall fibers were measured as 29±0.8 nm for *PT* and 40 nm±2.4 nm for *PT-PLD* substrates.
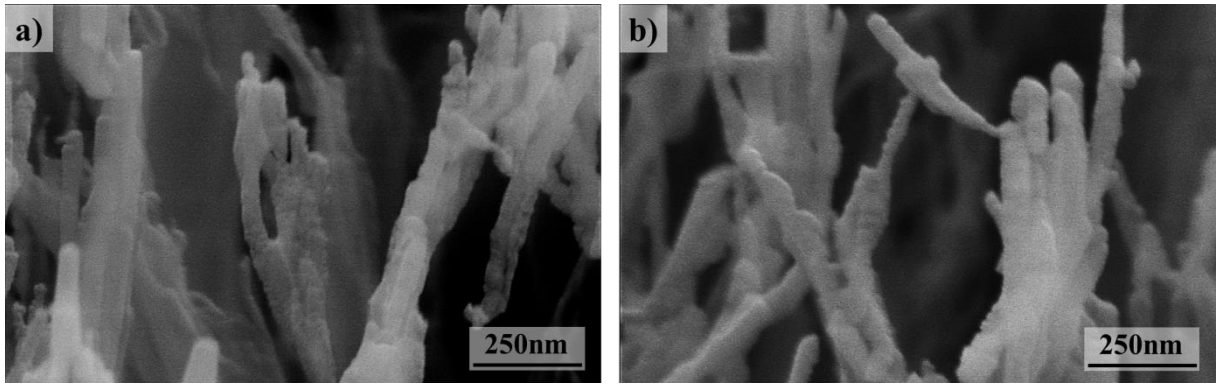
Figure 3.31: High magnification images of PEEK NWs a) Plasma treated (*PT*), b) Alumina coated and plasma treated (*PT-PLD*) NWs. Measured thicknesses are 29±0.8 nm before and 40 nm±2.4 after deposition for the single NW.
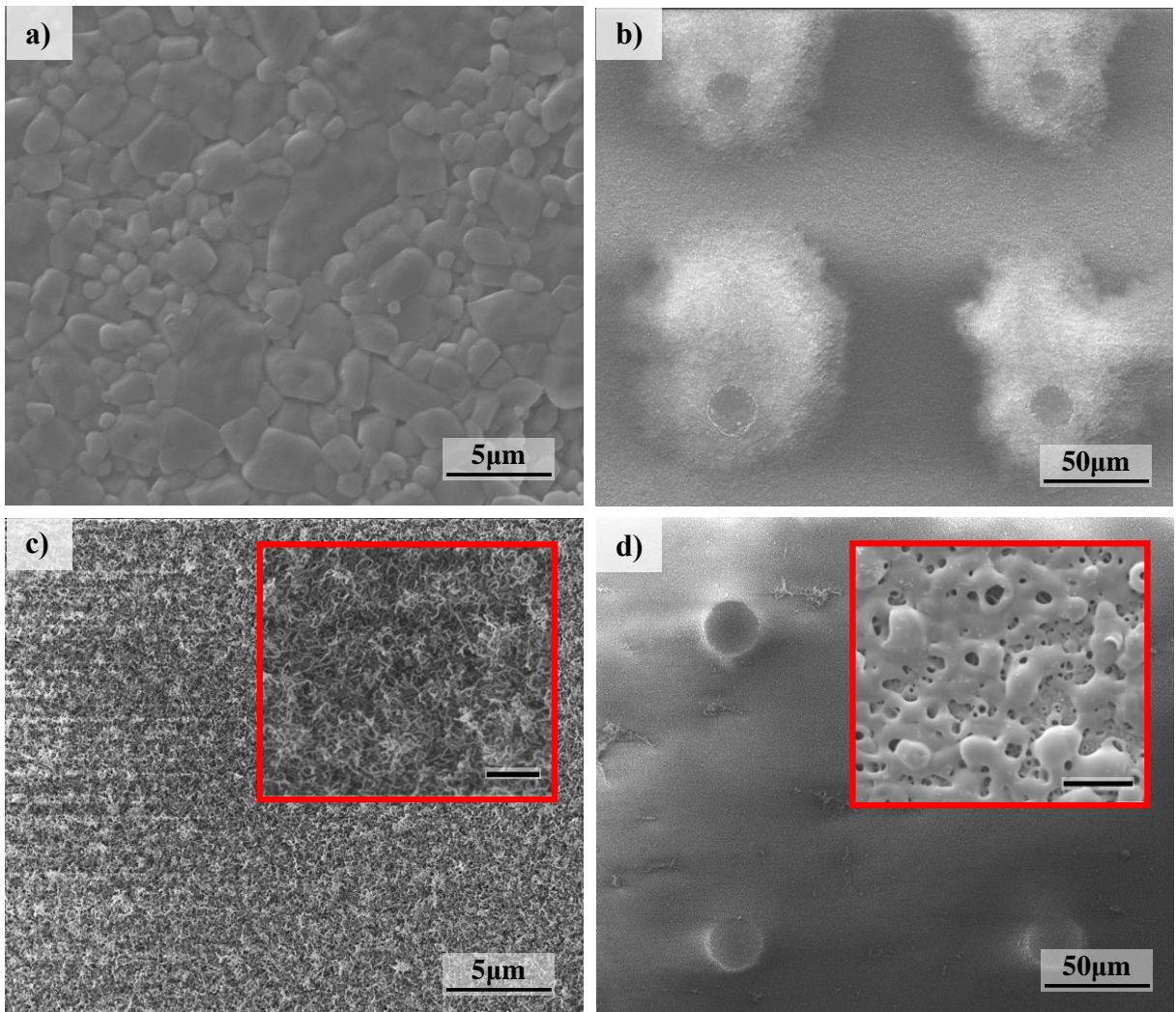
Figure 3.32: SEM images of alumina substrates. a) *NT-Al*, b) *LT-Al*, c) *NT-NWs* (insert: Zoom image with 1 μm scale bar), d) *LT-NWs* (inset: Zoom image of treatment with 2 μm scale bar).

In Figure 3.32, SEM images of laser surface structured substrates with microlens array setup are given for the alumina plates (*LT-Al*) and Al/Al$_2$O$_3$ core/shell NWs (*LT-NW*) together with the non-treated alumina plates (*NT-Al*) and non-treated Al/Al$_2$O$_3$ core/shell NWs (*NT-NW*). Distance between the periodic structures for *LT-Al*, *LT-NW*, *LT-PLD* and *PLT-PLD* substrates are defined by the microlens array and fixed to 150μm in both x- and y- axis.

Depths of the created micro structures with microlens array together with the diameter data for all substrates are given in Table 3.4.

Table 3.4: Diameter and depth measurements of laser treated surface

Laser Treatments	Al/Al$_2$O$_3$ NW	Alumina Plate	*LT-PLD*	*PLT-PLD*
Diameter (μm)	20±0.23	17±0.28	17±0.25	25±0.32
Depth (μm)	0.550±0.06	1.100±0.09	0.624±0.01	1.270±0.04

3.4.1 Chemistry Determination of Alumina layers on PEEK Substrates
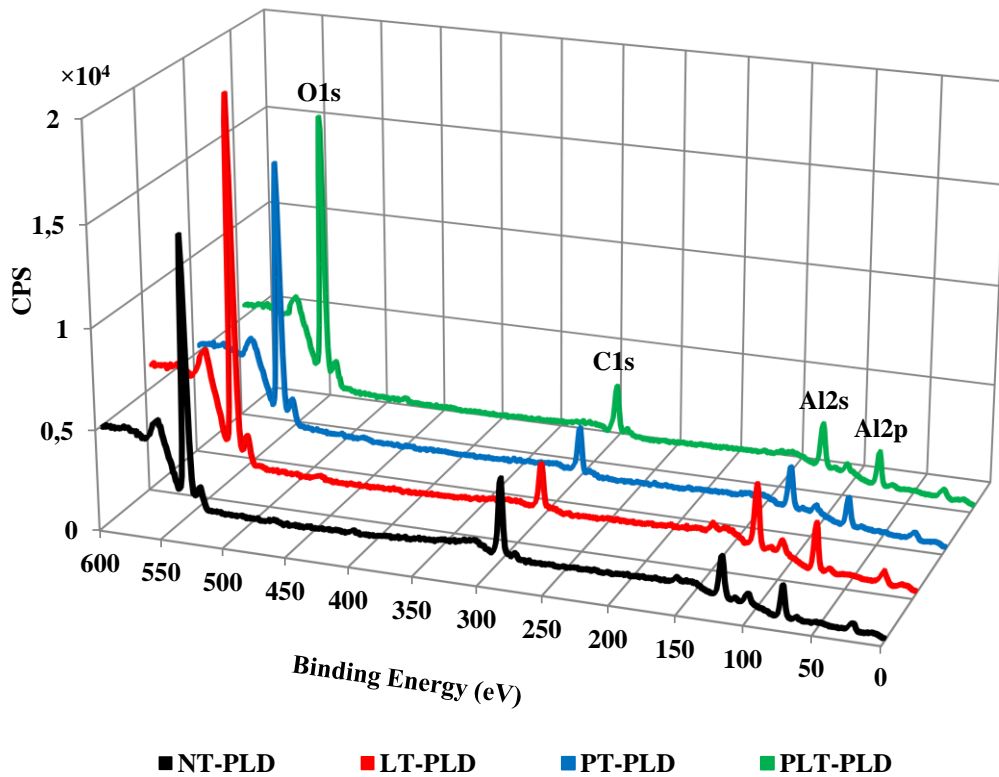
Figure 3.33: XPS measurements of alumina deposited PEEK substrates. It is clear that all the substrates have the same distribution.

XPS measurements were performed for the alumina deposited PEEK substrates in order to determine their surface chemistries. Due to the charging effect during the measurements, shifting of the measurements was corrected to the standard C1s peak. As can be seen in Figure 3.33, PEEK substrates have the same characteristic after the deposition of ultra-thin alumina layer. C1s peak may be the result of the carbon contamination on the surface due to its less than 5% in total amount. In order to understand the binding of aluminum with oxygen at 2p orbital, detailed analyzing was done between the binding energies of 70 eV and 80 eV and presented for all types of substrates in Figure 3.34. Central peaks for the surfaces *NT-PLD*, *LT-PLD*, *PT-PLD* and *PLT-PLD* were found at 74.6 eV, 74.8 eV, 74.6 eV and 74.3 eV respectively.
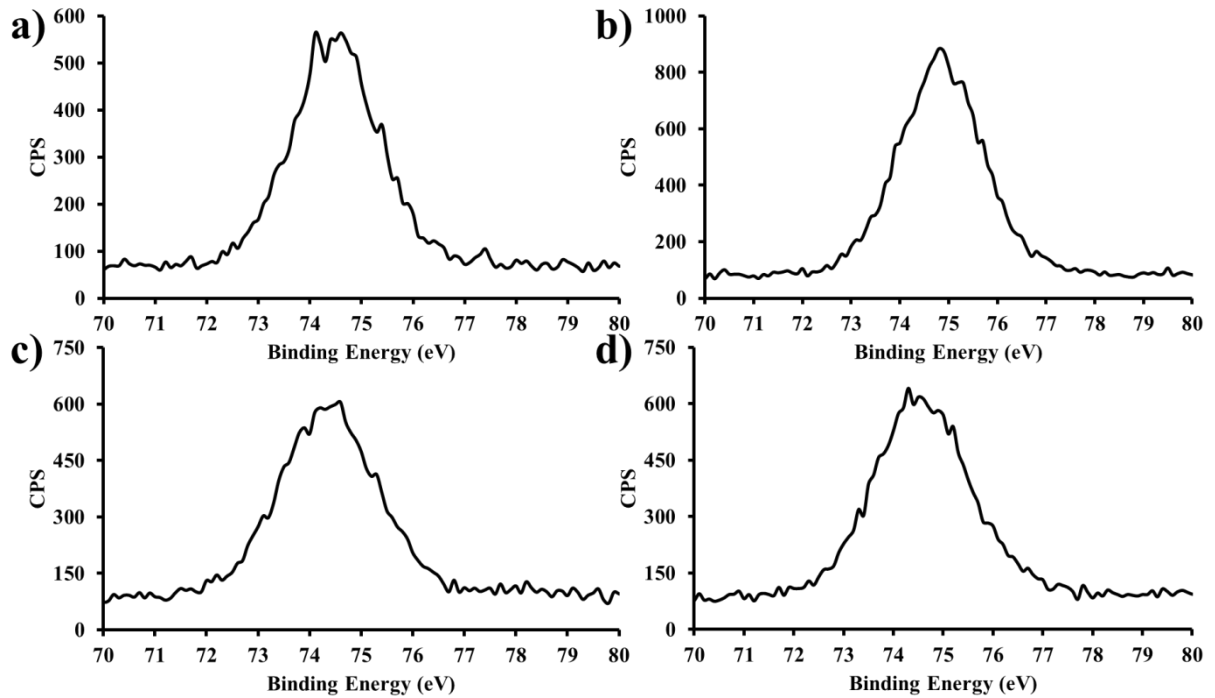
Figure 3.34: XPS analyzes of PEEK substrates for Al2p orbital a) *NT-PLD*, b) *LT-PLD*, c) *PT-PLD*, d) *PLT-PLD*.

3.4.2 Roughness Measurements of Alumina Deposited PEEK and Alumina Substrates

Roughness measurements were performed with AFM as mentioned previously. In order to see the effect of deposited alumina layer on PEEK substrates, they compared with their non-coated ones. AFM images of PEEK surfaces are given in Figure 3.35. Similarly, roughness values of the alumina substrates; which are, non-treated alumina plate (*NT-Al*), non-treated Al/Al$_2$O$_3$ NWs (*NT-NWs*), and laser treated Al/Al$_2$O$_3$ NWs (*LT-NWs*) were measured with

AFM and represented in Figure 3.36. Unfortunately, AFM measurement of the laser treated alumina plate (*LT-Al*) surface is not possible to measure the roughness data because of the unordinary optical reflections from the surface. As known, while operating the AFM, operator needs assistance of an optical view supported by a camera. However, unordinary surface reflections make the camera blind to the laser structures at the surface. In order to find an approximate roughness data for *LT-Al* substrate, SEM image of the corresponding surface was analyzed by open source software "Gwyddion". Gwyddion is mostly used for further data analyses of the collected AFM data. The logic behind this approximation is: if the highest point of the surface is known, it may be possible to make an approximation for roughness data from a SEM image over contrast. In order to make an approximation for this, known height value of *NT-Al* was used to determine the roughness value *LT-Al*. For this, whitelight interferometer data was used to find the highest point and when this point is inserted into the software, the approximate roughness value was defined. Calculation was controlled with the *NT-Al* substrate with the same method for its reliability. Result is given in Figure 3.36 and indicated with star (*). As a survey, roughness values of the all surfaces are given in Table 3.5.
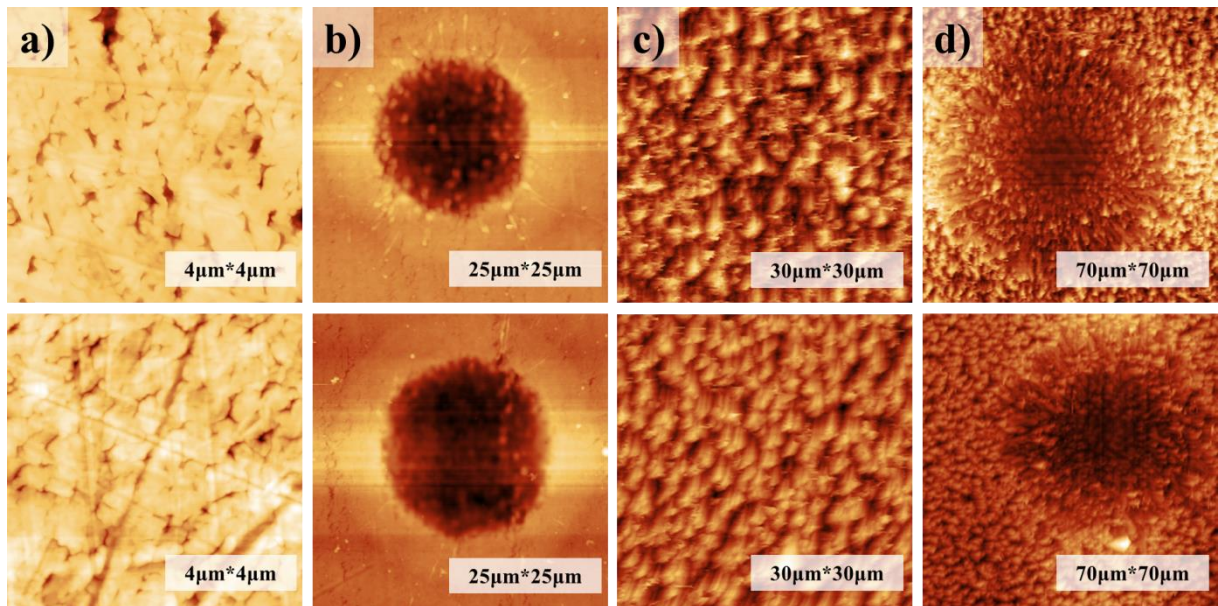
Figure 3.35: AFM topographies of laser and plasma treated samples. a) NT, b) LT, c) PT and d) PLT. Upper images are the non-deposited substrates while the lowers are the deposited ones.
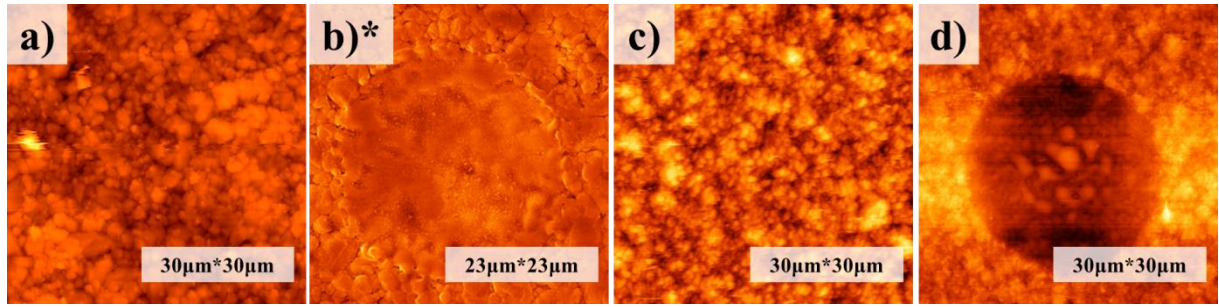
Figure 3.36: AFM images of a) NT alumina plate, b) LT alumina plate*, c) NT NWs and d) LT NWs. *: From SEM image for approximation.

Table 3.5: Roughness Values (R_a) of prepared substrates by AFM. *: Approximation from SEM image.

Deposited PEEK	NT-PLD	LT-PLD	PT-PLD	PLT-PLD
R_a Values (nm)	6.1	108.4	723	1000
Non-Deposited PEEK	NT	LT	PT	PLT
R_a Values (nm)	9	93	736	1065
Alumina Subs.	NT Alumina	LT Alumina*	NT NWs	LT NWs
R_a Values (nm)	111	130*	167	323

3.5   Contact Angle Measurements

Static contact angles of the prepared surfaces were measured and surface energies were calculated from the equation 18. Captured photos of the water drops on the surfaces of all substrates are presented in Figure 3.37 and 3.38. Measurement results are given in Figure 3.39 with the corresponding surface energies. As can be seen from the Figure 3.37, however their contact angles are tending to increase, alumina substrates are stable in their wettability for long term. When the alumina coated PEEK substrates are investigated (Figure 3.38), it is clear that the contact angles are increasing day by day but still much lower than the contact angle of non-coated PEEK which is around 87˚. Furthermore, previously plasma treated substrates (*PT-PLD* and *PLT-PLD*) show super hydrophilic behavior at the beginning and tending to increase with in the following days. Besides, it is clear that the *PLT-PLD* surface remains its hydrophilic behavior longer than the *PT-PLT* surface. For comparison of the substrates for their wettability, contact angles versus to days are given in Figure 3.39-a and –b.
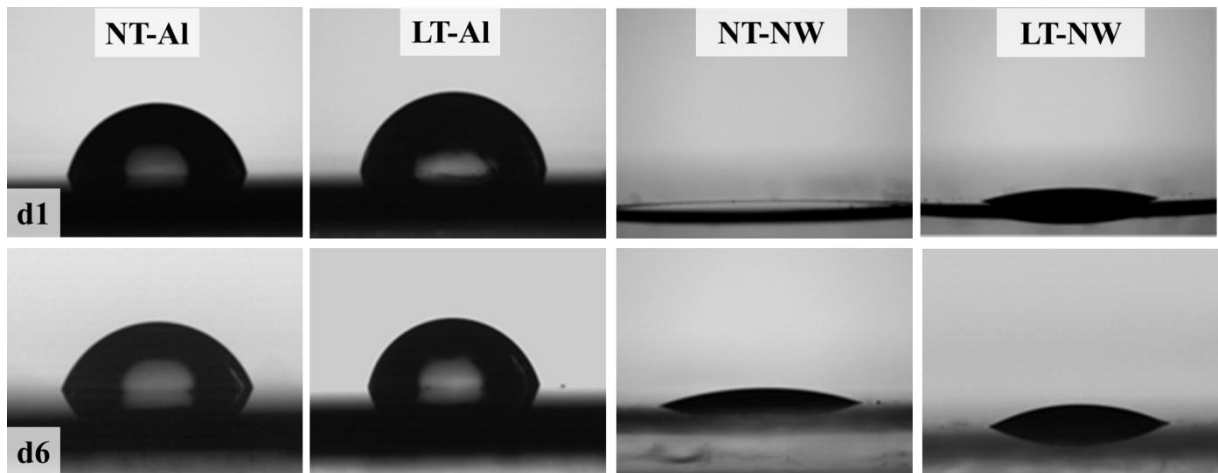
Figure 3.37: Captured water photos of *NT-Al*, *LT-Al*, *NT-NW* and *LT-NW* on the 1st and the 6th day after the substrates prepared. Photos are limited with these days due to the similar results.

As can be seen there, contact angle values of *NT-Al* and *LT-Al* surfaces vary around an average value. Thus the static contact angle of these surfaces can be considered stable at their average values. On the other hand, alumina coated PEEK substrates in the same comparison show more hydrophilic behavior than the others. Furthermore, if the *NT-PLD* and *LT-PLD* substrates are compared to each other, *LT-PLD* shows better wettability than *NT-PLD*. It may be right to mention about a Wenzel state here for *LT-PLD* substrates. When the surfaces only with NWs are investigated, it can be clearly seen from the curves, *PLT-PLD* surface shows long term
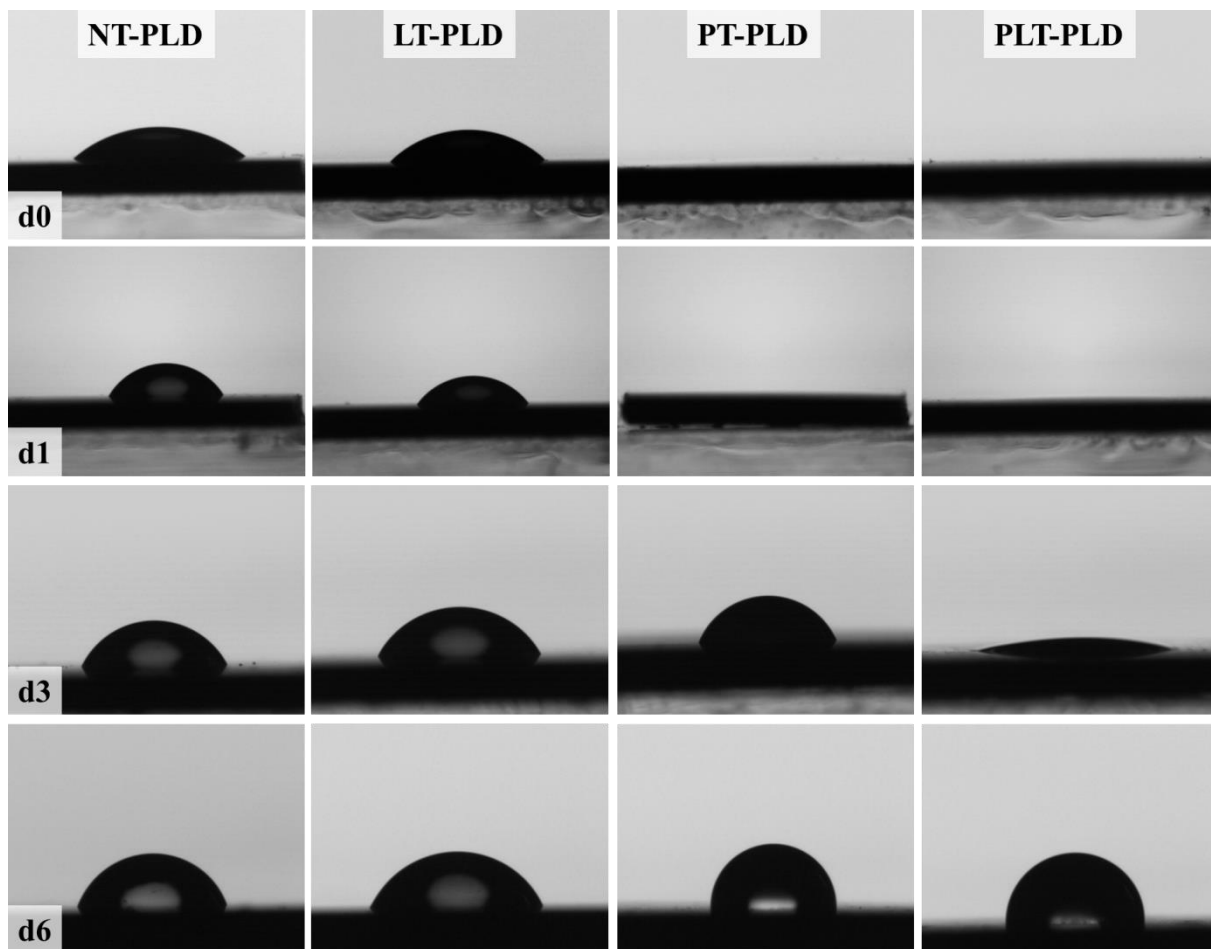
Figure 3.38: Captured water photos of alumina/PEEK substrates *NT-PLD*, *LT-PLD*, *PT-PLD* and *PLT-PLD*.

stability for the wetting properties while the *PT-PLD* surface starts to increase its contact angles after the 3rd day. On the other hand, when the first three days are examined, it must be noticed that the alumina coated PEEK NWs show more hydrophilic than the others where the contact angles for these substrates shows zero degree. These properties indicate super hydrophilic behavior. However after the 3rd day, these structures recover their hydrophobic behaviors and increase their contact angle.

a)

Comparison of Macro Surfaces

b)

Comparison of Nano Surfaces
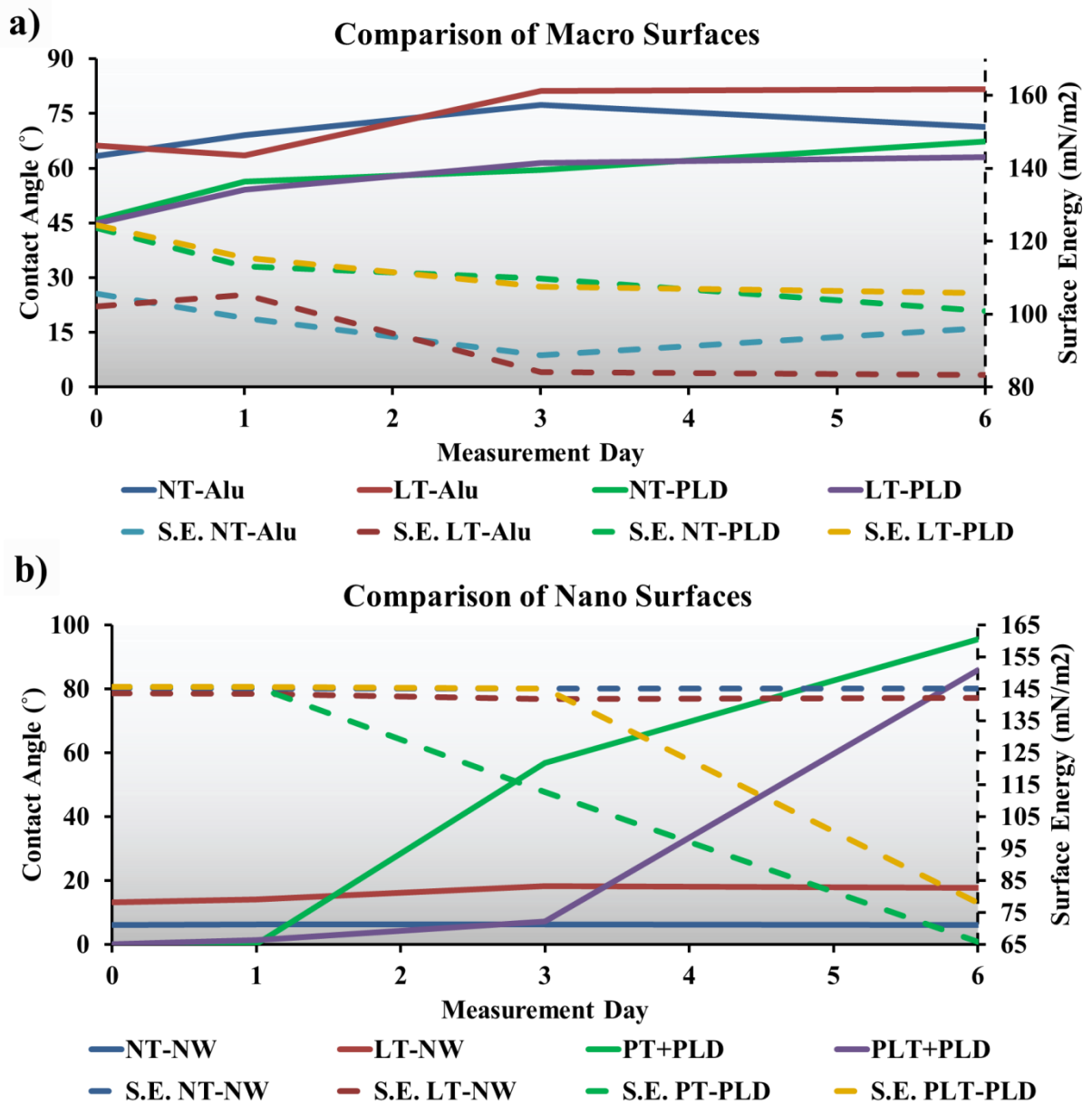
Figure 3.39: Contact angle comparisons between a) surfaces without NWs over. It can be seen that the alumina coated PEEK substrates show more hydrophilic for the measurement time. b) Surface with NWs over. It is clear that the Al/Al$_2$O$_3$ core/shell NW surfaces remain their wettability with in the time while the alumina coated PEEK NWs suffer from the hydrophobic recovery at the same time scale. Additional to the contact angles, surface energies of the substrates are given at the same graphs.

3.6 HUVEC Reaction to the Alumina and Alumina coated PEEK Substrates

3.6.1 HUVEC Morphology on NWs and Alumina Plate
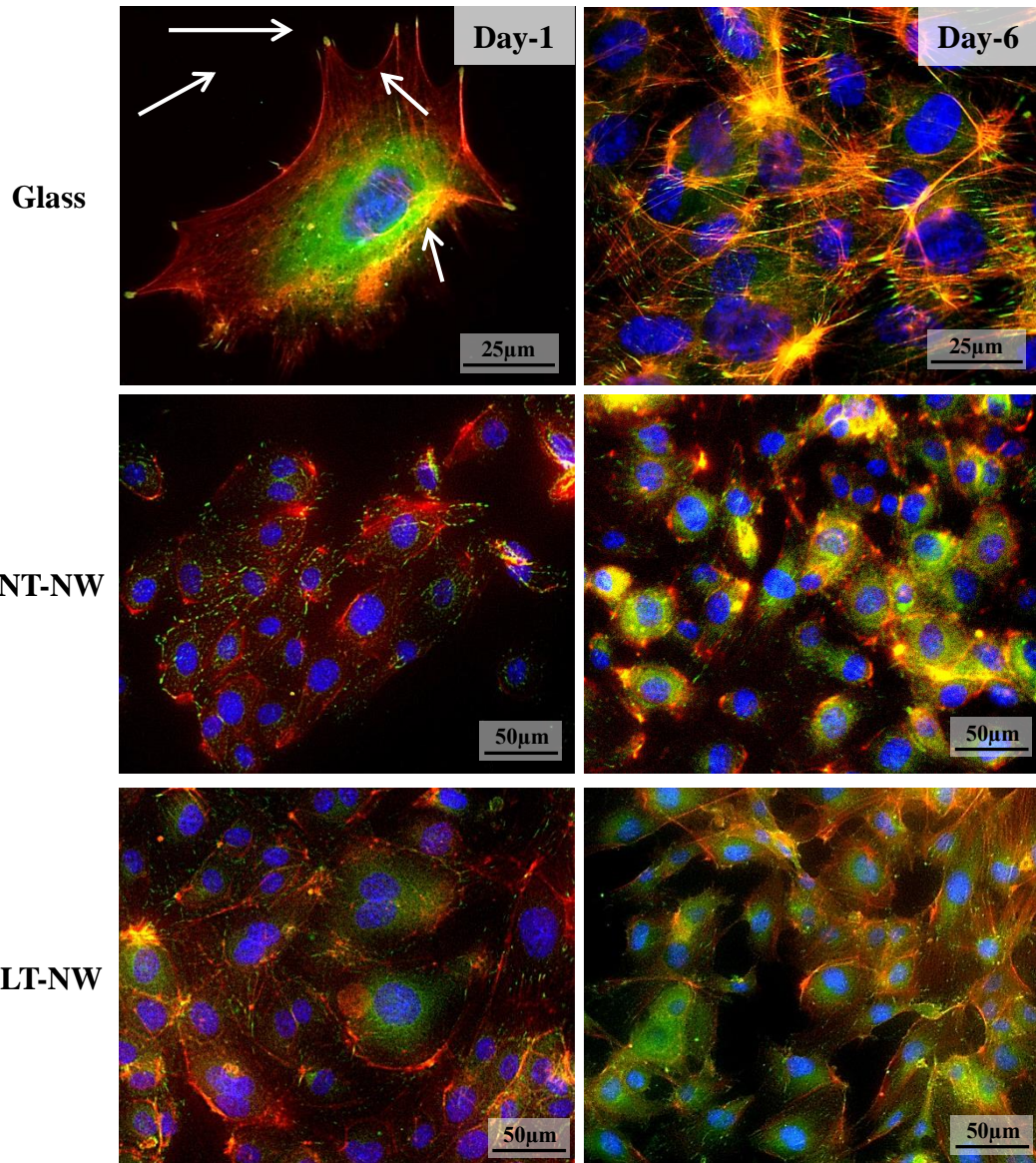
Figure 3.40: Fluorescence microscope images of HUVEC on glass, *NT-NW*, *LT-NW* substrates for their morphology.

As it can be seen in Figure 3.40, HUVECs exhibit a regular and normal morphology on glass substrate which is used as control. It can be seen there how the cells spread normally in a laminar shape which proved by the presence of the lammilopodia formation labelled by the white arrows as well as the high amount of focal adhesion which are indicating the effective

adhesion of the cells on these control surfaces (visualized by green spots). In contrast, on NWs surfaces the cells behave differently. It can be still observed there that there is a high amount of cells on the surface but these cells have different shapes characterized by a smaller surface area. Formation of F-actin in bundles can be seen clearly where they are indicating the applied stress on cells from the environment (Figure 3.40, *NT-NW_* day 1). In order to survive, cells strengthen their cytoskeleton by forming these bundles as a response to the applied stress, thus, they are reducing their sizes and try to form a sort of colonies with other joint cells. These colonies indicate the non-healthy way of connection between cells, therefore, it is believed that a normal tissue cannot be built in this case (Figure 3.40, *NT-NW_* day 6). Additionally, it is clearly observed that the number of focal adhesion points is very less which indicates that cells adhesion on the NWs surface are not good. On the other hand, cells on laser structured NWs show almost similar behaviour as observed on control substrates (Figure 3.40, *LT-NW_* day 1). Cells spread well in a normal form and are connected between each other with a good form which can lead to the formation of a normal tissue afterwards. Adhesion is also improved in these surfaces which can be shown by the high concentration of the focal adhesion points (Figure 3.40, *LT-NW_* day 6)
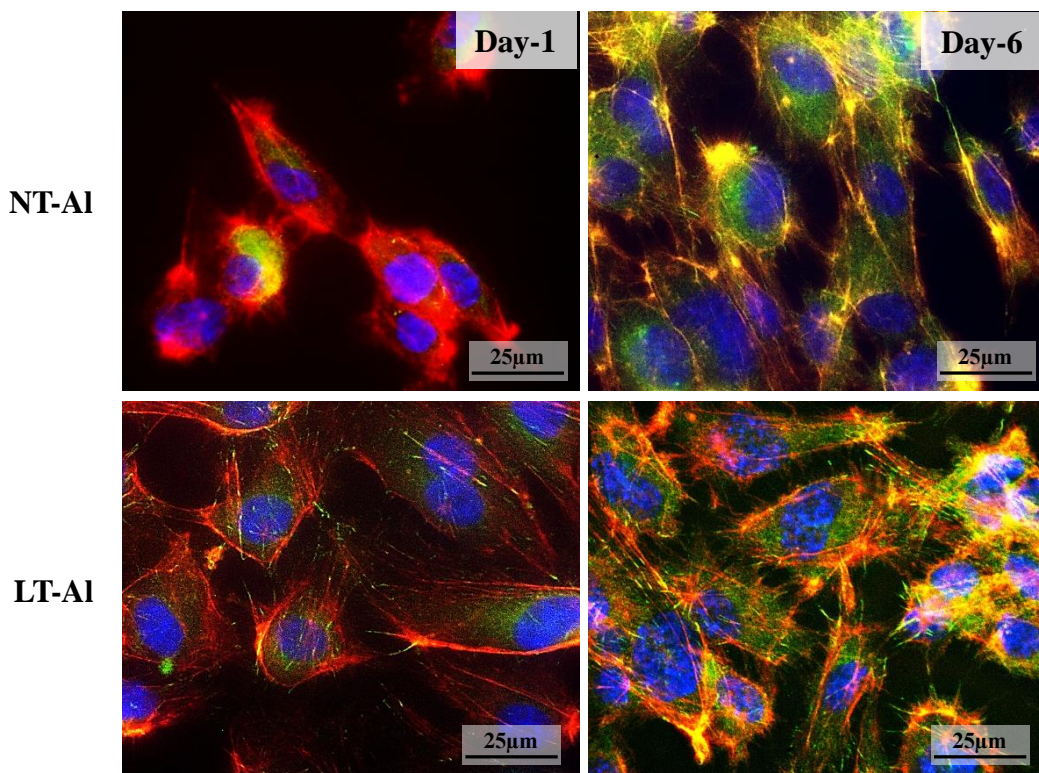
Figure 3.41: Fluorescence microscope images of HUVEC on *NT-Al* and *LT-Al* substrates for their morphology.

On *NT-Al*, normal behaviour of the cells with quite reduced surface areas can be seen (Figure 3.41, *NT-Al_* day 1). However, the adhesion on these surfaces seems to be better with the following time (Figure 3.41, NT-Al_ day 6). On the other hand, cells show better result on *LT-Al* surfaces which can be understood from the well spread cell bodies (Figure 3.41, *LT-Al_* day 1). It was observed for the day 6, cells were spread normally and adhered well to the surface. Such adhesion and growth regime can build a healthy tissue.

3.6.2 Metabolic Activity of HUVEC on Alumina and Alumina Coated PEEK Substrates

As it mentioned previously, metabolic activity of the HUVECs on different surface types were tested with WST-1 assay. Collected data are given in Figure 3.42-a for alumina surfaces and in Figure 3.42-b for alumina coated PEEK surfaces. As first general observation of the obtained results, all the surfaces are tending to increase the cell proliferation percentages in comparison to the positive control, while cells on the non-treated PEEK surfaces show almost similar percentage of metabolic activity at each day point.

Alumina substrates are observed in figure 3.42-a where it is clear that the proliferation rate for the early period of NW surfaces is higher than that the observed on planar alumina plates which indicate an enhanced HUVEC proliferation on nano features. Furthermore, when the *LT-NW* surface compared to the *NT-NW*, there is a clear increasing in proliferation rate of *LT-NWs*. Similar result can be seen for the *NT-Al* and *LT-Al* surfaces too. When the WST-1 assay was applied for the 3rd and the 6th days, it is clear that cell proliferation rates increase exponentially for all types of the alumina surfaces. On the 6th day, effect of the periodic laser micro structures can be seen much clear. These structures enhance the proliferation rate for both NWs (~3.7 times more than positive control) and alumina plates (~3.4 times more than positive control). This result indicates that, laser surface structuring with periodic micro features enhances the HUVEC proliferation on alumina surface. On the other hand, combination of micro structures with nano features enhances the HUVEC proliferation much better than micro structures alone.
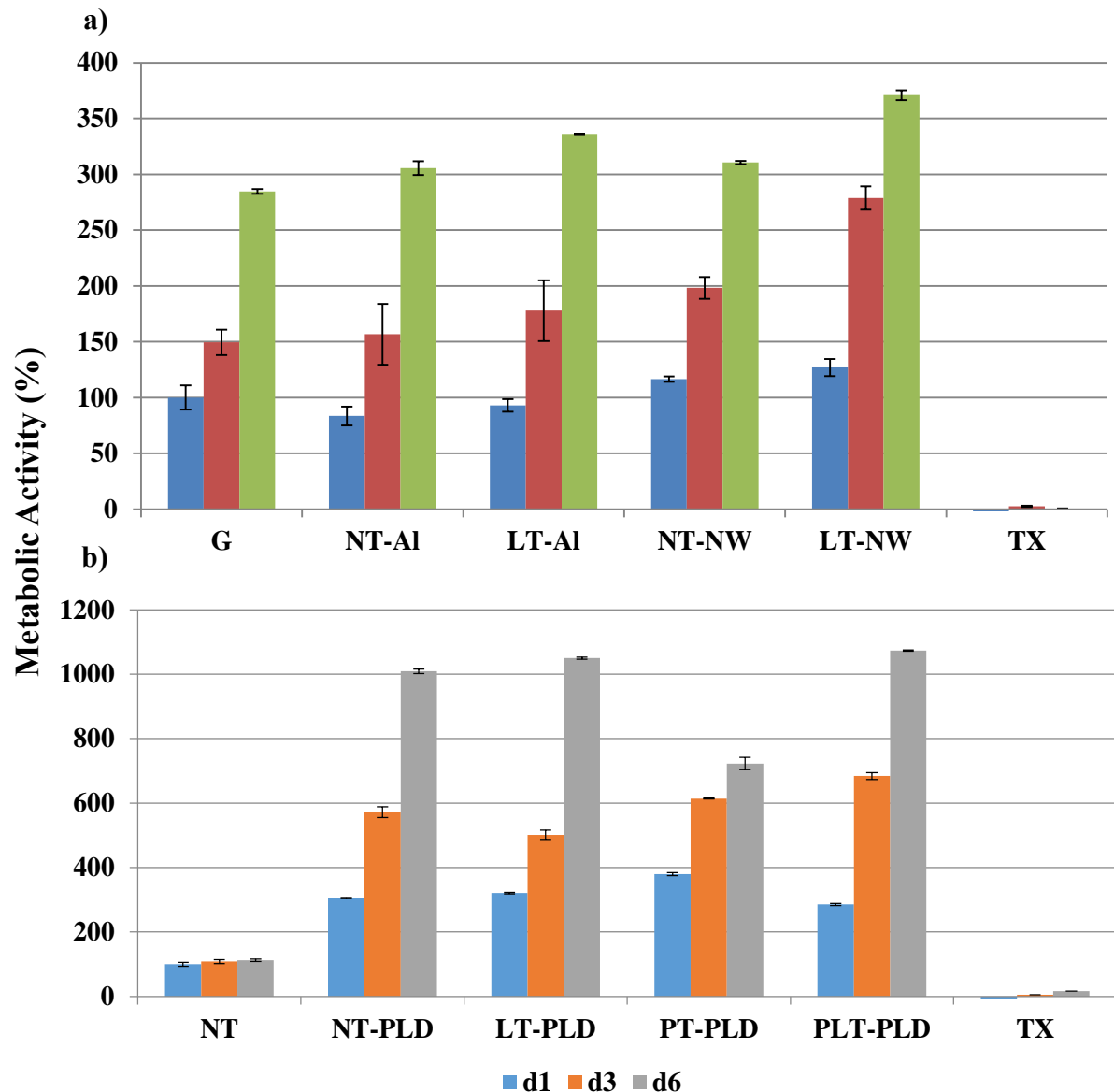
Figure 3.42: WST-1 assay for determination of HUVEC proliferation rate on a) alumina surface and b) alumina coated PEEK surfaces.

Metabolic activity of the HUVECs on alumina coated PEEK surfaces are presented in Figure 3.42-b which are indicating the similar result with alumina surface types. It is clear that the proliferation rates are increasing exponentially for all alumina coated PEEK substrates with the following days. For the early period of the WST-1 assay, cell proliferation rates are similar for *NT-PLD* and *LT-PLD* and these surfaces continue to raise their proliferation rates parallel till the late periods of the assay. When nanostructured alumina coated PEEK surfaces are examined, it was observed that the proliferation rate of *PT-PLD* for the first day shows better result in comparison to *PLT-PLD*. However, results for the 3rd day indicate that the combination

of NWs with periodic microstructures support better condition for the HUVEC proliferation. Proliferation rates for the *PLT-PLD* substrates reach to their higher value on the 6th day and exponential increment of this surface type shows similar result to its comparable alumina surface (*LT-NW*). In order to see the effect of deposited alumina layer on PEEK surface types, same experiment was applied to *NT* PEEK substrate. It can be clearly seen that the cells proliferation is same for each day point on *NT* PEEK surfaces which indicates that the bulk PEEK surface is not an optimal environment for cells proliferation. On the other hand, the introduction of ultra-thin alumina layer on PEEK enhances the HUVEC proliferation rate 10 times in comparison to non-coated one.

As it mentioned previously, alumina coated PEEK substrates were produced to create similar and comparable surfaces with the alumina substrates where alumina plates are commercially available and Al/Al$_2$O$_3$ core/shell NWs were produced by Veith et al.. In order to understand their similarities, comparison calculation was performed between the following groups: *NT-Al* to *NT-PLD, LT-Al* to *LT-PLD, NT-NW* to *PT-PLD* and *LT-NW* to *PLT-PLD* in the meaning of tendencies. Calculations are based on angular differences between the linear trendlines of each surface type proliferation rates. Trendlines with their equations are given in Figure 3.43.

In order to calculate the differences of each comparable surface type, slope of the trendlines were collected from the calculated equations and they were sorted in their selves. From these slope values, the angular differences between the comparable groups were calculated by using the equation 31:

$$\tan \theta = \frac{m_1 - m_2}{1 + m_1 m_2} \tag{31}$$

Results are given in Table 3.6. In order to make a relation between the calculated angle values and the differences between the comparable surfaces, a simple logic was followed and can be explained as: if the angle between the trendlines is 0°, this indicates 100% similarity and if the angle between the trendlines is 90°, this indicates 0% similarity. With this acceptance, the similarities between the comparable surfaces were calculated and given in Table 3.6. As can be seen from the results, comparable surfaces are highly similar which means that the alumina deposition with PLD technique over planar, laser treated, plasma treated and combined plasma and laser treated PEEK surfaces are acting like alumina surfaces. On the other hand, substrates *PT-PLD* and *PLT-PLD* can be alternative surface structures where the Al/Al$_2$O$_3$ core/shell NWs cannot be applied on materials, such as low melting temperature polymers.
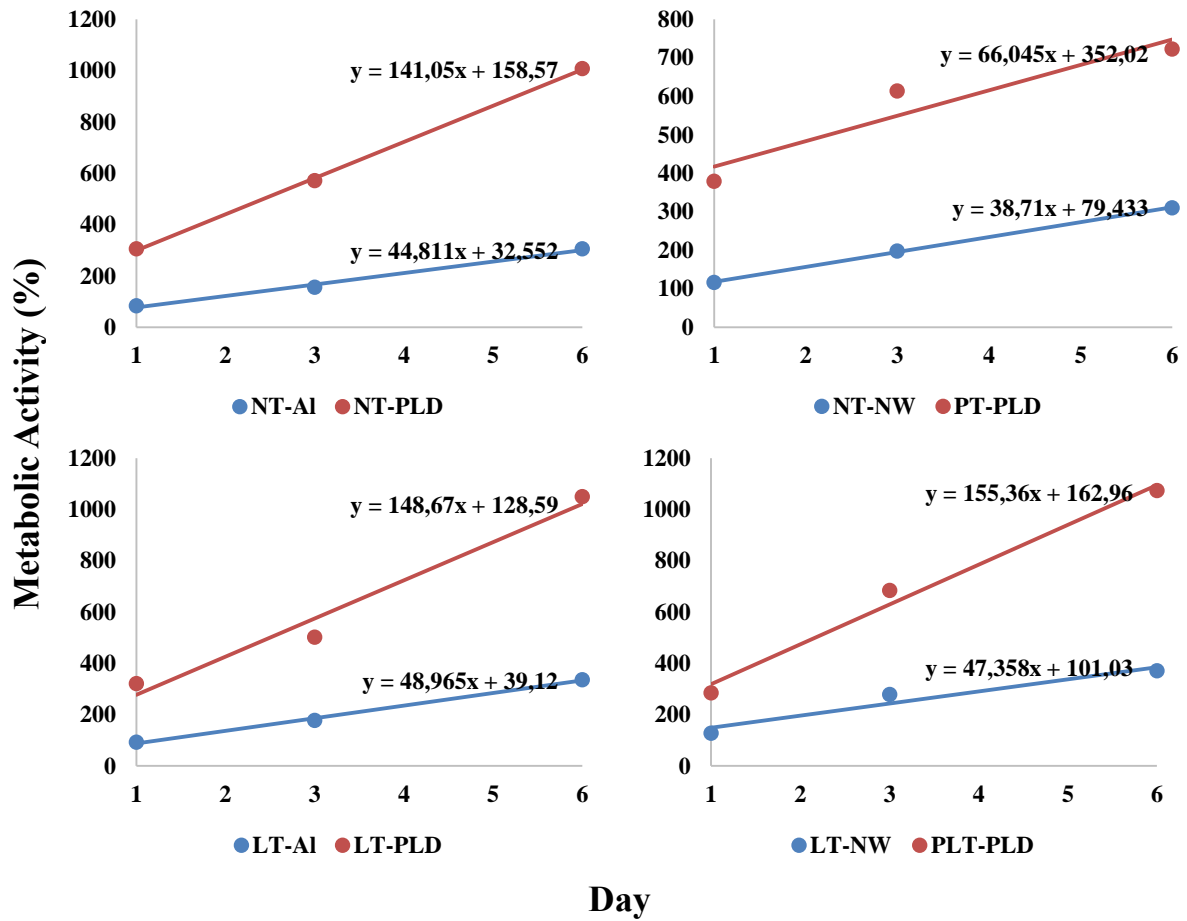
Figure 3.43: Proliferation rate versus to incubation time (day 1-3-6) distribution for the similarity calculation. Calculations had been done via using the linear trendlines of each surface type in comparable groups. Parallel trendlines shows 100% similarity while vertical trendlines show 0% similarity.

Table 3.6: Slope of the trendlines for the prepared surfaces for their similarity comparison.

Compared Surfaces		NT-Al & NT-PLD		NT-NW & PT-PLD		LT-Al & LT-PLD		LT-NW & PLT-PLD	
Slope 1	Slope 2	141.05	44.81	66.05	38.71	148.67	48.97	155.36	47.358
Calculated Angle (°)		0.87		0.61		0.78		0.84	
Similarity Percentage (%)		99.03		99.32		99.13		99.07	

4   DISCUSSION and CONCLUSION

In this thesis, different but chemically identical PEEK substrates were investigated and tested for their behavior to the HUVECs. Additionally, they compared to another medical grade implant material "Alumina" which was structured and generated with different surface topographies in terms of micro and nano scales. During the surface modifications, plasma etching and laser surface structuring techniques were applied to the necessary substrates separately or either following to each other (hierarchical surface structuring)

In order to support alumina surface, commercially available alumina plates were used as planar surfaces and Al/Al_2O_3 core/shell NWs, which were deposited by CVD technique over glass substrates as Veith et al. suggested previously, were used as nano scaled surface structures (Aktas OC 2009; Veith et al. 1996b; Veith et al. 2010a; Veith et al. 2012). Laser surface modification technique by using microlens array was carried out on these surfaces with 3rd harmonic of Nd:YAG laser and four different alumina surface types, *NT-Al*, *LT-Al*, *NT-NW* and *LT-NW* were prepared . During these processes, a new optical system was designed with single lens system which provided the same conditions with microlens array and performed successfully where this setup was founded necessary to protect the microlens array from back sputtering of the material due to its short focal length. Amount of the substrates for the biological experiments forced the experimental procedure to change in this way. Additional to these works, laser ablation rate and effect of laser pulse energy and pulse number on alumina plates were measured and calculated for different environments such as: air, vacuum and argon gas flow conditions. From the performed experiments, air and argon environments were found similar for the material processing however the vacuum condition showed different behavior. Similar results for laser drilling of alumina were observed previously by Mutlu et al. (Mutlu et al. 2009). They pointed out there the depths of the structures on alumina are decreasing when the ambient pressure starts to decrease from atmosphere pressure. On the other hand, depth of the structures starts to increase again when the vacuum level reaches to a certain value. This phenomenon can be a reason of the observed ablation rate differences during the performed experimental work. Additionally, during the laser modification of alumina plates, it was observed that the surface topography has high influence on the laser processing where the unordinary surface structures may cause variance on the result. For the laser structuring of Al/Al_2O_3 core/shell NWs, similar procedure was followed. However, due to their relatively low deposition thickness (around 750nm), treatments were found limited with single laser pulse at

7.5mJ. When the second laser pulse was tried on the same location, it was observed that the deposited layer is getting ablated completely from the surface.

In order to produce comparable micro surface structures on PEEK substrates same method was applied to the PEEK surfaces. In this context, laser parameter effect on PEEK polymer was investigated, such as ablation rate, structure depth and crated diameter. It was observed that the laser ablation rate for PEEK substrate is almost independent from applied atmospheres unlike alumina plates where it shows different behavior under vacuum condition while air and argon conditions show similar results and depth and crater diameter distributions follows the applied laser pulse energies. Similarly, Riveiro et al. investigated the effect of Nd:YAG laser wavelength on PEEK surface (Riveiroa et al. 2012). As can be seen there; and as observed from our previous experiences also, 355 nm wavelength, which corresponds to UV light source, gives the optimum surface structures (smoother structures).

One of the favorite plasma surface modification technique; which is plasma etching with oxygen etchant gas, was applied to perform NWs over PEEK surfaces where this method was used to generate comparable surface to the Al/Al_2O_3 core/shell NWs . In this content, effects of oxygen gas flow and applied RF power on PEEK substrates were investigated. It was observed that length of the produced fibers are increasing linearly when gas flow and RF powers increase. However, variation can be seen at the results where the semi crystalline structure of PEEK may lead such differentiations (Fridman A 2008). Tsougeni et al. pointed out similar results for the growth rate of NWs from the PEEK and PMMA materials under different oxygen gas flows (Tsougeni et al. 2009). On the other hand, it is known that surface chemistry cannot be as the same like bulk PEEK substrates after the laser and plasma treatments. Oxygen plasma etching of polymers; due to the mechanism of etching process, forms oxygen containing groups on the surfaces such as: -C=O, -C(R)-O-H and -C(R)-O-O-H (Fridman A 2008). As shown by Ha et al., new functional groups (carboxylade (COOH) and carbonate (CO_3^{2-})) are forming on PEEK surfaces after the oxygen plasma etching process additional to the increased ratio of oxygen bonds and reduced carbon bonds (Ha et al. 1997). As it shown before at the XPS analysis of plasma treated PEEK by mixed argon and oxygen gases, it is clear that percentage of the C-C single bonds are decreasing while the percentage of the C-O single bonds and C=O double bonds are increasing in comparison to the bulk non-treated PEEK surfaces (Akkan et al. 2013a). Besides, there must be a changing at the chemical state of the PEEK surfaces after laser treatment too. As Akkan et al. indicated previously, 355nm wavelength laser treatment causes an increasing at the oxygen bonds on non-treated PEEK surface. On the other hand, however it

is decreasing after laser treatment, previously plasma treated PEEK substrates show still higher percentages of carbon and oxygen bonds (Akkan et al. 2013a). Another laser modification study on PEEK was performed by Laurens et al.. They observed that the UV laser treatment causes a clear increasing of the O/C ration at the PEEK surface in air environment (Laurens et al. 1999; 2000). Similar study was performed on PMMA surface by Lawrence and Li by several laser sources. They observed that the oxygen ratio is increasing on the PMMA surface after the treatment by Excimer Laser (KrF-248nm) (Lawrence et al. 2001).

With the defined plasma and laser processing parameters, alumina substrates treated with laser and PEEK substrates were etched and treated by plasma and laser techniques respectively. It is possible to skip the chemical analysis of laser treated alumina plates and the Al/Al$_2$O$_3$ core/shell NWs surface by XPS were skipped due to their well-known stable chemical properties even after laser treatment. As shown by Kim et al. previously, alumina preserves its surface chemistry even after the laser treatment (Kim et al. 2009). Similarly, as shown by several authors, Al/Al$_2$O$_3$ core/shell NWs remains their α-alumina state after the laser treatments (Veith et al 2012; Veith et al .2010b; Aktas OC 2009, Lee et al. 2013).However the PEEK substrates were prepared for their surface topographies, their surface chemistries are in different states as mentioned above and they all have to be stabilized in order to understand the clear effects of the surface topography on cells at the further experiments. In this context, ultra-thin alumina layers (~ 10 nm) were deposited on PEEK substrates by PLD from 99.99% pure α-alumina target. Additionally, by applying this process, structured PEEK surfaces were transformed to a state that they can be comparable with the alumina substrates. Although there are several methods such as CVD and PVD, they are not suitable to deposit alumina layer on polymeric substrate. As known, CVD technique requires high surface temperature to deposit alumina layer on substrate which is not suitable for polymeric materials in most of the cases. PVD is another method to deposit homogeneous layers however, limitations at the stoichiometric deposition opportunity makes this method useless to sputter α-alumina (Lieberman et al. 2005). Atomic layer deposition (ALD) is also another promising method for the thin film applications. It was shown by Peng et al., alumina layers were successfully deposited over polymer nano fibers (Peng et al. 2007). However we found PLD technique easy to sputter alumina layers on PEEK surfaces where the stoichiometry of the target material can be transferred to the substrate surface without any doubt while providing ultra-thin and thickness controllable layers. In this content, homogeneous and topography following coatings were performed successfully and deposition parameters related to the deposition time and laser pulse energy were investigated simultaneously. Additionally, surface chemistries were found

identical at XPS analysis for all PEEK surfaces after deposition (Figure 3.33 and 3.34) and these results were found identical with the observations of Kim et al. and Yang et al (Kim et al. 1994;Yang et al. 2000).

As a counter discussion to the benefits of PLD, this deposition method may causes surface defects or film defects as characteristic results. Some hillock formations for $Fe_{81}B_{13.5}Si_{3.5}Co_2$ over silicon wafer was reported by Mróz et al. previously (Doughty et al. 1995; Eason R 2007; Carradò et al. 2011; Marcu et al. 2000, Mróz et al. 2008). Droplets are the particles that they can be located at the surface of the grown film or can be embedded inside the film. They usually have sizes between 100 nm and 3 μm and they are the most common defects observed in PLD. Besides, grains with sizes larger than 10μm can be seen due to the direct material ejection from the target (Doughty et al. 1995). At Figure 3.27-a, -b, -c and -e some droplets can be seen as expected. Their sizes are measured with whitelight interferometer (Figure 3.24 and 3.25) and detected as smaller than 1μm in diameter with height of between 50 nm to 100 nm. Similar structures were reported by J.E. Villarreal-Barajas et al. previously (Villarreal-Barajas et al. 2002).
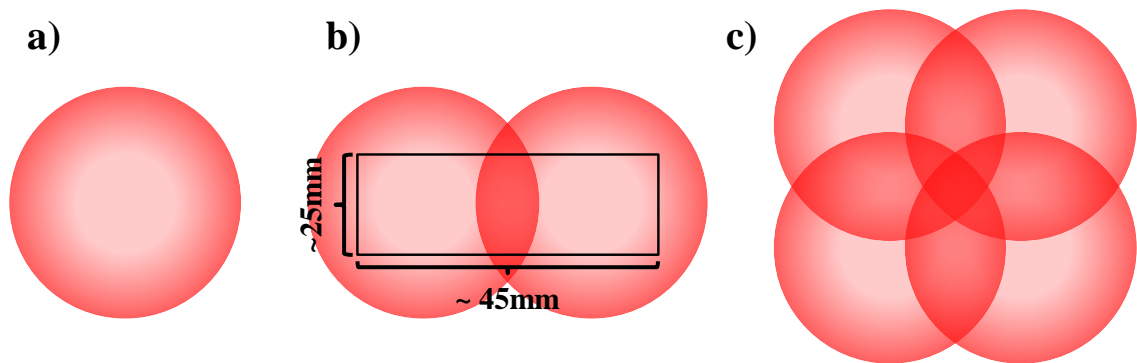
Figure 4.1: Homogeneity definition for all described deposition techniques: a) single beam PLD, b) double beam PLD and c) basic illustration of Matrix Shaped PLD.

During the determination of the PLD process parameters, three different deposition techniques were applied to perform better homogeneous coatings and in order to support this, three different optical setups were realized (Figure 2.7). It is observed that the double beam deposition technique supports better linear homogeneity at single direction while single beam deposition technique supports less homogeneous area. Additional to the single and double beam deposition techniques, completely new deposition technique which is named as "Matrix Shaped Pulsed Laser Deposition" (MS-PDL) was suggested and performed successfully in this thesis. This process provides better homogeneous layers on the substrates surfaces in two directions

due to its matrix laser beam distribution (Figure 4.1) (Akkan et al. 2013b). However, as far as this technique is a new method, it has to be improved in its optical system setup and intensity distribution on the target surface in order to obtain highly homogeneous layer distribution on substrate surface. Therefore, during the PLD works, double beam deposition technique was selected to coat the PEEK surfaces because of its more plateaus like coating distribution in single axis. This homogeneous plateau like area can be seen in Figure 4.1-b. Additionally, mentioned homogeneous area of the double beam process can be improved via changing the location of the laser beams on the target surface and can rise up to 70 to 80 mm in single axis.

As it mentioned above, water contact angles of the substrate surfaces were measured where the surface wettability has high correlation for the cell adhesion and spreading (Ratner et al. 1996; Liang et al. 2005). Therefore, surface contact angles were measured for the 1st, 3rd and the 6th day additional to the substrate preparation day. It was observed from alumina surface that these surfaces remain their hydrophilic behavior for long term although there is a relatively small increasing at the contact angle of *NT-NW* and *LT-NW* surfaces. When the alumina coated PEEK surfaces were examined, it was observed that these surfaces show hydrophilic behavior similar to the alumina substrates. As can be seen there, PEEK surfaces with NWs (*PT-PLD* and *PLT-PLD*) show extremely hydrophilic behavior in comparison to *NT-PLD* and *LT-PLD* surface. Here the effect of the surface roughness can be seen clearly as Wenzel suggested (Wenzel RN 1936). Although these surfaces show hydrophilic behavior, they suffer from the hydrophobic recovery with in the following time. In most of the conditions, reorientation of the polar groups after treatment, condensation of the hydroxyl groups at the surface and possible surface cracks on the deposited layer may cause hydrophobic recovery at the substrates surfaces (Tsougeni et al. 2009; Spagnola et al. 2010; Kim et al. 2001). Kobayashi et al. were observed that the alumina coating on organic surface by ALD technique decreases the water contact angle when the thickness of the coated layer increases. However, after certain amount of time, these layers start to lose their hydrophilic properties (Kobayashi et al. 2007). This may be the reason of the formation of hydroxyl groups on alumina surface as mentioned. Takeda et al. pointed out that the metal oxides may suffer from hydrophobic recovery with in the time due to increased OH density on the surface (Takeda et al. 2005). Similar result was shown before by Finch et al.. He pointed out that the increasing at the surface hydroxyl groups can cause increment at water contact angle (Finch et al. 2008). However, as can be seen from the Figure 3.38 and 3.39, *PLT-PLD* surface remains its hydrophilic behavior longer than the *PT-PLD* surface for the first three day. This can be the reason of the decreased surface area after the laser treatment where the concentration of the OH groups on *PLT-PLD* surface is less than the *PT-PLD* surface. Same

expectation is also applicable to the *NT-PLD* and *LT-PLD* surface additional to the comparison of *LT-NW* to the other alumina surfaces where the less rough surfaces show longer hydrophilic behavior

Since the alumina and PEEK are the biomedical implant materials, their behavior to the HUVECs were examined over the prepared alumina and alumina coated PEEK substrates. Since the PEEK known as autofluorescent, only the alumina substrates were analyzed with fluorescence microscope (Althaus et al. 2012). Fluorescence microscopy images are indicating that the combined structures, where the laser treatment was performed over NW surfaces, shows better cell adhesion and spreading which may lead healthy tissue forming with in time. It was pointed out by several authors that oxygen containing surfaces enhance the cell proliferation and adhesion (Pashkuleva et al. 2010; Haa et al. 1997; Haidar et al. 2011; Dekker et al. 1992; Althaus et al. 2012). Since all the prepared surfaces have the oxygen containing material over their surface it was expected to see an increased proliferation rate for the cells. In this content, WST-1 assay which measures the metabolic activity of the cell on the surface was applied. This method supports the fluorescence microscopy results for the alumina substrates where the nano features in combination with periodic micro structures give highest proliferation rates for the HUVECs. When the HUVECs proliferation behavior was analyzed on alumina coated PEEK surfaces by the same method, surprisingly, similar proliferation rates were observed with in the each comparable group (*NT-Al* to *NT-PLD, LT-Al* to *LT-PLD, NT-NW* to *PT-PLD* and *LT-NW* to *PLT-PLD*). When the similarity percentages were calculated depending on their slopes for each surface (Figure 3.43), it was found that the comparable surfaces are similar to each other with a high ratio of 99% (Table 3.6).

However PEEK has a wide range of application field in medical implantology (such as: the total hip replacement, femoral stems, spinal implants, as bearing surface of hip and knee implants, stents to use for the esophagus and intestines and at the frame of the heart valves), it is clear that its surface modification has high importance for the success of the implant. Although its physical properties limit the modification methods, low temperature processing techniques can be an alternative way for necessary modifications. The present study shows that the laser and plasma surface modification techniques on PEEK substrates are a good candidate to the other modification techniques and present excellent results. Modifying the substrates surfaces without effecting the bulk propertied of the material is another benefit of the choosen treatment methods. Especially, stabilizing the surface chemistry by PLD technique eliminates the doubts in the terms of the cells reaction to the substrate surface while gives chance to deposit

any kind of materials to the PEEK surface which can be used for the other implanting fileds. Therefore, we hghly recommend the investigated methods for the PEEK implants since PEEK is a good candidate to alumina, titanium and its alloys for many application fields of the implant such as cardiovascular and orthopedic applications.

References

Abdel Ghany K, Newishy M (2005) Cutting of 1.2 mm thick austenitic stainless steel sheet using pulsed and CW Nd:YAG laser, J. mater. process. technol. 168: 438-447

Akkan CK, Hammadeh M, Brück S, Park HW, Veith M, Abdul-Khaliq H, Aktas C (2013a) Plasma and short pulse laser treatment of medical grade PEEK surfaces for controlled wetting, Mater. lett. 109: 261-264

Akkan CK, May A, Hammadeh M, Abdul-Khaliq H, Aktas OC (2013b) Matrix Shaped Pulsed Laser Deposition: New approach to Large Area and Homogeneous Deposition, Appl. surf. sci. Accepted Manuscript

Akkan ÇK (2009) Designing a Confocal Microscope for Researching the Biological Cells Interacted with Femtosecond Laser (Master Thesis), Kocaeli University, Kocaeli

Aktas C, Dörrschuck E, Schuh C, Miró MM, Lee J, Pütz N, Wennemuth G, Metzger W, Oberringer Mi, Veith M, Abdul-Khaliq H (2012) Micro- and nanostructured Al_2O_3 surfaces for controlled vascular endothelial and smooth muscle cell adhesion and proliferation, Mater. sci. eng. C 32: 1017-1024

Aktas OC (2009) Functional Applications of Al·Al2O3Nanowires: Laser Assisted α-Al2O3Synthesis and Fabrication of Micro-/Nanostructured Surfaces for Cell Compatibility Studies (Dissertation), Universität des Saarlandes, Saarbrücken

Aktas OC, Sander M, Miró MM, Lee J, Akkan CK, Smail H, Ott A, Veith M (2011) Enhanced fibroblast cell adhesion on Al/Al_2O_3 nanowires, Appl. surf. sci. 257: 3489-3494

Althaus J, Urwyler P, Padeste C, Heuberger R, Deyhle H, Schift H, Gobrecht J, Pieles U, Scharnweber D, Peters K, Müller B (2012) Micro- and nanostructured polymer substrates for biomedical applications, SPIE proc. 8339: 0Q

Babu SV, D'Couto GC, Egitto FD (1992) Excimer laser induced ablation of polyetheretherketone, polyimide, and polytetrafluoroethylene, J. appl. phys. 72: 692-698

Bajpai S, Jain M, Srivastava S, Balani K (2010) Pulsed Laser Deposition of Biocompatible Alumina-Hydroxyapatite (HA) Nanocomposite on 316L Steel, National Conference on Advancements and Futuristic Trends in Mechanical and Materials Engineering

Bäuerle D (1996) Laser Processing and Chemistry, Springer , Berlin: Heidelberg

Bäuerle D (2010) Laser chemical processing: an overview to the 30th anniversary, Appl. phys. A 101: 447-459

Bazaka K, Jacob MV, Crawford RJ, Ivanova EP (2011) Plasma-assisted surface modification of organic biopolymers to prevent bacterial attachment, Acta biomater. 7: 2015–2028

Bellan PM (2006) Fundamentals of Plasma Physics, Cambridge University Press, Cambridge

Bettinger CJ, Langer R, Borenstein JT (2009) Engineering Substrate Topography at the Micro- and Nanoscale to Control Cell Function, Angew. Chem. int ed Engl 48, 5406-5415

Biela SA, Su Y, Spatz JP, Kemkemer R (2009) Different sensitivity of human endothelial cells, smooth muscle cells and fibroblasts to topography in the nano–micro range, Acta biomater. 5: 2460-2466

Boumaza A, Favaro L, Lédion J, Sattonnay G, Brubach JB, Berthet P, Huntz AM, Roy P, Tétot R (2009) Transition alumina phases induced by heat treatment of boehmite: An X-ray diffraction and infrared spectroscopy study, J. solid state chem.182: 1171-1176

Cao G (2004) Nanostructures and nanomaterials: Systhesis, Properties and Applicaitons, Imperial College Press

Carradò A, Pelletier H, Roland T (eds) (2011) Nanocrystalline Thin Ceramic Films Synthesised by Pulsed Laser Deposition and Magnetron Sputtering on Metal Substrates for Medical Applications, Reza Fazel-Rezai (ed), Biomedical Engineering - From Theory to Applications, InTech , Croatia

Carradò A, Pelletier H, Sima F, Ristoscu C, Fabre A, Barrallier L, Mihailescu IN (2008) A perspective of pulsed laser deposition (PLD) in surface engineering: alumina coatings and substrates, Key eng. mater. 384: 185-212

Chapman B (1980) Glow Discharge Processes: Sputtering and Plasma Etching, John Wiley & Sons Inc., Canada

Chemicalland21 (2012)http://www.chemicalland21.com/industrialchem/inorganic/ALUMIN UM%20OXIDE.htm

Choudhury AJ, Barve SA, Chutia J, Pal AR, Kishore R, Jagannath, Pande M, Patil DS (2011) RF-PACVD of water repellent and protective HMDSO coatings on bell metal surfaces: Correlation between discharge parameters and film properties, Appl. surf. sci. 257: 8469-8477

Chu CF, Lu A, Liszkowski M, Sipehia R (1999) Enhanced growth of animal and human endothelial cells on biodegradable polymers, Biochim. Biophys. Acta 1472: 479-485

Chu PK, Chen JY, Wang LP, Huang N (2002) Plasma-surface modification of biomaterials, Mater. sci. eng. R 36: 143-206

Cordingley R, Kohan, Ben-Nissan B, Pezzotti G (2003) Alumina and Zirconia Bioceramics in Orthopaedic Applications, J Aust. ceram. soc. 39: 20-28

Dalby MJ, Giannaras D, Riehle MO, Gadegaard N, Affrossman S, Curtis AS (2004) Rapid fibroblast adhesion to 27nm high polymer demixed nano-topography, Biomater. 25: 77-83

Dekker A, Reitsma K, Beugeling T, Bantjes A, Feijen J, Kirkpatrick CJ, van Aken WG (1992) Surface modification of hydrophobic polymers for improvement of endothelial cell-surface interactions, Clin. mater. 11: 157-162

Dekker A, Reitsma K, Beugeling T, Bantjes A, Feijen J, van Aken WG (1991) Adhesion of endothelial cells and adsorption of serum proteins on gas plasma-treated polytetrafluoroethylene, Biomater. 12: 130-138

Diener electronic GmbH + Co. KG (2012) http://www.plasma.de

Doughty C, Findikoglu AT, Venkatesan T (1995) Steady state pulsed laser deposition target scanning for improved plume stability and reduced particle density, Appl. phys. lett. 66: 1276-1278

Eason R (2007) Pulsed Laser Deposition of Thin Films Applications-Led Growth of Functional Materials, John Wiley & Sons, New Jersey

Extrand CW (2003) Contact Angles and Hysteresis on Surfaces with Chemically Heterogeneous Islands, Langmuir 19: 3793-3796

Eyettand M, Bäuerle D (1987) Influence of the beam spot size on ablation rates in pulsed-laser processing, Appl. phys. lett. 51: 2054-2055

F. Hoffmann La-Roche (2005) Cell Proliferation Reagent WST-1 Catalogue, Cat. No. 11 644 807 001

Feng Y, Gottmann J, Kreutz EW (2003) Structuring of poly ether ether ketone by ArF Excimer laser radiation in different atmospheres, Appl. surf. sci. 211: 68-75

Feret FR, Roy D, Boulanger C (2000) Determination of alpha and beta alumina in ceramic alumina by X-ray diffraction, Spectrochim. Acta Part B at. spectrosc. 55: 1051-1061

Ferguson SJ, Visser JMA, Polikeit A (2006) The long-term mechanical integrity of non-reinforced PEEK-OPTIMA polymer for demanding spinal applications: experimental and finite-element analysis, Eur. spine j. 15: 149-156

Finch DS, Oreskovic T, Ramadurai K, Herrmann CF, George SM, Mahajan RL (2008) Biocompatibility of atomic layer-deposited alumina thin films, J. biomed. mater. res. part A 87A: 100-106

Fridman A (2008) Plasma Chemistry, Cambridge University Press, New York

Gabzdyl J, Brodsky M (2013) Micro-Cutting with Nanosecond Pulsed Fiber Lasers, BFI Optilas Application Notes

Gao L, McCarthy TJ (2007) How Wenzel and Cassie Were Wrong, Langmuir 23: 3762-3765

GEO 347K: Gems & Gem Minerals Department of Geological Sciences, The University of Texas at Austin (2012)http://www.geo.utexas.edu/courses/347k/redes ign/gem_notes/corundum/corundum_main.htm

Goodfellow Corporation (2012) http://www.goodfellow.com/

Gottmann J, Kreutz EW (1999) Pulsed laser deposition of alumina and zirconia thin films on polymers and glass as optical and protective coatings, Surf. coat. technol. 116–119: 1189-1194

Green S, Schlegel J (2001) A polyaryletherketone biomaterial for use in medical implant applications, Polymers for the Medical Industry 2001 Proceedings, Rapra Technology Limited, Shropshire, UK

Guilak F, Cohen DM, Estes BT, Gimble JM, Liedtke W, Chen CS (2009) Control of Stem Cell Fate by Physical Interactions with the Extracellular Matrix, Cell stem cell 5: 17-26

Ha SW, Hauert R, Ernst KH, Wintermantel E (1997) Surface analysis of chemically-etched and plasma-treated polyetheretherketone (PEEK) for biomedical applications, Surf. coat. technol. 96: 293-299

Haidar A, Martinez MM, Lee J, Akkan CK, Brück S, Löw K, Aktas OC, Abdul-Khaliq H (2011) Improved endothelialisation on silicon oxide (SiOx) thin film : possible approach for stent coatings, Clin. res. cardiol. 100: 852-853

Hancock G (1988) Laser studies of gas-phase kinetics and photochemistry, J. chem. soc., Faraday trans. 2 84: 429-440

Harsha AP, Tewari US (2003) The Effect of Fibre Reinforcement and Solid Lubricants on Abrasive Wear Behavior of Polyetheretherketone Composites, J. reinf. plast. compos. 22: 751-767

Hayes, J. S.: Czekanska, E. M.: Richards, R. G. (eds) (2012) The Cell–Surface Interaction. Springer-Verlag Berlin Heidelberg

Hecht E (2002) Optics 4th ed., Addison Wesley, San Francisco

Hegemanna D, Vohrera U, Oehra C, Riedelb R (1999) Deposition of SiO_x films from O_2/HMDSO plasmas, Surf. coat. technol. 116-119: 1033-1036

Herzog D, Jaeschke P, Meier O, Haferkamp H (2008) Investigations on the thermal effect caused by laser cutting with respect to static strength of CFRP, Int j mach tool manuf 48: 1464-1473

Jenkins MJ (2000) Relaxation behaviour in blends of PEEK and PEI, Polym. 41: 6803-6812

Kang B, Ryu SC, Park HC (2012) A study of the use of a hydroxyapatite and poly(methyl methacrylate) composite as a material for implants, J. ceram. process. res. 13: 791-796

Kannatey-Asibu E (2009) Principles of Laser Materials Processing, John Wiley & Sons, New Jersey

Khanga D, Lua J, Yao C, Haberstroh KM, Webster TJ (2008) The role of nanometer and sub-micron surface features on vascular and bone cell adhesion on titanium, Biomater. 29: 970-983

Kim J, Chaudhury MK, Owen MJ, Orbeck T (2001) The Mechanisms of Hydrophobic Recovery of Polydimethylsiloxane Elastomers Exposed to Partial Electrical Discharges, J colloid int. sci. 244: 200-207

Kim SH, S I, J S (2009) Ablation characteristics of aluminum oxide and nitride ceramics during femtosecond laser micromachining, Appl. surf. sci. 255: 9717-9720

Kim Y, Park H, Chun JS, Lee W (1994) Compositional and structural analysis of aluminum oxide films prepared by plasma-enhanced chemical vapor deposition, Thin solid films 237: 57-65

Knowles MRH, Rutterford G, Karnakis D, Ferguson A (2007) Micro-machining of metals, ceramics and polymers using nanosecond lasers, Int. j. adv. manuf. technol.33: 95-102

Kobayashi NP, Donley CL, Wang S, Williams RS (2007) Atomic layer deposition of aluminum oxide on hydrophobic and hydrophilic surfaces, J. cryst. growth 299: 218-222

Krebs H, Weisheit M, Faupel J, Süske E, Scharf T, Fuhse C, Störmer M, Sturm K, Seibt M, Kijewski H, Nelke D, Panchenko E, Buback M (2003) Pulsed Laser Deposition (PLD) -- A Versatile Thin Film Technique, Adv. solid state phys. 43: 505-518

Krüss GmbH (2013) http://www.kruss.de/en/theory/measurements/contact-angle.html

Kubena P, Kotalova L (2012) Self-Expanding Plastic Stent, US Patent, US8323351 B2

Kurtz SM, Devine JN (2007) PEEK Biomaterials in Trauma, Orthopedic, and Spinal Implants, Biomater. 28: 4845-4869

Kwon DY, Kim JI, Kim DY, Kang HJ, Lee B, Lee KW, Kim MS (2012) Biodegradable stent, J. biomed. sci. eng. 5: 208-216

Laurens P, Sadras B, Decobert F, Arefi F, Amouroux J (1999) Modifications of polyether-etherketone surface after 193 nm and 248 nm excimer laser radiation, Appl. surf. sci. 138-139; 93-96

Laurens P, Bouali MO, Meducin F, Sadras B (2000) Characterization of modifications of polymer surfaces after excimer laser treatments below the ablation threshold, Appl. surf. sci. 154-155: 211-216

Lawrence J, Li L (2001) Modification of the wettability characteristics of polymethyl methacrylate (PMMA) by means of CO_2, Nd:YAG, excimer and high power diode laser radiation, Mat. sci. eng. A 303; 142-149

Lee J, Miró MM, Akkan CK, Haidar A, Metzger W, Schwarz LK, Zaporojtchenko V, Schäfer KH, Abdul-Khaliq H, Veith M, Aktas C (2013) Development of Multi Scale Structured Al/Al_2O_3 Nanowires for Controlled Cell Guidance, J. biomed. nanotechnol. 9: 295-298

Lee SJ, Sundararajan N (eds) (2010) Microfabrication for microfluidics, Artech House inc, Norwood

Liang H, Lawrence J (eds) (2005) Laser surface treatment of Bio-Implant materials, John Wiley & Sons Ltd, West Sussex

Lieberman MA, Lichtenberg AJ (2005) Principles of Plasma Discharges and Materials Processing 2nd ed., John Wiley & Sons Ltd, New York

Liu SJ, Chiang FJ, Hsiao CY, Kau YC, Liu KS (2010) Fabrication of balloon-expandable self-lock drug-eluting polycaprolactone stents using micro-injection molding and spray coating techniques, Annals biomed. eng. 10: 3185-3194

Majumdar J., Manna I. (2003) Laser Processing of Materials, Sadhana 28: 495-562

Marcu A, Grigoriu C, Jiang W, Yatsui K (2000) Pulsed laser deposition of YBCO thin films in a shadow mask configuration, Thin solid films 360: 166-172

Marmur A (2003) Wetting on Hydrophobic Rough Surfaces: To Be Heterogeneous or Not To Be?, Langmuir 19: 8343-8348

Marmur A (2009) Solid-Surface Characterization by Wetting, Annu. rev. mater. res. 39: 473-489

Moe AAK, Suryana M, Marcy G, Lim SK, Ankam S, Goh JZW, Jin J, Teo BKK, Law JBK, Law HY, Goh ELK, Sheetz MP, Yim EKF (2012) Microarray with Micro- and Nano-topographies Enables Identification of the Optimal Topography for Directing the Differentiation of Primary Murine Neural Progenitor Cells, Small 8: 3050-3061

Molloy D, Jack C, Esposito C, Walter WL (2012) A Mid-Term Analysis Suggests Ceramic on Ceramic Hip Arthroplasty Is Durable with Minimal Wear and Low Risk of Squeak, HSS J. 8: 291-294

Mróz W, Prokopiuk A, Korwin-PawlowskiiML, Burdyńska S (2008) Deposition of Thin Films Composed of $Fe_{81}B_{13.5}Si_{3.5}Co_2$ Material by PLD Method Using the ArF Excimer Laser, J. laser micro/nanoeng. 3: 170-174

Mutlu M, Kacar E, Akman E, Akkan CK, Demir P, Demir A (2009) Effects of The Laser Wavelength on Drilling Process of Ceramic Using Nd:YAG Laser, J. laser micro/nanoeng. 4: 84-88

Narushima K, Ikeji H (2009) Plasma Surface Modification of Poly(aryl ether ether ketone) and Surface Metallization using Copper Metal, J. soc. fiber sci. technol, Jpn, 65: 127-131 [38]

Newport Corp. (2012a) http://www.newport.com/Gaussian-Beam-Optics/144899/1033/content.aspx

Newport Corp. (2012b) http://www.newport.com/Quanta-Ray-Pro-Series-Pulsed-Nd-YAG-Lasers/368168/1033/info.aspx#tab_Specifications

Newport Corp. (2013) http://www.newport.com/Technical-Note-Optics-Formulas/144956/1033/content.aspx

Oberringer M, Akman E, Lee J, Metzger W, Akkan CK, Kacar E, Demir A, Abdul-Khaliq H, Pütz N, Wennemuth G, Pohlemann T, Veith M, Aktas C (2013) Reduced myofibroblast differentiation on femtosecond laser treated 316LS stainless steel, Mater. sci. eng. C 33: 901-908

Pashkuleva I, Marques AP, Vaz F, Reis RL (2010) Surface modification of starch based biomaterials by oxygen plasma or UV-irradiation, J. mater. sci. mater. med. 21: 21-32

Patnaik P (2003) Handbook of Inorganic Chemicals, The McGraw-Hill, New York

Peng Q, Sun XY, Spagnola JC, Hyde GK, Spontak RJ, Parsons GN (2007) Atomic layer deposition on electrospun polymer fibers as a direct route to Al_2O_3 microtubes with precise wall thickness control, Nano lett. 7: 719-722

Plasma Electronic GmbH (2012) http://www.plasma-electronic.de

Quéré D (2008) Wetting and Roughness, Annu. rev. mater. res. 38: 71-99

Ran C, Ding G, Liu W, Deng Y, Hou W (2008) Wetting on Nanoporous Alumina Surface: Transition between Wenzel and Cassie States Controlled by Surface Structure, Langmuir 24: 9952-9955

Ratner BD, Hoffman AS, Schoen FJ, Lemons JE (eds) (1996) Biomaterials science An Introduction to Materials in med., Academic Press, California

Refractive Index Database (2012) http://refractiveindex.info/?group=METALS&material =Silver

Riveiroa A., Sotoa R., Comesañaa R., Boutinguizaa M., del Vala J., Quinteroa F., Lusquiñosa F., Poua J. (2012) Laser surface modification of PEEK, Appl. surf. sci. 258: 9437-9442

Romoli L, Fischer F, Kling R (2012) A study on UV laser drilling of PEEK reinforced with carbon fibers, Opt. laser. eng. 50: 449-457

Rossi F, Kylián O, Rauscher H, Hasiwa M, Gilliland D (2009) Low pressure plasma discharges for the sterilization and decontamination of surfaces, New j. phys. 11: 115017

RP Photonics Consulting GmbH (2012) http://www.rp-photonics.com/encyclopedia.html /

Sagomonyants KB, Jarman-Smith ML, Devine JN, Aronow MS, Gronowicz GA (2008) The in vitro response of human osteoblasts to polyetheretherketone (PEEK) substrates compared to commercially pure titanium, Biomater. 29: 1563-1572

Schou J (2006) Laser Beam–Solid Interactions: Fundamental Aspects, Pauleau Y (eds) Materials Surface Processing by Directed Energy Techniques, Elsevier Ltd, Oxford

Silfvast WT (1996) Laser Fundamentals. 2nd ed, Cambridge University Press, Cambridge

Smith WF (1996) Principles of materials science and engineering 3ed, McGraw-Hill, New York

Song H, Zhang Z, Men X (2008) Superhydrophobic PEEK/PTFE composite coating, Appl. phys. A 91: 73-76

Spagnola JC, Gong B, Parsons GN (2010) Surface texture and wetting stability of polydimethylsiloxane coated with aluminum oxide at low temperature by atomic layer deposition, J. vac. sci. technol. A 28: 1330-1337

Sprague EA, Tio F, Ahmed SH, Granada JF, Bailey SR (2012) Impact of parallel micro-engineered stent grooves on endothelial cell migration, proliferation, and function: an in vivo correlation study of the healing response in the coronary swine model, Circ. cardiovasc. interv. 5: 499-507

Steen W, Mazumder J (2010) Laser Material Processing 4th ed., Springer London Dordrecht Heidelberg NewYork

SÜSS MicroTec AG (2012) SMO TechInfo 10 - Beam Homogenizer, http://www.suss-microoptics.com

Svendsen W, Ellegaard O, Schou J (1996) Laser ablation deposition measurements from silver and nickel, Appl. phys. A 63: 247-255

Takeda S, Fukawa M (2005) Role of surface OH groups in surface chemical properties of metal oxide films, Mater. sci. eng. B 119: 265-267

Thorlabs Inc (2012) www.thorlabs.com

Träger F. (2007), Handbook of Lasers and Optics, Springer, LLC New York

Tsougeni K, Vourdas N, Tserepi A, Gogolides E (2009) Mechanisms of Oxygen Plasma Nanotexturing of Organic Polymer Surfaces: From Stable Super Hydrophilic to Super Hydrophobic Surfaces, Langmuir 25: 11748-11759

Tsunekawa M, Nishio S, Sato H (1994) Laser ablation of polymethylmethacrylate and polystyrene at 308 nm: Demonstration of thermal and photothermal mechanisms by a time-of-flight mass spectroscopic study, J. appl. phys. 76: 5598-5600

Tunna L, Kearns A, O'Neill W, Sutcliffe CJ (2001) Micromachining of copper using Nd:YAG laser radiation at 1064, 532, and 355 nm wavelengths, Opt. laser technol. 33: 135-143

Tyuninaand M, Leppävuori S (2000) Effects of laser fluence, size, and shape of the laser focal spot in pulsed laser deposition using a multielemental target, J. appl. phys. 87: 8132-8142

Veith M, Aktas OC, Lee J, Miró MM, Akkan CK (2010a) Biphasic Nano-Materials and Applications in Life Sciences: 1D Al/Al$_2$O$_3$ Nanostructures for Improved Neuron Cell Culturing, Mathur S, Shen H, Singh M (eds), Nanostructured Materials and Systems, John Wiley & Sons, Inc., Hoboken, NJ, USA

Veith M, Aktas OC, Metzger W, Sossong D, Ullah Wazir H, Grobelsek I, Pütz N, Wennemuth G, Pohlemann T, Oberringer M (2010b) Adhesion of fibroblasts on micro- and nanostructured surfaces prepared by chemical vapor deposition and pulsed laser treatment, Biofabrication 2

Veith M, Faber S, Hempelmann R, Janssen S, Prewo J, Eckerlebe H (1996a) Synthesis and microstructure of nanostructured Al/Al$_2$O$_3$ (H)-composite, J. mater. sci. 31: 2009-2017

Veith M, Faber S, Wolfanger H, Huch V (1996b) (tert-Butoxy)aluminium and -gallium Hydrides, Chemische Berichte (known as: Eur. j. inorg. chem.) 129: 381-384

Veith M, Lee J, Miró MM, Akkan CK, Dufloux C, Aktas OC (2012) Bi-phasic nanostructures for functional applications, Chem. soc. rev. 41: 5117-5130

Victrex Manufacturing Limited (2012) Victrex Properties Guide, http://www.victrex.com/

Villarreal-Barajas JE, Escobar-Alarcon L, Gonzalez PR, Camps E, Barboza-Flores M (2002) Thermoluminescence properties of aluminum oxide thin films obtained by pulsed laser deposition, Radiat. meas. 35: 355-359

Voelkel R, Weible KJ (2008) Laser Beam Homogenizing: Limitations and Constraints, SPIE proc. Opt. fabr. test. metrol. III 7102

Walboomers XF, Jansen JA (2001) Cell and tissue behavior on micro-grooved surfaces, Odontol. 89: 2-11

Weaver I, Lewis CLS (1995) Polar distribution of ablated atomic material during the pulsed laser deposition of Cu in vacuum: Dependence on focused laser spot size and power density, J. appl. phys. 79: 7216-7222

Webster TJ, Hellenmeyer EL, Price RL (2005) Increased osteoblast functions on theta+delta nanofiber alumina, Biomater. 26: 953-960

Wenzel RN (1936) Resistance of Solid Surfaces to Wetting by Water, Ind. eng. chem. 28: 988-994

Wheatley DJ, Raco L, Bernacca GM, Sim I, Belcher PR, Boyd JS (2000) Polyurethane: material for the next generation of heart valve prostheses?, Eur J Cardiothorac Surg. 17: 440-448.

Williams D (2008) Polyetheretherketone for Long-Term Implantable Devices, Med. device technol.

Williams DF, McNamara A, Turner RM (1987) Potential of polyetheretherketone (PEEK) and carbon-fibre-reinforced PEEK in medical applications, J. mater. sci. lett. 6: 188-190

Willmott PR, Huber JR (2000) Pulsed laser vaporization and deposition, Rev. mod. phys. 72: 315-328

Wu JM, Chung Y, Belford KJ, Smith GD, Takayama S, Lahann J (2006) A surface-modified sperm sorting device with long-term stability, Biomed. Microdevices 8: 99-107

Yang CS, Kim JS, Choi JW, Kwon MH, Kim YJ, Choi JG, Kim GT (2000) XPS Study of Aluminum Oxides Deposited on PET Thin Film XPS Study of Aluminum Oxides Deposited on PET Thin Film, J. ind. eng. chem. 6: 149-156

Yu F (2006) Laser interference lithography: micropatterning of polymer surface for cell adhesion, (Dissertation), Universität des Saarlandes, Saarbrücken

Yue TM, Hu QW, Mei Z, Man HC (2001) Laser cladding of stainless steel on magnesium ZK60/SiC composite, Mater. lett. 47: 165-170

List of Figures and Tables

Abbreviations

A^*:	Atomic weight
A:	Absorption, Effective frequency factor, Laser beam area on substrate
Å:	Angstrom
AFM:	Atomic Force Microscopy
ASC:	Adipose tissue derived stem cell
CA:	Contact Angle
c_p:	Specific heat at constant pressure
CVD:	Chemical Vapor Deposition
CW:	Continuous wave
d:	Ablation depth, Particle radius
D:	Thermal diffusivity, Laser beam diameter
DAPI:	4',6-diamidino-2-phenylindole
DC:	Direct Current
DES:	Drug Eluting Stents
D_{ML}:	Diameter of a single microlens
DRG:	Dorsal Root Ganglion
DUV:	Deep Ultraviolet
E:	Laser energy
E_a:	Generated effective area
EC:	Endothelial cells
ECM:	Extra Cellular Matrix
EDS:	Energy Dispersive X-Ray Spectroscopy
E_s:	Surface energy
eV:	Electron volt
F:	Laser fluence, Focal length
f:	Surface fraction, Focal length
Fn:	Fibronectin
fs:	Femtosecond
HA:	Hydroxyapatite
HAS:	Human serum albumin
HDL:	Human high-density lipoprotein
HDMEC:	Human dermal micro vascular endothelial cells
HMDSO:	Hexamethydisiloxane
HUVEC:	Human Umbilical Vein Endothelial Cell
HUVSMC:	Human Umbilical Vein Smooth Muscle Cell
Hz:	Hertz
I:	Light intensity
I_0:	Incoming light intensity
IgG:	Human immunoglobulin
INM:	INM-Leibniz Institute for New Materials
IR:	Infrared
I_{th}:	Heat diffusion length

J:	Ablation rate of atoms per unit area per time, Joule
k:	Imaginary part of refractive index
LASER:	Light Amplification of Stimulated Emission by Reflection
LSGS:	Low Serum Growth Supplement
LT:	Laser treated PEEK substrate
LT-Al:	Laser treated alumina plates
LT-NW:	Laser treated Al/Al_2O_3 core/shell NWs
LT-PLD:	Alumina deposited laser-treated PEEK substrate
M^2:	Laser beam quality factor
MF:	Miyofibroblast
mJ:	Millijoule
ms:	Milisecond
MSC:	Mesenchymal Stem Cells
MS-PLD:	Matrix Shaped Pulsed Laser Deposition
n:	Real part of refractive index
N_A:	Avogadro number
ND:	Neutral density
n_i:	Real part of refractive index of air
n_p:	Plasma plume particle density
ns:	Nanosecond
NT:	Non-treated PEEK substrate
n_t:	Real part of refractive index of the material
NT-Al:	Non-treated alumina plates
NT-NW:	Non-treated Al/Al_2O_3 core/shell NWs
NT-PLD:	alumina deposited non-treated PEEK substrate
NW:	Nanowire
P:	Generated diffraction patterns
P:	Laser power
p:	P polarization
P:	Pressure
Pa:	Pascal
PAEK:	Poly-aryl ether ketone
PBS:	Phosphate buffered saline
PCL:	Poly(ε-caprolactone)
PE:	Polyethylene
PECVD:	Plasma Enhanced Chemical Vapor Deposition
PEEK:	Polyetheretherketone
PEKEKK:	Poly-ether ketone ether ketone ketone
PET:	Polyethylene-therephtalate
PFA:	Paraformaldehyde
PGA:	poly(glycolicacid)
PLD:	Pulsed Laser Deposition
PLLA:	Poly-L-lactic acid
PLT:	Plasma and laser treated PEEK substrate
PLT-PLD:	Alumina deposition after the plasma and laser treatments of PEEK substrate

ps:	Picosecond
PT:	Plasma treated PEEK substrate
PTFE:	Polytetrafluoroethylene
PTFE:	Polytetrafluoroethylene
PT-PLD:	Alumina deposited plasma treated PEEK substrate
P_v:	Vapor pressure at the surface temperature
r:	Reflection coefficient, radius of laser beam
R:	Reflectivity, ideal gas constant, Radius of curvature
r:	Roughness
R_a:	Average roughness
RAEC:	Rat aortic endothelial cells
RbMVEC:	Rabbit micro vascular endothelial cell
RF:	Radio Frequency
r_p:	Reflection coefficient at p polarization
R_p:	Reflectivity at p polarization
r_s:	Reflection coefficient at s polarization
R_s:	Reflectivity at s polarization
RT:	Room temperature
s:	S polarization
sccm:	Standard Cubic Centimeters per Minute
SEM:	Scanning Electron Microscopy
SMC:	Smooth muscle cells
T:	Temperature, Tesla, Transmission
t_c:	Central thickness
TCPS:	Tissue Culture Polystyrene
T_e:	Electrons Temperature
TEM:	Transverse Electromagnetic Modes
T_g:	Glass transition temperature
T_i :	Ion temperatures
T_m:	Melting temperature
T_s:	Surface temperature
t_v:	Vaporization temperature
U_0:	Cohesive energy per atom
UV:	Ultraviolet
VIS:	Visible
WST-1:	Cell Proliferation Reagent
XPS:	X-Ray Photoelectron Spectroscopy
Y:	Ablation yield
z:	Sample thickness
Z_K:	Knudsen Layer
α:	Absorption coefficient, crystal state of alumina
β:	Collision cross section
η:	Refractive index
θ:	Angle
$θ_i$:	Angle of the incoming light

θ_t: Angle of refracted light inside the material
θ_Y: Young's contact angle
κ: Thermal conductivity
λ: Wavelength
ρ: Mass density
σ_l: Surface tension of liquid
σ_s: Surface tension of solid
σ_{sl}:   Tension of solid-liquid interface
τ_L: Pulse length of the laser
Φ: Laser fluence
Φ_{th}:   Threshold fluence of laser
ψ: Mean free path
ω_0:   Spot size

Acknowledgment